Design, modeling and characterization of multi-stable metastructures for shape reconfiguration and energy absorption

Zhang, Y.

DOI
10.4233/uuid:6f942371-855f-4fba-bcd6-a264edbeb5dd

Publication date
2022

Document Version
Final published version

Citation (APA)
Zhang, Y. (2022). *Design, modeling and characterization of multi-stable metastructures for shape reconfiguration and energy absorption*. [Dissertation (TU Delft), Delft University of Technology]. https://doi.org/10.4233/uuid:6f942371-855f-4fba-bcd6-a264edbeb5dd

Important note
To cite this publication, please use the final published version (if applicable).
Please check the document version above.

Design, modeling and characterization of multi-stable metastructures for shape reconfiguration and energy absorption

DESIGN, MODELING AND CHARACTERIZATION OF MULTI-STABLE METASTRUCTURES FOR SHAPE RECONFIGURATION AND ENERGY ABSORPTION

Dissertation

for the purpose of obtaining the degree of doctor
at Delft University of Technology,
by the authority of the Rector Magnificus, Prof.dr.ir. T.H.J.J. van der Hagen,
chair of the Board for Doctorates,
to be defended publicly on
Monday 17 January 2022 at 17:30 o'clock

by

Yong ZHANG

Master of Engineering in Mechanics,
Harbin Institute of Technology, China,
born in Yantai, China.

This dissertation has been approved by the promotors.

Composition of the doctoral committee:

Rector Magnificus,	chairperson
Prof.dr.ir. A. van Keulen,	Delft University of Technology, promotor
Dr.ir. M. Tichem,	Delft University of Technology, promotor
Independent members:	
Prof.dr. M.I. Frecker,	The Pennsylvania State University, USA
Prof.dr. C. Bisagni,	Delft University of Technology
Prof.dr. A.A. Zadpoor,	Delft University of Technology
Prof.dr.ir. J.L. Herder,	Delft University of Technology
Dr.ir. J.T.B. Overvelde,	Eindhoven University of Technology

This project was financially sponsored by China Scholarship Council from Sep. 2016 to Sep. 2020.

Keywords: multi-stable metastructures, snap-through behavior, negative stiffness, translational and rotational states, energy absorption, reconfiguration

Printed by: Ipskamp Printing

ISBN 978-94-6384-286-0

An electronic version of this dissertation is available at
http://repository.tudelft.nl/.

To my beloved parents

CONTENTS

SUMMARY

Materials and their properties play an important role in the development of products. To create materials with new functionalities, in the last decade, researchers have looked into the possibility to tailor the material properties by changing their inner micro-structures, namely metamaterials. Different from the chemical composition design, metamaterials are carefully structured materials whose effective unusual properties are mainly governed by their structures at small length scale. Thus, metamaterials are often referred to as metastructures.

In order to tune the functionality of metastructures, much effort has been made recently to develop flexible metastructures that can achieve configuration transformations. In this regard, multi-stable beam-type metastructures exhibiting snap-through behavior have been proposed, for which a number of stable states can be maintained without the need of external power supply. By arranging a series of beams exhibiting bi-stability, multi-stable metastructures can be constructed. However, current designs of multi-stable metastructures are limited in terms of structural kinematics and the associated functionalities are not fully explored. In this thesis, we aim to present design strategies that can facilitate new kinematic behavior and functionalities for multi-stable metastructures (i.e., energy absorption and shape reconfiguration).

Multi-stable metastructures featuring many beam elements arranged serially can normally realize translational motion. In Chapter 2, we investigate the additional rotational degrees of freedom by incorporating rotational compliance. In doing so, multi-stable metastructures are capable of realizing both translational and rotational motion, facilitating their applicability in soft robotics and deployable structures. Furthermore, a theoretical model that can describe the snap-through deformation is presented and the effect of geometric parameters on rotational stable states is analyzed. The design space for realizing the translational and rotational stable states is identified using this model.

In Chapter 3, we extend the concept of rotational states to a three-dimensional (3D) structural design. That is, the proposed multi-stable metastructures are able to achieve multiple rotational states in different directions, depending on the arrangement of unit cells. To reveal the relation between the unit cell arrangement and rotational states, an experimental evaluation is conducted, in which we consider both parallel and serial stacking of unit cells. It is shown that for the in-plane patterning, the rotational degrees of freedom are mainly determined by the structural symmetry axes. In case of serial arrangement, the translational and rotational stable states can be easily programmed by adding more layers.

In Chapter 4, we study the energy dissipation of multi-stable metastructures. New design strategies are proposed to enhance the metastructures' mechanical response and energy absorption. In particular, it is found that by tuning structural bending stiffness, a large benefit in energy dissipation can be obtained without using more material. Here, lattice and box-shaped cross sections are integrated into curved beams to develop structural designs (i.e., hierarchical and hollow beams) with relatively high bending stiffness. Both numerical and experimental results show that the proposed metastructures are able to respond via sequential snap-through transitions with improved energy dissipation. Moreover, the influence of geometric parameters on snap-through behavior, local buckling, and bi-stability are investigated. It should be noted that the proposed design strategy is not only applicable to beam-type elements but also useful for enhancing energy dissipation of shell structures.

In addition to the energy dissipation, multi-stable metastructures can also be designed to realize shape reconfiguration. In Chapter 5, we explore this possibility and present a design concept of morphing surface based on multi-stable metastructures. The multi-stable metastructure here can function as a mechanism to realize curved stable states for a surface. To achieve such stable configurations, we propose an analytical formulation that can identify the proper geometric parameters for bi-stability. Furthermore, it is found that two-dimensional arrangements of bi-stable elements can lead to a series of stable states, including horizontal, vertical and diagonal configurations. With the proper arrangement of unit cells, the proposed morphing surfaces can be exploited to achieve a number of curved configurations for adaptive structures.

Multi-stable beam-type metastructures exhibiting translational and rotational degrees of freedoms hold great potential for developing reconfigurable structures and energy absorbers. The implementation of actuation as well as other forms of snap-through transition (e.g., twisting) can be further explored to enhance the functionality of multi-stable metastructures.

SAMENVATTING

Materialen en hun eigenschappen spelen een belangrijke rol in de ontwikkeling van producten. Om materialen te creëren met nieuwe functionaliteiten, hebben wetenschappers in het afgelopen decennium gekeken naar mogelijkheden om materiaaleigenschappen aan te passen door hun micro-structuur te veranderen, genaamd metamaterialen. Anders dan het ontwerp door chemische samenstelling, zijn metamaterialen zorgvuldig gestructureerde materialen wiens resulterende ongewone eigenschappen vooral worden beïnvloed door hun structuren op kleine schaal. Daarom worden metamaterialen vaak ook metastructuren genoemd.

Om de functionaliteit van metastructuren aan te passen, is recent veel onderzoek gedaan naar flexibele metastructuren die van configuratie kunnen transformeren. In dit opzicht zijn meervoudig stabiele balk-achtige metastructuren voorgesteld die doorknikgedrag laten zien, waarvoor een aantal stabiele toestanden behouden kunnen worden zonder externe energie toevoer. Door een reeks bi-stabiele balken te schikken, kunnen meervoudig stabiele metastructuren worden geconstrueerd. Echter, huidige ontwerpen van meervoudig stabiele metastructuren zijn gelimiteerd wat betreft structurele kinematica en de bijbehorende functionaliteiten zijn niet volledig verkend. In dit proefschrift, streven wij er naar om nieuwe ontwerp-strategieën te presenteren die nieuw kinematisch gedrag en functionaliteit voor meervoudig stabiele metastructuren kunnen vergemakkelijken (bijvoorbeeld energie absorptie en herconfiguratie van vorm).

Meervoudig stabiele metastructuren met veel balk-elementen in serie geschakeld kunnen normaal gesproken een translatie-beweging realiseren. In Hoofdstuk 2, onderzoeken we de bijkomende rotatie-vrijheidsgraden door toevoeging van rotatie-flexibiliteit. Hierdoor zijn meervoudig stabiele metastructuren in staat om zowel translatie- als rotatiebewegingen te realiseren, wat hun toepasbaarheid in zachte robotica en ontplooibare structuren vergemakkelijkt. Verder wordt een theoretisch model gepresenteerd dat de doorknik-vervorming kan beschrijven en wordt het effect van de geometrische parameters op de rotatie-stabiele toestanden geanalyseerd. De ontwerpruimte voor realisatie van translatie- en rotatie-stabiele toestanden wordt geïdentificeerd met behulp van dit model.

In Hoofdstuk 3 breiden we het concept van rotatie-toestanden uit naar een driedimensionaal (3D) structureel ontwerp. Dit houdt in dat de voorgestelde meervoudig stabiele metastructuren meerdere rotatie-toestanden in verschillende richtingen kunnen aannemen, afhankelijk van de schikking van de eenheidscel. Om de relatie tussen de schikking van de eeneheidscel en de rotatie-toestanden bloot te leggen, is een experimentele evaluatie gedaan, waarin zowel parallelle als seriële opbouw worden beschouwd. Voor het patroon in het vlak, is laten zien dat de rotatie-vrijheidsgraden vooral

worden bepaald door de structurele symmetrieassen. In geval van seriële schikking, kunnen de translatie- en rotatie-stabiele toestanden gemakkelijk worden geprogrammeerd door meerdere lagen toe te voegen.

In Hoofdstuk 4 bestuderen we de energie dissipatie van meervoudig stabiele metastructuren. Nieuwe ontwerpstrategieën worden voorgesteld om het mechanisch gedrag en de energie absorptie van de metastructuren te verbeteren. In het bijzonder is ontdekt dat het afstemmen van de structurele buigstijfheid veel baat heeft voor de dissipatie van energie, zonder gebruik van extra materiaal. Hiervoor worden rooster en doosvormige doorsnedes geïntegreerd in gekromde balken (d.w.z., hiërarchische en holle balken) om structurele ontwerpen te ontwikkelen met relatief hoge buigstijfheid. Zowel numerieke als experimentele resultaten laten zien dat de voorgestelde metastructuren zich kunnen gedragen door opeenvolgende doorknik-transities met verbeterde energie dissipatie. Verder wordt de invloed van geometrische parameters op doorknik-gedrag, lokale knik en bi-stabiliteit onderzocht. Er moet worden opgemerkt dat de voorgestelde ontwerpstrategie niet alleen toepasbaar is voor balk-elementen, maar ook nuttig is voor het verbeteren van energie dissipatie in schaal-structuren.

Naast de energie dissipatie kunnen ook meervoudig stabiele metastructuren worden ontworpen om herconfiguratie van vorm te realiseren. In Hoofdstuk 5 verkennen we deze mogelijkheid en presenteren we een ontwerpconcept voor vervormbare oppervlakten gebaseerd op meervoudig stabiele metastructuren. De meervoudig stabiele metastructuren kunnen hier fungeren als een mechanisme om gekromde stabiele toestanden voor een oppervlak te realiseren. Om dergelijke stabiele configuraties te bereiken, stellen we een analytische formulering voor die de juiste geometrische parameters voor bi-stabiliteit kan identificeren. Verder is gevonden dat tweedimensionale opstellingen van bi-stabiele elementen kunnen leiden tot een reeks stabiele toestanden, waaronder horizontale, verticale en diagonale configuraties. Met de juiste opstelling van eenheidscellen kunnen de voorgestelde vervormbare oppervlakten worden benut om een aantal gebogen configuraties voor adaptieve structuren te bereiken.

Meervoudig stabiele balk-achtige metastructuren die translatie- en rotatie-vrijheidsgraden vertonen, bieden een groot potentieel voor de ontwikkeling van herconfigureerbare structuren en energie absorbeerders. De implementatie van actuatie en andere vormen van doorknik-transities (bijvoorbeeld verdraaiing) kan verder worden onderzocht om de functionaliteit van meervoudig stabiele metastructuren te verbeteren.

1

INTRODUCTION

1

1.1. BACKGROUND

Owing to the advance of additive manufacturing techniques (3D printing), the field of metamaterial design has grown rapidly in recent years. Metamaterials are rationally structured materials whose effective properties are mainly governed by their structural layout rather than the material composition. Therefore, metamaterials are also named as metastructures or architected materials in literature [1]. By carefully designing structural units and arranging them in a periodic pattern, novel functionalities, like wave manipulation and acoustic filters, can be accomplished. For instance, acoustic metamaterials are able to guide or block wave propagation within a certain range of frequencies, which allows for applications in sensing and noise reduction [2, 3].

Research on mechanical metastructures is mainly focused on structural deformations, motion, and stresses which can give rise to unconventional mechanical properties, such as negative Poisson's ratio [4–6] and negative compressibility [7]. For instance, ultra-stiff but light-weight metastructures have been designed and proposed, where strength and stiffness over density are key quantities. To realize a stiff structural design, several strategies have been studied, including micro- and nano-lattices [8] and hierarchical structures [9].

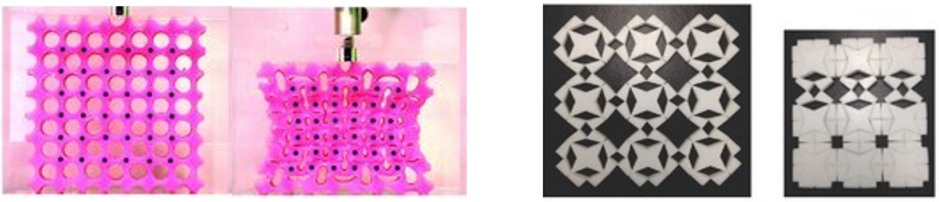

(a) (b)

Figure 1.1: Examples of flexible metastructure design. (a) A flexible metastructure that can achieve configuration transformations under compression [10]. (b) A reconfigurable metastructure is based on compliant hinges with rotational degrees of freedom [11]. Panel (a) is adapted with permission from Ref. [10], John Wiley & Sons, Inc. Panel (b) is adapted with permission from Ref. [11], John Wiley & Sons, Inc.

On the other hand, flexible metastructures that deal with large deformations and configuration transformations have been an active focus in this field because they can provide tunable properties arising from structural geometry change. Different from the above-mentioned stiff metastructures, flexible metastructure design puts emphasis on shape or configuration changes. Upon loading or actuation, the introduced flexibility enables metastructures to deform into another configuration. During the structural deformation, geometric non-linearity (e.g., finite rotations or buckling behavior) is normally involved [12, 13]. Fig. 1.1(a) and (b) present two samples that can realize evident structure reconfiguration after loading. The reconfigurability can facilitate functionalities for many applications, including actuators, deployable structures and soft robotics. A recent overview on designing such flexible metastructures can be found in the review paper authored by Bertoldi *et al.* [14].

In order to maintain the deformed configurations for flexible metastructures, a continuous actuation is often required, making the system potentially energy-inefficient. To

address this, scholars have focused on studying bi- or multi-stable metastructures with snap-through behavior. A commonly used structure for bi-stability is the pre-shaped beam, which can exhibit snap-through transitions when applied load exceeds a threshold [15]. As such, the beam is able to stabilize at the deformed configuration and it can be fully reversed to the undeformed state by applying loads in the opposite direction. Such bi-stable beam mechanisms have been widely developed in Micro-Electro-Mechanical Systems (MEMS) for providing motion outputs [16]. Based on the bi-stable mechanisms, multi-stable metastructures can be obtained by arranging multiple bi-stable elements in different manners. A few recent studies have demonstrated that the multi-stability and associated snap-through transition may open up new ways for designing a variety of functional devices, such as switches and energy absorbers [17–19]. However, the development of multi-stable metastructure is still in its infancy and it is far from being comprehensive. In this dissertation, we concentrate on the mechanical properties of multi-stable beam-type metastructures and explore their potential functionalities. The following section gives a brief introduction to multi-stable metastructures from the perspective of structural design, mechanical behavior and potential applications.

1.2. MULTI-STABLE BEAM-TYPE METASTRUCTURES

In this dissertation, we focus on metastructures based on beam-type bi-stable mechanisms. Under compression, a pre-shaped curved beam, as shown in Fig. 1.2(a), is able to flip into the deformed stable state. The snap-through transition is illustrated in Fig. 1.2(b). In a displacement-controlled quasi-static loading, the force first reaches a peak threshold and then decreases with a phase of negative stiffness. Afterwards, a positive stiffness is captured from the force-displacement curve, leading to the deformed stable state (denoted by green dot in Fig. 1.2(b)). Note that the symmetry may break up such that asymmetric buckling modes can occur during the snap-through transition. From the perspective of strain energy (blue line in the figure), the system switches from an energy-free state into a local minimum at which elastic energy is stored. This nonlinear deformation process plays a fundamental role in developing multi-stable metastructures with advanced functionalities. To obtain multi-stability, we look into different arrangements of such bi-stable elements to design multi-stable metastructures that can achieve new kinematic properties and functionalities.

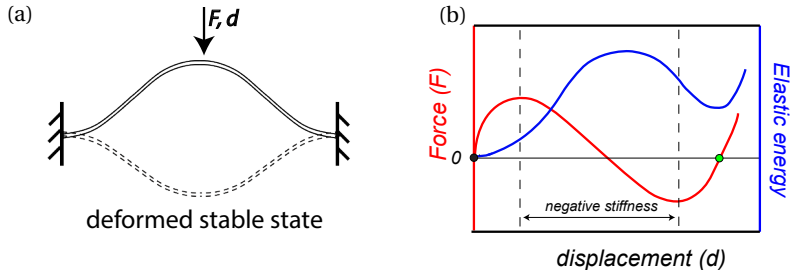

Figure 1.2: Snap-through behavior of a pre-shaped beam. (a) A schematic for a pre-shaped curved beam that exhibits two stable states and snap-through behavior when a displacement (d) is prescribed at the center. (b) The red and blue curves represent the variation of force and elastic energy during the loading process.

1

1.2.1. STRUCTURAL DESIGN AND KINEMATICS

Based on the bi-stable mechanisms, multi-stable beam-type metastructures can be built by arranging bi-stable elements in different manners, including two-dimensional (2D) planar shapes [20–25] and three-dimensional (3D) geometries [26–30]. An example of a planar multi-stable metastructure is displayed in Fig. 1.3, where each layer of this metastructure is capable of snapping into its second stable configuration. As shown in this figure, the metastructure can exhibit a large translational motion when subjected to a compressive load, resulting in deformations of potentially all layers and a sequential snap-through. This translational motion can gives rise to benefits in two aspects: energy absorption and motion-related applications, such as morphing structures and actuators.

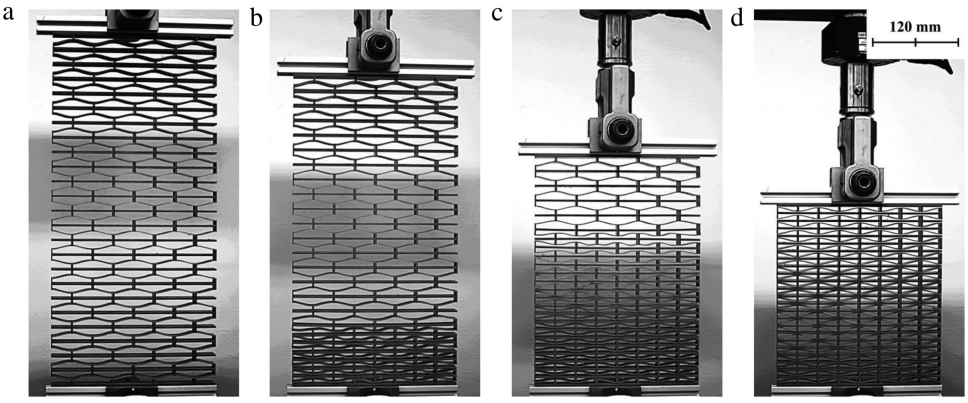

Figure 1.3: Different deformation stages of a multi-stable metastructure under unaxial compression [22]. The figure is adapted with permission from Ref. [22], Elsevier Ltd.

For shape reconfiguration or morphing, only exhibiting translation is not adequate; in other words, enabling other degrees of freedom, like rotations, is also desired in order to achieve complex shapes change. However, most previous designs have only demonstrated the presented translational transitions and studies focused on metastructures' rotational behavior are rare. In this thesis, we propose and explore the strategy to develop a new class of multi-stable metastructures that are capable of exhibiting both translational and rotational movements.

1.2.2. SHAPE RECONFIGURATION

The snap-through behavior of multi-stable metastructures plays a crucial role in the development of reconfigurable structures. By exploiting multi-stable metastructures, a number of applications have been presented in literature, including morphing structures, deployable structures, and mechanisms for actuation. For instance, the transitions of multi-stable metastructures between different stable configurations can open the door for designing deployable structures and fast actuators. In particular, the translational movement assures the direction of actuation [31], while the snap-through behavior makes it possible to realize a rapid actuation speed [32]. As displayed in Fig. 1.4(a), by integrating such translations into a cubic design, the designed structure is capable of expanding its shape from a small-volume state to a large deployed stable configuration

that can be retained after removing external actuation. Moreover, other types of deployable structures can also be designed through arranging multi-stable elements in different directions (see Fig. 1.4(b)). It is worth noting that the metastructure-based shape reconfiguration is able to realize a fast transition by the suddenly releasing stored elastic energy, which overcomes the challenge of slow transitions in some previous concepts, like shape-memory polymers and artificial muscles [33, 34].

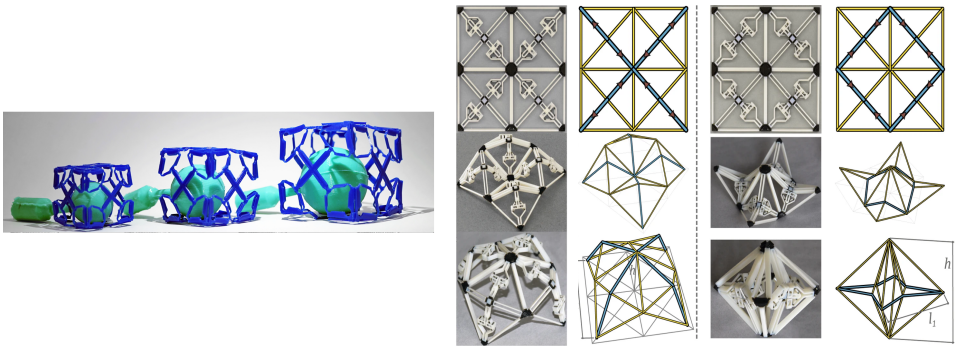

(a) (b)

Figure 1.4: Examples of multi-stable metastructure induced shape reconfiguration. (a) The translational motion enables a structure to deploy into a large self-stable deployed shape [35]. (b) Complex shape reconfiguration can be generated by various arrangements of structural elements with translational snap-through behavior [36]. Panel (a) is adapted under the terms of a Creative Commons Attribution License [35], Elsevier Ltd. Panel (b) is adapted under the terms of a Creative Commons Attribution License [36], Springer Nature.

Apart from structural deployment, multi-stability has been exploited in morphing structures. In this regard, many studies have investigated shape changes of a shell or a thin plate to realize different surface morphology. As a result, surface topography can be changed into a series of stable configurations, enabling to realize tunable functionalities, like optical properties [37]. For design such multi-stable shells or plates, various methodology has been proposed. For example, Dai *et al.* [38] demonstrated that by connecting a few bi-stable composite plates, several wavy stable configurations can be realized to morph a surface. Moreover, a method for constructing a monolithic plate has been proposed to achieve continuous morphing features [39]. For the bi-stable plates, it is still challenging to connect them to obtain a multi-stable plate because the interaction will have a significant influence on mechanical performance of the connected plate [40]. To overcome this problem, a few recent studies have focused on utilizing a variety of bi-stable mechanisms, such as trusses and hinges, to realize more complex deformations as well as stable configurations [41]. Currently, only few stable configurations, e.g., cylindrical shapes, have been presented. Studies on using multi-stable beam-type metastructures to realize surface morphing are scarce. In this dissertation, we explore this possibility and develop a type of multi-stable metastructure based deformable surfaces. Compared to previous studies based on bi-stable shells, the strategy proposed in this work can provide a wide range of wavy configurations and degrees of freedom.

1

1.2.3. ENERGY ABSORPTION

In addition to the motion-related applications, multi-stable metastructures have also been studied in terms of their energy dissipation, which opens the door for developing reusable shock absorbers. The energy dissipation arises from the serial arrangement of bi-stable elements, which makes effective properties of the multi-stable metastructures distinct from their unit cells (bi-stable elements). Specifically, the energy absorption is often quantified by a displacement-controlled cyclic loading in such a way that the multi-stable metastructures are able to realize a hysteresis loop, while the deformations of inner structures remain entirely within the elastic regime. In contrast, energy dissipation due to plastic deformations, such as honeycomb lattices and metallic foams, normally leads to inevitable structural damage.

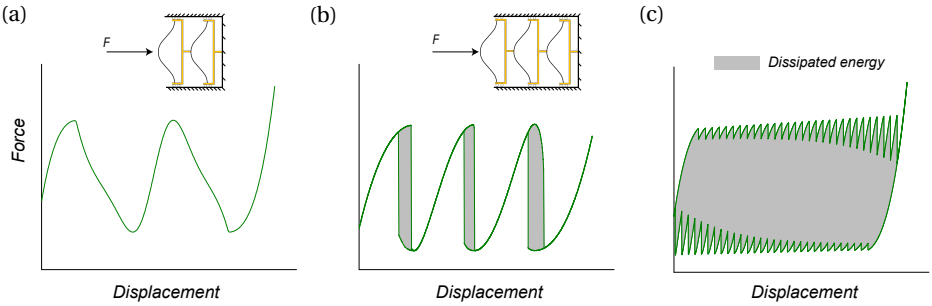

Figure 1.5: Energy absorption characteristics of multi-stable metastructures under displacement controlled cyclic loading. (a)–(c) Schematics of force-displacement curves (loading-unloading) for multi-stable metastructures consisting of 2,3, and 30 bi-stable elements.

The hysteresis characteristics of multi-stable metastructures are caused by a collective effect of both the snap-through and the serial arrangement of unit cells. As presented in Fig. 1.5(a), when two bi-stable elements are assembled in series, the displacement controlled loading and unloading curves follow the same path, indicating that no energy is dissipated under a loading cycle. When more elements are combined, in the displacement controlled loading, one element of the metastructure is unstable and thus free to move after reaching the critical load. As a result, a dynamic transition takes place during the quasi-static loading and the elastic energy is dissipated. This dissipation process is reflected in the force-displacement curves in such a way that when the number of unit cells is large enough, an hysteresis loop appears under cyclic loading. The amount of dissipated energy is dependent on the number of unit cells. That is, as more unit cells are assembled into the metastructure, the amount of absorbed energy per unit cell will increase and gradually converge to a maximum value, as demonstrated in Fig. 1.5(b)–(c). Thus, multi-stable metastructures consisting of a large number of serially arranged bi-stable elements are able to mimic the force plateaus.

Although previous works give important insights into metastructure's snap-through behavior and hysteresis characteristics, the associated energy dissipation capacity is restricted by the solid-beam design, for which the amount of absorbed energy is essentially governed by geometries of the beam's profile. To ensure snap-through and bi-stable be-

havior, geometric parameters have to be constrained within certain ranges. As a result, the solid beams generally lead to a fairly low strength and energy absorption, which limits their applicability. Moreover, the design freedom in previous work is limited. Therefore, it is of great significance to explore new designs to improve multi-stable metastructure's mechanical properties and energy dissipation.

1.3. AIM OF THIS RESEARCH

The main aim of this thesis is to investigate multi-stable beam-type metastructures in terms of their kinematics, energy absorption as well as shape reconfigurability, and to provide comprehensive understanding of the underlying mechanisms of the proposed designs. To realize this objective, several research goals are formulated:

1. *Design and model multi-stable metastructures that exhibit both translational and rotational stable states.*
2. *Develop designs to improve metastructures' energy dissipation.*
3. *Investigate functionalities of multi-stable metastructures in morphing surface.*

In the following chapters, we propose new concepts for multi-stable metastructures to exhibit novel and better mechanical properties. By using these strategies, a series of multi-stable structures that have not been studied before is explored systematically on the basis of theoretical, numerical and experimental analysis. Moreover, design principles and considerations for realizing improved structural performances are unveiled in detail, which gives a full identification of the proper design space. This study will help to open up new pathways for expediting applications of multi-stable metastructures in the field of energy absorption and shape-shifting.

1.4. THESIS OUTLINE

In this dissertation, research questions summarized above are answered in the following chapters. Each chapter except for Conclusions (**Chapter** 6) is structured based on either a published or submitted journal paper. Inevitably, this might result in some repetitions in the introduction of each chapter. As displayed in Fig. 1.6, the remaining chapters are divided into two parts: Part I is focused on the mechanical behavior of multi-stable metastructures, where the translational and rotational states are investigated via analytical and experimental studies. Part II mainly concentrates on functionalities of multi-stable metastructures, in which we develop different multi-stable metastructures for energy absorption and shape reconfiguration.

Chapter 2 investigates the methodology that enriches the kinematics of multi-stable metastructures. In particular, we integrate rotations into multi-stable metastructures so that rotational stable states can be realized, next to the intrinsic translational states. The rotational compliance and bi-stability of unit cells play key roles in realizing this additional rotational behavior. The predominant geometric parameters for reaching rotational stability are identified through a rigorous analytical analysis. Design criteria are defined subsequently. Besides, the newfound rotational states are validated by experimental tests to demonstrate their ability of shape reconfiguration.

1

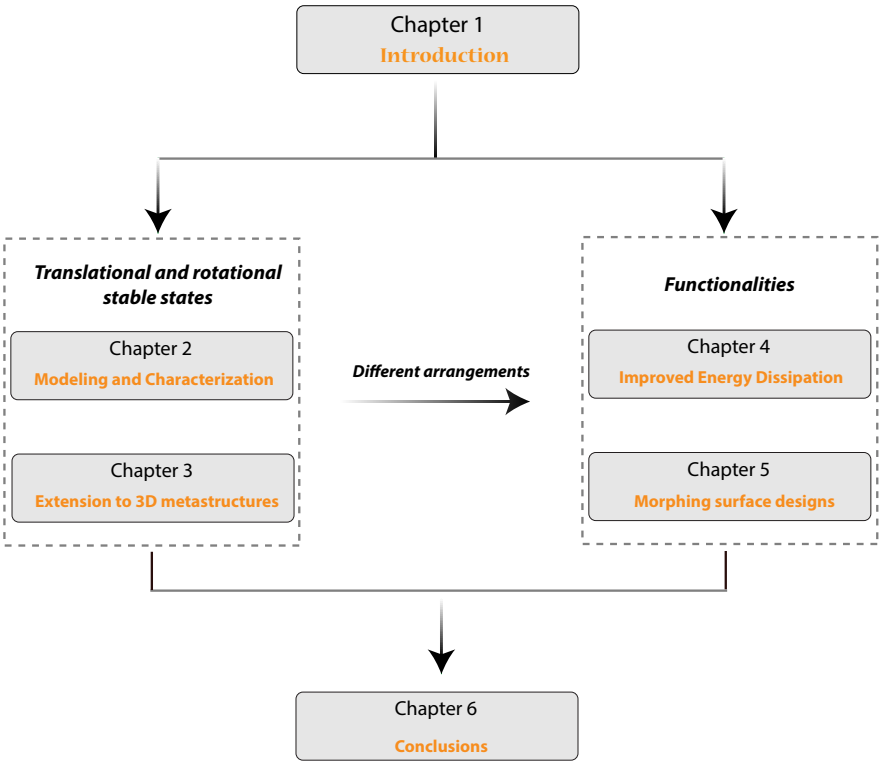

Figure 1.6: Visual outline of this thesis.

In addition, the concept of rotational compliance is further extended into 3D structural design, as presented in **Chapter 3**. The proposed three-dimensional multi-stable metastructures are capable of exhibiting both translational and rotational states in multiple directions. The translational and rotational transitions are compared in terms of snapping force and stability. Moreover, the effect of unit cell arrangements on rotational kinematics is investigated and different patterns for the unit cell arrangement (e.g., in series and parallel) are presented to investigate the allowable tilting directions.

Chapter 4 reports a class of multi-stable structures that are composed of curved beams with embedded lattices and with box-shaped cross sections. The proposed design enables metastructures to exhibit an enhanced bending stiffness, resulting in an improved energy dissipation efficiency as compared to the state-of-art. Specifically, key design parameters are identified, and their effects on snap-through, local buckling, and bi-stability are studied systematically. The improvements are further demonstrated and verified via experimental tests. Moreover, we demonstrate that the proposed design methodology is not restricted to beam-type structure and can be extended to develop shell structures.

With regard to shape reconfiguration, **Chapter 5** extends the application of metas-

tructures to morphing surfaces by developing a type of deformable surface exhibiting curved stable states in multiple directions. In order to probe the design space, an analytical model that captures the non-linear snap-through deformations is developed. Moreover, we design multi-stable metastructures based on two-dimensional arrangements of bi-stable elements. The resulting morphing surface induced by the multi-stable metastructures are characterized experimentally, where the relation between the arrangement of bi-stable elements and the accessible curved stable states is analyzed.

Finally, conclusions of this thesis are presented in **Chapter 6** and recommendations for future research are also discussed.

REFERENCES

[1] T. A. Schaedler and W. B. Carter, *Architected cellular materials,* Annual Review of Materials Research **46**, 187 (2016).

[2] H. Peng and P. F. Pai, *Acoustic metamaterial plates for elastic wave absorption and structural vibration suppression,* International Journal of Mechanical Sciences **89**, 350 (2014).

[3] S. Babaee, N. Viard, P. Wang, N. X. Fang, and K. Bertoldi, *Harnessing deformation to switch on and off the propagation of sound,* Advanced Materials **28**, 1631 (2016).

[4] X. Yu, J. Zhou, H. Liang, Z. Jiang, and L. Wu, *Mechanical metamaterials associated with stiffness, rigidity and compressibility: A brief review,* Progress in Materials Science **94**, 114 (2018).

[5] R. S. Lakes, *Negative-poisson's-ratio materials: auxetic solids,* Annual review of materials research **47** (2017).

[6] X. Ren, R. Das, P. Tran, T. D. Ngo, and Y. M. Xie, *Auxetic metamaterials and structures: a review,* Smart materials and structures **27**, 023001 (2018).

[7] Z. G. Nicolaou and A. E. Motter, *Mechanical metamaterials with negative compressibility transitions,* Nature materials **11**, 608 (2012).

[8] L. R. Meza, S. Das, and J. R. Greer, *Strong, lightweight, and recoverable three-dimensional ceramic nanolattices,* Science **345**, 1322 (2014).

[9] L. R. Meza, A. J. Zelhofer, N. Clarke, A. J. Mateos, D. M. Kochmann, and J. R. Greer, *Resilient 3d hierarchical architected metamaterials,* Proceedings of the National Academy of Sciences **112**, 11502 (2015).

[10] J. T. B. Overvelde, S. Shan, and K. Bertoldi, *Compaction through buckling in 2d periodic, soft and porous structures: effect of pore shape,* Advanced Materials **24**, 2337 (2012).

[11] B. Haghpanah, L. Salari-Sharif, P. Pourrajab, J. Hopkins, and L. Valdevit, *Multistable shape-reconfigurable architected materials,* Advanced Materials **28**, 7915 (2016).

[12] N. Hu and R. Burgueño, *Buckling-induced smart applications: recent advances and trends,* Smart Materials and Structures **24**, 063001 (2015).

[13] K. Bertoldi, *Harnessing instabilities to design tunable architected cellular materials,* Annual Review of Materials Research **47**, 51 (2017).

[14] K. Bertoldi, V. Vitelli, J. Christensen, and M. Van Hecke, *Flexible mechanical metamaterials,* Nature Reviews Materials **2**, 1 (2017).

[15] G. Simitses and D. H. Hodges, *Fundamentals of structural stability* (Butterworth-Heinemann, 2006).

[16] X. Liu, F. Lamarque, E. Doré, and P. Pouille, *Multistable wireless micro-actuator based on antagonistic pre-shaped double beams,* Smart Materials and Structures **24**, 075028 (2015).

[17] S. M. Montgomery, X. Kuang, C. D. Armstrong, and H. J. Qi, *Recent advances in additive manufacturing of active mechanical metamaterials,* Current Opinion in Solid State and Materials Science **24**, 100869 (2020).

[18] H. Y. Jeong, S.-C. An, Y. Lim, M. J. Jeong, N. Kim, and Y. C. Jun, *3d and 4d printing of multistable structures,* Applied Sciences **10**, 7254 (2020).

[19] A. Rafsanjani, K. Bertoldi, and A. R. Studart, *Programming soft robots with flexible mechanical metamaterials,* Science Robotics **4** (2019).

[20] S. Shan, S. H. Kang, J. R. Raney, P. Wang, L. Fang, F. Candido, J. A. Lewis, and K. Bertoldi, *Multistable architected materials for trapping elastic strain energy,* Advanced Materials **27**, 4296 (2015).

[21] S. Liu, A. I. Azad, and R. Burgueño, *Architected materials for tailorable shear behavior with energy dissipation,* Extreme Mechanics Letters **28**, 1 (2019).

[22] D. Restrepo, N. D. Mankame, and P. D. Zavattieri, *Phase transforming cellular materials,* Extreme Mechanics Letters **4**, 52 (2015).

[23] S. Sun, N. An, G. Wang, M. Li, and J. Zhou, *Snap-back induced hysteresis in an elastic mechanical metamaterial under tension,* Applied Physics Letters **115**, 091901 (2019).

[24] Y. Zhang, D. Restrepo, M. Velay-Lizancos, N. D. Mankame, and P. D. Zavattieri, *Energy dissipation in functionally two-dimensional phase transforming cellular materials,* Scientific reports **9**, 1 (2019).

[25] A. Rafsanjani, A. Akbarzadeh, and D. Pasini, *Snapping mechanical metamaterials under tension,* Advanced Materials **27**, 5931 (2015).

[26] C. S. Ha, R. S. Lakes, and M. E. Plesha, *Cubic negative stiffness lattice structure for energy absorption: Numerical and experimental studies,* International Journal of Solids and Structures **178**, 127 (2019).

[27] T. Frenzel, C. Findeisen, M. Kadic, P. Gumbsch, and M. Wegener, *Tailored buckling microlattices as reusable light-weight shock absorbers,* Advanced Materials **28**, 5865 (2016).

[28] X. Tan, S. Chen, B. Wang, S. Zhu, L. Wu, and Y. Sun, *Design, fabrication, and characterization of multistable mechanical metamaterials for trapping energy,* Extreme Mechanics Letters **28**, 8 (2019).

[29] H. Yang and L. Ma, *1d to 3d multi-stable architected materials with zero poisson's ratio and controllable thermal expansion,* Materials & Design **188**, 108430 (2020).

[30] H. Yang and L. Ma, *1d and 2d snapping mechanical metamaterials with cylindrical topology,* International Journal of Solids and Structures **204**, 220 (2020).

[31] Y. Song, R. M. Panas, S. Chizari, L. A. Shaw, J. A. Jackson, J. B. Hopkins, and A. J. Pascall, *Additively manufacturable micro-mechanical logic gates,* Nature communications **10**, 1 (2019).

[32] R. Baumgartner, A. Kogler, J. M. Stadlbauer, C. C. Foo, R. Kaltseis, M. Baumgartner, G. Mao, C. Keplinger, S. J. A. Koh, N. Arnold, *et al.*, *A lesson from plants: High-speed soft robotic actuators,* Advanced Science **7**, 1903391 (2020).

[33] T. Chen, O. R. Bilal, K. Shea, and C. Daraio, *Harnessing bistability for directional propulsion of soft, untethered robots,* Proceedings of the National Academy of Sciences **115**, 5698 (2018).

[34] A. Zareei, B. Deng, and K. Bertoldi, *Harnessing transition waves to realize deployable structures,* Proceedings of the National Academy of Sciences **117**, 4015 (2020).

[35] F. Bobbert, S. Janbaz, T. van Manen, Y. Li, and A. Zadpoor, *Russian doll deployable meta-implants: Fusion of kirigami, origami, and multi-stability,* Materials & Design , 108624 (2020).

[36] T. Chen, J. Mueller, and K. Shea, *Integrated design and simulation of tunable, multi-state structures fabricated monolithically with multi-material 3d printing,* Scientific reports **7**, 1 (2017).

[37] D. P. Holmes and A. J. Crosby, *Snapping surfaces,* Advanced Materials **19**, 3589 (2007).

[38] F. Dai, H. Li, and S. Du, *A multi-stable lattice structure and its snap-through behavior among multiple states,* Composite Structures **97**, 56 (2013).

[39] Y. Cui and M. Santer, *Highly multistable composite surfaces,* Composite Structures **124**, 44 (2015).

[40] Y. Cui and M. Santer, *Characterisation of tessellated bistable composite laminates,* Composite Structures **137**, 93 (2016).

[41] D. P. Holmes, *Elasticity and stability of shape-shifting structures,* Current opinion in colloid & interface science **40**, 118 (2019).

2

INCORPORATING ROTATIONS TO MULTI-STABLE METASTRUCTURES

The metastructures are able to generate translational motions due to the stacking of bi-stable unit cells. For some motion-driven applications, only exhibiting translations is not adequate, whereas rotational degrees of freedom are also required. In this chapter, we explore the rotational properties of multi-stable metastructures on the basis of both experimental and theoretical investigations, and define the conditions for achieving rotational stable states. Results show that the metastructure is able to realize both translational and rotational states, while the rotational transitions require less energy as compared to their translational counterparts. The influence of geometric parameters on rotational stability is investigated via parametric studies. Furthermore, to determine the design criteria for rotational stability, a theoretical investigation based on mode superposition principle is performed to predict the nonlinear-deformation of a unit cell. The theoretical analysis predicts well the rotational snap-through transitions that are observed in finite element simulations. It is found that the rotational stability is determined by setting proper values for h/L and t/L (h, t, L represent apex height, thickness and span of the bi-stable beam structure, respectively). Finally, we experimentally demonstrate that the proposed metastructure with multiple layers is able to achieve large rotations and translations.

This chapter is based on a journal paper: Zhang, Y., Tichem, M. and van Keulen, F., (2020). Rotational snap-through behavior of multi-stable beam-type metastructures. International Journal of Mechanical Sciences, 193, p.106172.

2.1. INTRODUCTION

The design of mechanical metastructures is a rapidly emerging field, because of the potential to create unusual mechanical properties, such as ultra-high stiffness but lightweight [1–5], negative Poisson's ratio [6–8], and negative thermal expansion [9–13]. These superior features are mainly realized by the rational design of their unit structures. For example, arranging unit cells in a re-entrant pattern can result in a negative Poisson's ratio of the macroscopic metastructure [14]. At present, a variety of mechanical metastructures have been proposed and intensively studied for various applications, including medical implants [15, 16], soft robots [17, 18], and microelectromechanical systems [19].

More recently, the strategy of utilizing buckling, which is generally avoided in classical structural designs, has been extensively reported in metastructural design [20–24]. The designed instability-based mechanical metastructures allow for large macroscopic deformations with recoverable shape changes, and thus they are also referred to as reconfigurable metastructures [25–28]. New functionalities, e.g. tuneable mechanical behavior, can be achieved by such metastructures. However, these transformations of geometry or reconfiguration usually require continuous power, in the sense that a continuous external actuation is necessary to maintain the deformed configuration. One way to improve energy efficiency is to introduce bi- or multi-stability, so that a structure maintains different states without the need for continuous energy supply. In designing such multi-stable metastructures, pre-shaped beams have been commonly adopted as basic elements since they have large loading-bearing capacity and can be easily manufactured via additive manufacturing [21, 29]. When an applied load reaches a critical level, the beam will jump from one configuration into another configuration, which is referred to as snap-through behavior [30]. By arranging multiple snapping beams, the associated metastructures are able to exhibit multiple self-stable configurations. Many examples of regularly assembled pre-shaped beams in one or two dimensions (1D or 2D), referred to as multi-stable beam-type metastructures (MBMs), can be found in literature [31–39].

In light of the stacking of the snapping beams with two stable configurations, MBMs are normally capable of achieving a large reversible switching motion, which has been utilized for energy absorption [40–43]. It has been demonstrated that the multi-stability can enhance the ability of reducing peak acceleration while MBMs are still reusable [44]. In addition, such MBMs, as reconfigurable structures, can be widely used for designing motion-driven mechanisms including deployable structures, shape-changing structures, actuators, soft robotics, and motion systems [45–50]. These motion-driven applications usually require multiple degrees of freedom and the monolithic multi-stable structures might offer a compact solution for such challenges. For instance, Chen *et al.* [45] presented a design for propulsion of soft robots, exploiting motions from the snapping of beams. Santer *et al.* [47] exploited 1D translational motion of a multi-stable structure to deploy a surface. Pontecorvo *et al.* [48] proposed the concept of using bi-stable elements to extend a helicopter rotor blade, based on the large translation of MBMs. Besides, Che *et al.* [51] designed a multi-stable beam-type structure using different materials for each layer to control its deformation sequences. The dynamic behavior of MBMs was also investigated to analyze its vibration modes [52]. However, most proposed MBMs are limited in terms of allowable directions and are only presented with their translational motions. Their potential to realize rotational stable states has not

been revealed and studied, and thus this limits their feasibility in motion-driven applications where rotational movements are typically needed, such as actuators, deployable structures and robotics.

To enrich multi-stable structure's reconfiguration capability, here we explore the possibility for MBMs to achieve rotational movements. This work aims to analyze the rotational behavior of MBMs and study design conditions for structures to realize additional rotational states. Although previous papers on MBMs give important insights into the mechanics of the translational transitions, the potential of rotational reconfiguration is restricted in most previous designs and little information is available on the rotational stability of MBMs. In this chapter, the rotational behavior of MBMs is characterized via experimental and numerical approaches, and the design requirements for rotational states are investigated via an analytical model, which can rapidly identify the design space for the rotational stability. The resulting multi-stable structures exhibit both translational and rotational motions, which can further enhance multi-stable mechanisms' deployment capacities. For instance, the rotational transitions can be exploited to design multi-stable bending actuators in which rotational degrees of freedom is essential, while the intrinsic translational state can be harnessed to provide extensions or contractions.

The remainder of this chapter is organized as follows. Section 2.2 describes the structural geometry of MBMs and methods we use in this work. The mechanical properties and resulting rotational stable states are characterized experimentally and numerically via a parametric study, as presented in Section 2.3. In Section 2.4, we conduct a theoretical analysis to investigate the rotational stability. Section 2.5 describes the mechanical behavior of multi-layer metastructures exhibiting large rotations and translations. Conclusions are presented in Section 2.6.

2.2. STRUCTURAL DESIGN AND METHODS

2.2.1. STRUCTURAL GEOMETRY AND STABLE STATES

The structural design of MBMs studied in this chapter is based on the snap-through behavior of curved beams, which were first studied by Vangbo *et al.* [53]. Here, pre-shaped curved beams are used as basic elements to construct multi-stable metastructures, as shown in Fig. 2.1. Each beam element illustrated in Fig. 2.1(b) is composed of a curved beam, upper and lower frame (marked in blue). The geometric parameters of the frames are shown in the inset table and are fixed in this study. The original shape ($w_0(x)$) of the curved beam illustrated in Fig. 2.1(b) can be expressed as:

$$w_0(x) = \frac{h}{2}(1 - cos(2\pi\frac{x}{L})) \tag{2.1}$$

where h and L represent initial beam height and length, respectively. The beam's in-plane thickness and out-of-plane thickness are denoted as t and b, respectively. These three parameters (h, L, and t) are considered as design parameters and their influence on rotational behavior is systematically discussed in this chapter. As illustrated in Fig. 2.1(a), by serially combining multiple beam elements, MBMs can be designed.

The resulting metastructures and their stable states are demonstrated in Fig. 2.1(c), where the representative unit is referred to as a unit cell that consists of two beam el-

ements: left and right beam element, as denoted in the figure. The unit cell can deform into flat or tilted stable configurations. These flat and tilted stable configurations are referred to as translational and rotational states respectively in the remainder of this chapter. The unit cell possesses four stable configurations: the initial state and three deformed stable states including one translational and two rotational stable states. When the unit cell switches from the initial to the translational state, both beams undergo the same deformations and snap to the second stable state. Therefore, the behavior of translational transitions can be obtained based on a study for one side, either the left or right beam element. However, symmetry breaks up during the transition to the rotational state, where both curved beams deform with different manners. In particular, the left beam element snaps while the right beam element is mainly rotated. The resulting rotational state is enabled by a collective effect of the left beam element's snapping deformations and rotational deformations of right beam element. Consequently, mechanics and design requirements for the proposed rotational state are different from that of translational transitions. To establish the design criteria for reaching rotational states, an analytical study is performed in Section 2.4.

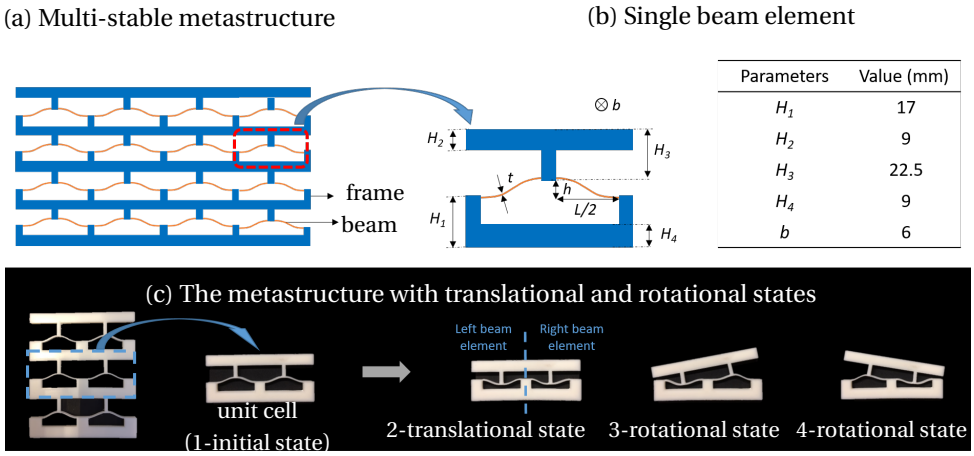

Figure 2.1: A demonstration of multi-stable structures with translational and rotational stable states. (a) A schematic for the proposed multi-stable metastructure. The structure is designed by serially stacking curved beams with thick frames. (b) Geometric parameters of the beam element are depicted. The out-of-plane dimension is denoted as b. (c) Each unit cell ($h = 5$mm $t = 0.8$mm and $L = 28$mm) possesses four stable states such that it can snap into the translational state or the rotational states.

2.2.2. FABRICATION AND EXPERIMENTAL TESTS

To study the proposed multi-stable metastructures' behavior, a series of samples were fabricated via a fused deposition printer using flexible thermoplastic polyurethanes (TPU, Flex-45, RS). TPU is an environmental friendly material with advantages of good wear resistance and large recoverable elastic strains. Its properties were characterized by standard tensile measurements according to ASTM D638-14 [40]. The measured Young's modulus (E) and Poisson's ratio (ν) are 95 MPa and 0.4, respectively. The correspond-

ing stress-strain curve is plotted in Fig. 2.2(a).

Uniaxial loading tests were conducted to characterize metastructures' snap-through transitions as load-displacement curves. Quasi-static loading conditions were applied using a universal testing system (ZwickRoell Z005) with a loading rate of 10 mm/min in a displacement-control manner. For each sample, multiple tests were conducted to get average load-displacement curves. Extra parts used for connecting samples to the testing system were designed and printed using polylactic acid (PLA), as seen in Fig. 2.2(b). To allow for unit cells' rotations during uniaxial testing, two rigid parts were assembled using screws to mimic hinge connections. Loads were applied on one side of the frame. For characterizing translational motions, clamped conditions were applied between specimens and the extra parts, as displayed in Fig. 2.2(b).

2.2.3. NUMERICAL METHODS

Finite element models were established by using software ABAQUS/Standard (2017) to examine the structures' mechanical behavior, where geometric parameters are in accordance with those of experiments. A Marlow hyper-elastic material model was adopted as a constitutive relation in finite element analysis (FEA) [54]. Here, the stress-strain curve shown in Fig. 2.2(a) was imported to ABAQUS. Eight-node brick elements (C3D8) were used to mesh the structure geometry, with mesh convergence analysis performed to ensure accuracy. Nonlinear geometric FEA based on static/general procedure was conducted by prescribing vertical displacements at specific loading points on the top of the unit cell, which is consistent with the experimental compression tests shown in Fig. 2.2(b). The bottom of the structure is fully fixed in x, y, z directions. The reaction forces were collected in each iteration from nodes where vertical displacements were applied.

2.3. MECHANICAL RESPONSE FOR ROTATIONAL TRANSITIONS

In this section, we characterize the rotational transitions of the representative element, which is the unit cell defined before. Moreover, a parametric study is performed to investigate the influence of primary geometric parameters.

2.3.1. CHARACTERISTICS OF SNAP-THROUGH BEHAVIOR

The force and vertical displacement of loading points shown in Fig. 2.2(b) are denoted as F and d, respectively. The measured force and displacement are then normalized by Ebt and h, respectively. Figure 2.2(c) shows force-displacement curves for translational and rotational snap-through behavior. It can be observed that there is a good quantitative agreement between experimental and numerical results. Negative stiffness is captured in both translational and rotational transition curves. The force first gradually increases along with the displacement and then instability (i.e. snapping) is triggered when reaching the maximum force (denoted as F_{max}). Under force-control loading condition, snap-through behavior typically exhibits "displacement jump" after reaching F_{max}. In this work we apply displacement-control loading condition to capture the full force-displacement curve shown in Fig. 2.2(c), with a negative stiffness phase (the yellow region in the figure). In this chapter, we refer to this negative stiffness phase as

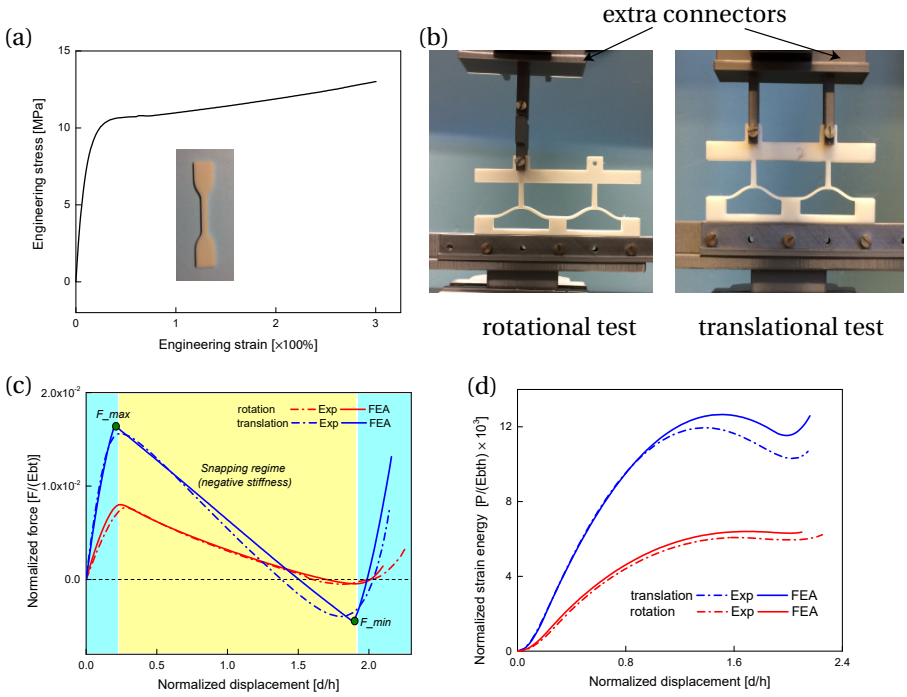

Figure 2.2: Characterization of snap-through transitions of the unit cell. (a) Stress-strain results for the material we used. (b) Experimental setup for measuring rotational (left) and translational (right) transitions. Samples are clamped at the bottom and connected to the printed part at the top. (c) Normalized load-displacement curves of snap-through transitions. The blue regions represent positive stiffness phases while the yellow area stands for the snapping phase, exhibiting negative stiffness. F_{max} and F_{min} represent the maximal and minimal force of each load-deflection curves, respectively. (d) Evolution of the normalized strain energy of the unit cell during the uniaxial loading.

snap-through transitions. F_{min} represents the minimum force in the force-displacement curve. In this figure, the magnitude of F_{max} for translation is approximately two times larger than for rotation. This is due to the fact that in case of translational transitions, two beams undergo bending and compression deformations, while for the case of rotations mainly the beam near the loading position deforms. Moreover, the minimum force F_{min} for translation is also higher than for rotations as a result of deformations of two beams. This implies that recovering from the translational to the initial state needs larger force as compared to reversing the rotational state. In addition, we assess the symmetry of snap-through transition by defining a quantity $\eta = |F_{max}/F_{min}|$. When η is close to 1, the structure intends to exhibit symmetric transitions. Here, the η for translational transitions in Fig. 2.2(c) is 3.95, whereas the counterpart of rotational curve is 15.24. This indicates that the unit cell's rotational deformation exhibits a more evident asymmetric characteristic as compared to translational deformations. The highly asymmetric behav-

ior of rotations is attributed to two aspects: the snapping deformation of the left beam element and right beam's rotational deformations, as discussed in Section 2.2.

The evolution of strain energy (P) during the loading process is shown in Fig. 2.2(d). P is equal to the area under the corresponding force–displacement curve. It indicates that both the translational and rotational state transitions exhibit a local minimum in the energy landscape, which correspond to the deformed (translational and rotational) stable states. The rotational snap-through (negative stiffness) can be understood as: by applying prescribed displacements as shown in Fig. 2.2(b), the right beam element is mainly bent. The left beam element experiences bending and compression deformations, where the compression energy first increases and then decreases, leading to the decline of the unit cell's strain energy. In addition, it can be observed that the energy of deformed stable state is larger than that of the initial undeformed state, which implies a sufficiently large disturbance may cause the structure to switch back to its initial state that has a lower potential energy.

2.3.2. INFLUENCE OF GEOMETRIC PARAMETERS ON ROTATIONAL STATES

For multi-stable metastructures, tuning geometric parameters can result in different mechanical properties including strength, stiffness and stability. Rotational behavior of these metastructures is mainly controlled by the beams' geometric parameters defined before: the beam height (h), the thickness (t) and the length (L). Here, parametric studies are carried out for unit cells' rotational transitions and a series of unit cells with different parameters is tested. Moreover, we have characterized the tangent slope of each force-displacement curve for the initial and rotational state. k_0 and k_1 are referred to as the tangent slope of each force-displacement curve at the points corresponding to the initial and rotational state, as illustrated in Fig. 2.3(a). Similarly, when varying h and L, k_0 and k_1 can also be quantified for the corresponding load-displacement curves.

THICKNESS VARIATION

Results of the unit cells' rotational transitions with different thickness (t) are presented in Fig. 2.3(a)–(c). Figure 2.3(b) shows the change of F_{max} and F_{min} versus the variation of thickness. The minor deviations between experimental and numerical results are mainly attributed to manufacturing imperfections and local defects introduced during printing. It can be seen that F_{max} is increasing dramatically with respect to the change of thickness. This is due to the fact that both bending and compression energy of the unit cell increase monotonically with the increasing of t. The variation of minimum force (F_{min}) shows a small distinction as compared to that of F_{max}. Nevertheless, it is clear that when thickness is large, the corresponding F_{min} is a positive value, which means that the structure switches back to the initial state after removal of load. This is verified in FEA (shown in Fig. 2.3(b)) as well as experimental demonstrations such that unit cells with small t can realize self-stable rotational states while the unit with a thickness of 1.6 mm recovers back to the initial state upon removing the load. This shows that t is crucial for rotational stability. Moreover, results in Fig. 2.3(c) show that the stiffness k_0 increases monotonically when t increases. However, k_1 first increases and then dramatically decreases when t is larger than 1.38 mm in this case. This indicates that the unit cell possesses tunable stiffness, which is related to its multiple stable states.

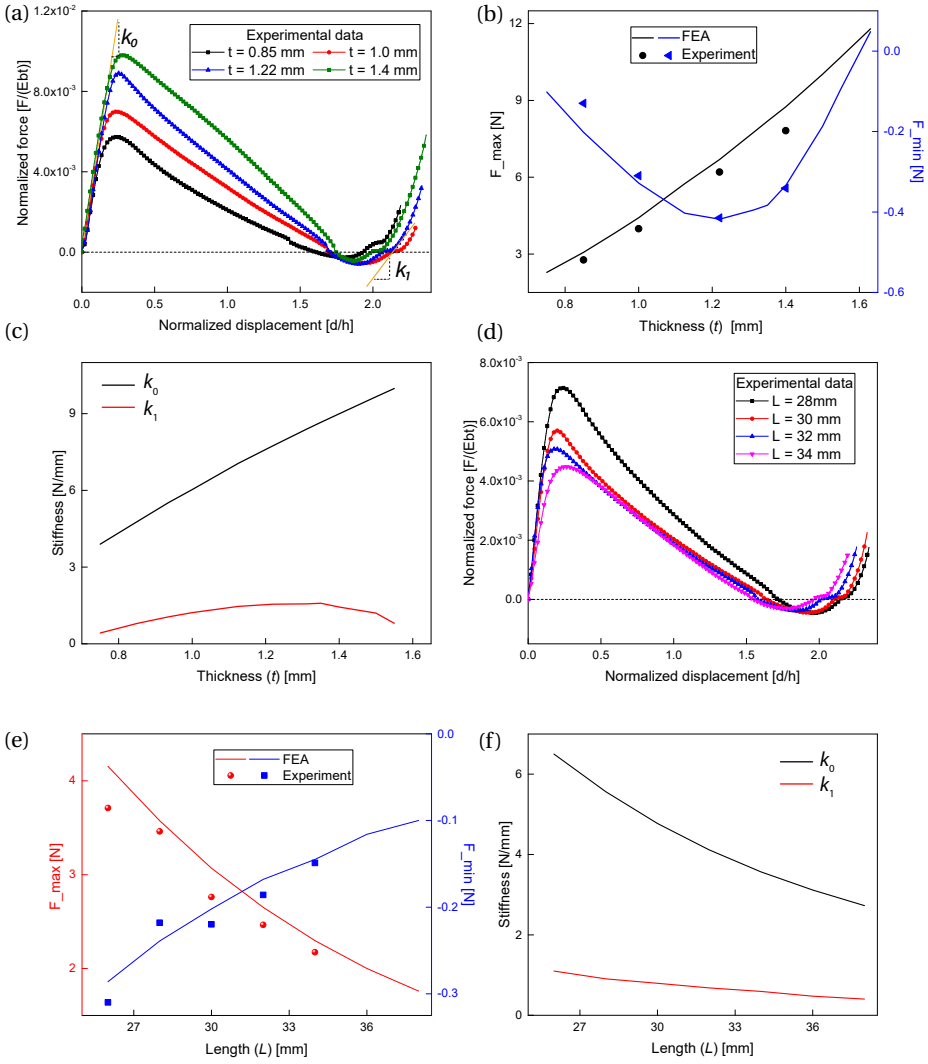

Figure 2.3: The influence of geometric parameters on rotational responses. (a)–(c): The effect of t on rotational transitions. (a) shows experimentally measured load-displacement curves for specimens with different thickness. k_0 and k_1 are defined as the slope of tangent line (orange color) at two stable locations (the initial and rotational state). (b) presents F_{max} and F_{min} of force-displacement curves as a function of thickness. The positive sign of F_{min} indicates that the rotational stable state does not exist. (c) represents the change of k_0 and k_1 when varying thickness in FEA. (d)–(f): The effect of L on rotational transitions.

LENGTH VARIATION

Figure 2.3(d)–(f) display the influence of the beam length (L) on rotational properties while keeping other parameters unchanged. Results show that the value of F_{max} decreases with the increase of L, while F_{min} is increasing. Similar characteristics can be captured for both k_0 and k_1 that stiffness decreases when L is increased. Furthermore, it can be seen from Fig. 2.3(e) that the slope of the F_{min} curve gradually decreases. As compared to the effect of t, the beam length L has minor effects on the sign of F_{min}, which is still negative despite its magnitude is decreasing. Similarly, it was also found that L has minor influence on the sign of F_{min} of translational transitions [55]. It should be mentioned that this effect of L is only applicable for shallow and thin beams, where L is much larger than h and t.

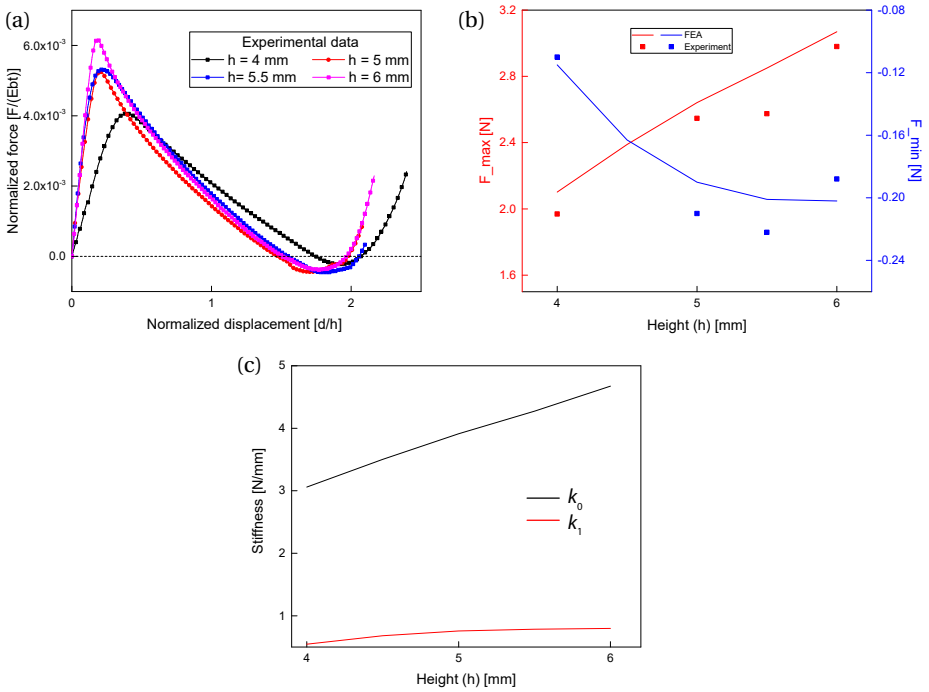

Figure 2.4: The influence of height (h) on rotational responses.

HEIGHT VARIATION

Results presented in Fig. 2.4 show that the beam height (h) has a different influence on the rotational behavior. The effect can be summarized as: *i*) F_{max} increases with an increasing of h, similar to the effect of t; differently, the F_{max} curve gradually increases in a linear manner (see Fig. 2.4(b)). *ii*) When enlarging h, F_{min} and the slope of F_{min} curve decrease, as shown in Fig. 2.4(b). *iii*) The changes of k_0 and k_1 displayed in Fig. 2.4(c) exhibit different characteristics. The k_0 increases with increasing h in a proportional manner, while the k_1 increases with a small rate of change. This relation results from the

energy variation of the unit cell, where the height (h) influences both initial curvature and length of the beam. Changing the geometric parameters can control the variation of elastic energy during deformations. The tunability of stiffness offers the potential to tune structures' dynamic behavior by switching into different stable states.

2.4. DESIGN CRITERIA FOR ROTATIONAL STATES

From the previous section, it is found that geometric parameters (t, L, h) affect rotational transitions in different manners. With changing these parameters, the rotational response can shift from stabilizing at the rotational states ($F_{min} < 0$) to switching back to the initial state (no rotational states, $F_{min} > 0$). In order to explore the design space for realizing rotational stable states, we present an analytical investigation of the rotational behavior on the basis of parameters defined before.

2.4.1. MODEL FORMULATION

The theoretical analysis is established for the unit cell's rotational transitions by combining buckling modes of the beam elements. It has been reported in literature that utilizing buckling modes can provide a good estimation of load-displacement responses for the snapping beams [35, 56–58]. Here, since the unit cell undergoes both symmetric and asymmetric deformations (see Fig. 2.5(a)), dominant modes (symmetric Mode 1 and asymmetric Mode 2) are employed to construct displacement fields, as displayed in Fig. 2.5(b). Based on the assumed displacement field, the potential energy is then formulated to derive the governing equations.

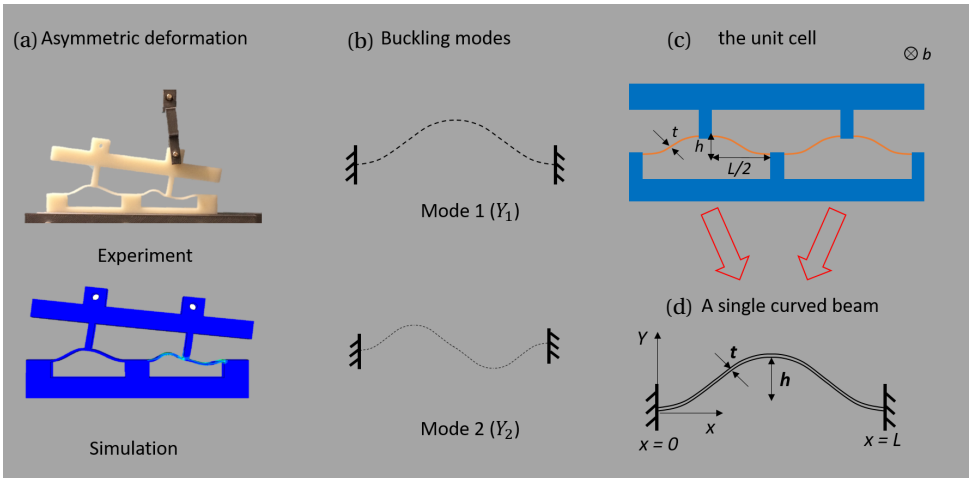

Figure 2.5: Modeling a single beam based on buckling modes. (a) The rotational transitions observed in both experiments and FEA show evident asymmetric deformation modes. (b) The first two buckling modes (Mode 1 and 2) for a clamped-clamped beam. These modes are employed as bases to approximate the displacement field. (c) Geometry of the unit cell. (d) Illustration of a single curved beam. Each beam of the unit cell is modeled as a single beam. Based on the X-Y coordinate in the figure, the first two buckling modes are described by function Y_1 and Y_2, respectively.

ELASTIC ENERGY FOR A SINGLE BEAM

We first derive energy formulas for each single clamped-clamped pre-shaped curved beam illustrated in Fig. 2.5(d), and formulate the model for the unit cell. The beam's geometric parameters are depicted in Fig. 2.5(d), with $X-Y$ coordinate defined. According to Euler–Bernoulli equations [59], the first and second buckling modes of a straight beam that is axially compressed to buckle are given as:

$$Y_1 = 1 - \cos(N_1 \frac{x}{L}) \text{ with } N_1 = 2\pi, \tag{2.2}$$

$$Y_2 = 1 - 2\frac{x}{L} - \cos(N_2 \frac{x}{L}) + \frac{2}{N_2}\sin(N_2 \frac{x}{L}), \tag{2.3}$$

where N_2 is the first positive solution of equation $\tan(N_2/2) = N_2/2$. The deformed beam shape (Y) under a given load is described as:

$$Y = A_1 Y_1 + A_2 Y_2 \text{ and } Y_0 = \frac{h}{2} Y_1, \tag{2.4}$$

$$d = Y_0 - Y, \tag{2.5}$$

where Y_0 is the initial beam shape and d is the displacement of the beam. A_1 and A_2 are unknown coefficients, which need to be solved on the basis of the principle of minimum energy. The elastic energy for the curved beam is obtained, which includes bending energy (U_b) and compression energy (U_c). The bending and compression energy is derived respectively by:

$$U_b = \frac{EI}{2}\int_0^L (\frac{d^2Y}{dx^2} - \frac{d^2Y_0}{dx^2})^2 dx \text{ where } I = \frac{bt^3}{12}, \tag{2.6}$$

$$U_c = \frac{Ebt(\Delta s)^2}{2L} \text{ and } \Delta s = s - s_0. \tag{2.7}$$

Here, s is the beam's total length at any position, while s_0 is the beam's initial length. Assuming small deformations, s can be approximated as:

$$s = \int_0^L \sqrt{1 + (\frac{dY}{dx})^2}\, dx \approx \int_0^L [1 + \frac{1}{2}(\frac{dY}{dx})^2] dx. \tag{2.8}$$

By combining eqns. (2.7) and (2.8), U_b and U_c can be expressed as a function of A_1 and A_2, as shown in eqns. (2.9)–(2.10). C_1, C_2, D_1, D_2 are constants, which follow from integrations along the x axis (see Appendix A.1).

$$U_b = \frac{EI}{2L^3}[(-h\boldsymbol{A_1} + \boldsymbol{A_1^2} + \frac{h^2}{4})C_1 + \boldsymbol{A_2^2}C_2]. \tag{2.9}$$

$$U_c = \frac{EA}{8L^3}\{D_1^2\boldsymbol{A_1^4} + D_2^2\boldsymbol{A_2^4} + 2D_1D_2\boldsymbol{A_1^2}\boldsymbol{A_2^2} - \frac{h^2D_1^2}{2}\boldsymbol{A_1^2} - \frac{h^2D_1D_2}{2}\boldsymbol{A_2^2} + \frac{h^4D_1^2}{16}\}. \tag{2.10}$$

MODEL THE UNIT CELL

Based on the derived formulation for a single beam, we now build the model for the unit cell which is composed of two pre-shaped beams connected by frames. The geometric parameters of the unit cell are illustrated in Fig. 2.6, where each beam's shape (represented as left and right unit) is modeled using the formula derived in Section 2.4.1. Specifically, each beam's geometry is determined by t, L, and h, which are the same notations used before. The vertical branch denoted in Fig. 2.6(a) represents the vertical part of the upper frame, with dimensions depicted as H and W. As observed in simulation, this vertical branch is bent during loading, as shown in Fig. 2.6(b). Therefore, the bending energy of the branch is taken into account in the following energy formulation. The unit is compressed by a load (F) at point A, as illustrated in Fig. 2.6(a). The angle of the upper frame is depicted as θ.

(a) Model geometry

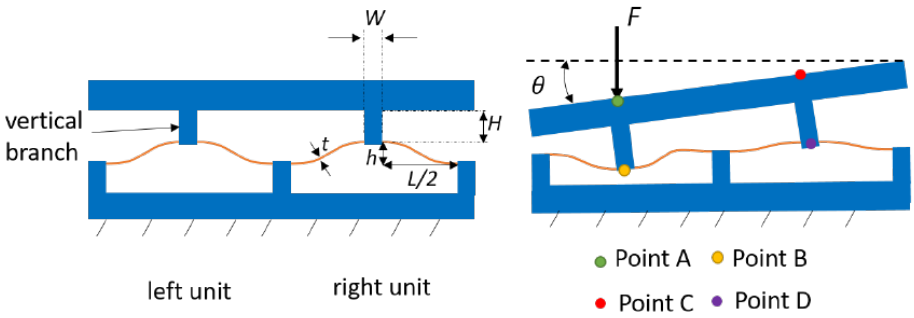

(b) Bending of the vertical branch

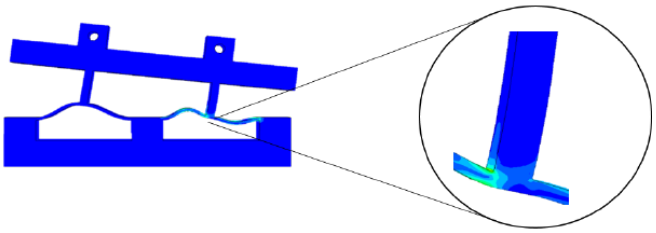

Figure 2.6: Model the rotational deformation of the unit cell. (a) Unit cell's geometry and predefined parameters. b is the out-of-plane dimension. (b) As observed, the vertical branch is bent during rotational transitions. The associated bending energy is taken into account when calculating the total potential energy of the system.

a. Kinematics

As discussed in the previous section, the left and right beam's shape (denoted as Y^L and Y^R) can be described as:

$$Y^L = {A_1}^L Y_1 + {A_2}^L Y_2 \text{ and } Y^R = {A_1}^R Y_1 + {A_2}^R Y_2, \tag{2.11}$$

where Y_1 and Y_2 are the first two buckling modes, as defined before. ${A_1}^L$, ${A_2}^L$, ${A_1}^R$, ${A_2}^R$ are unknown factors, which need to be solved. The displacement of each beam's midpoint (Point B and D), denoted as d^B and d^D, can be expressed as:

$$d^B = h - 2{A_1}^L, \ d^D = h - 2{A_1}^R. \tag{2.12}$$

Kinematic relationship between the vertical displacement of Point A (denoted as d^A) and C (denoted as d^C) is presented in eqns. (2.13). The relation between ${A_1}^L$ and ${A_1}^R$ is derived, as shown in eqns. (2.14).

$$d^A = d^C + L_x \sin(\theta), \tag{2.13}$$

$${A_1}^L = {A_1}^R - \frac{L_x \sin(\theta)}{2} \approx {A_1}^R - \frac{L_x \theta}{2}, \tag{2.14}$$

where L_x is the distance between Point A and C, which is a constant value.

b. Total potential energy

The total potential energy for the unit under the point-force loading is formulated to obtain the four unknown coefficients (${A_1}^L$, ${A_2}^L$, ${A_1}^R$, ${A_2}^R$). There are four energy contributions, which are the bending energy of left and right beam (${U_b}^L$ and ${U_b}^R$), the compression energy of left and right beam (${U_c}^L$ and ${U_c}^R$), the bending energy of vertical branch (U_v) and potential energy (U_e).

${U_b}^L$, ${U_c}^L$ can be derived by substituting ${A_1}^L$, ${A_2}^L$ for A_1 and A_2 in eqns. (2.9) and (2.10) (see Appendix A.2). Similarly, by combining eqns. (2.9), (2.10) and (2.14), we can get the expression of ${U_b}^R$, ${U_c}^R$, as a function of ${A_1}^L$, ${A_2}^R$ and θ. Finally, there are four independent unknown variables (${A_1}^L$, ${A_2}^L$, θ, ${A_2}^R$) in the governing equations. Moreover, the bending energy of the vertical branch can be expressed as:

$$U_v = \frac{EI_B(\frac{A_2^L C_s}{L} + \theta)^2}{2H} + \frac{EI_B(\frac{A_2^R C_s}{L} + \theta)^2}{2H}, \tag{2.15}$$

where EI_B represents the bending stiffness of the vertical beam and C_s is a constant value, as shown in the Appendix A.2. The potential energy, associated to applied force, is simply:

$$U_e = -Fd^A. \tag{2.16}$$

Finally, the total potential energy is:

$$U_{tot} = {U_b}^L + {U_c}^L + {U_b}^R + {U_c}^R + U_v + U_e, \tag{2.17}$$

and the governing equations are obtained by taking the derivative of U_{tot} with respect to four variables (${A_1}^L$, ${A_2}^L$, θ, ${A_2}^R$). The equations are then solved numerically by giving a range of F inputs. Consequently, the corresponding load-displacement ($F - d^A$) curves can be extracted.

2.4.2. RESULTS OF THE ANALYTICAL MODEL

The corresponding load-displacement curves predicted by the analytical model are presented in Fig. 2.7(a). It can be seen that the model gives a good approximation of rotational snap-through characteristics that are observed in FEA. Specifically, the theoretical results exhibit the same slope as that of FEA in the negative stiffness phase. This can be explained by the fact that snapping behavior is mainly determined by the asymmetric Mode 2, which has been used as a modal basis in the analytical formulation. Meanwhile, it is shown that the deformed stable position of the rotational state is well predicted by the model. As compared to the FEA results, higher stiffness are observed in this model's predictions. The differences are mainly caused by two factors. First, the theoretical model does not consider high order buckling modes since using dominant modes already allow to capture the characteristic of snap-through deformation at the snapping phase, which is our focus in this study. Second, the model is based on small deformation hypothesis, as reflected in the energy formulations.

The design criterion for the rotational stability is presented in Fig. 2.7(b), based on two non-dimensional quantities (h/L and t/L). The grey region in the figure is corresponding to the case that the structure cannot stabilize at the deformed rotational state, where F_{min} is a positive value. The colored region means that the unit is able to achieve rotational stable states by setting proper h/L and t/L. Geometrical thresholds along the boundary are highlighted as green dots, which are denoted as t_b/L_b and h_b/L_b. The t_b/L_b and h_b/L_b obtained from the model are compared with FEA, as shown in Fig. 2.7(d). It is shown that the model is able to give a reasonable prediction of the boundary that determines the rotational states. Therefore, it allows a rapid and full identification of the design space for rotational stability before manufacturing.

In addition, from Fig. 2.7(b), it can be noted that for a specified thickness, the rotational stable state can be realized when h/L of the structure is larger than the h_b/L_b. In order to reach the rotational stable state, h/L should be larger than the critical value while t/L should not exceed a specific value. It can also be interpreted in the sense that h/t should be large for achieving the rotational stable states. Besides, we explore the variation of F_{max} with respect to t/L and h/L, and results are plotted in Fig. 2.7(c). As compared to h/L, t/L has a more substantial influence on F_{max}. That is, the value of F_{max} increases dramatically with the change of t/L, while the change of h/L does not influence F_{max} much. Therefore, it is more paramount to change the parameter t/L when the maximal actuation force needs to be tuned to accommodate different circumstances.

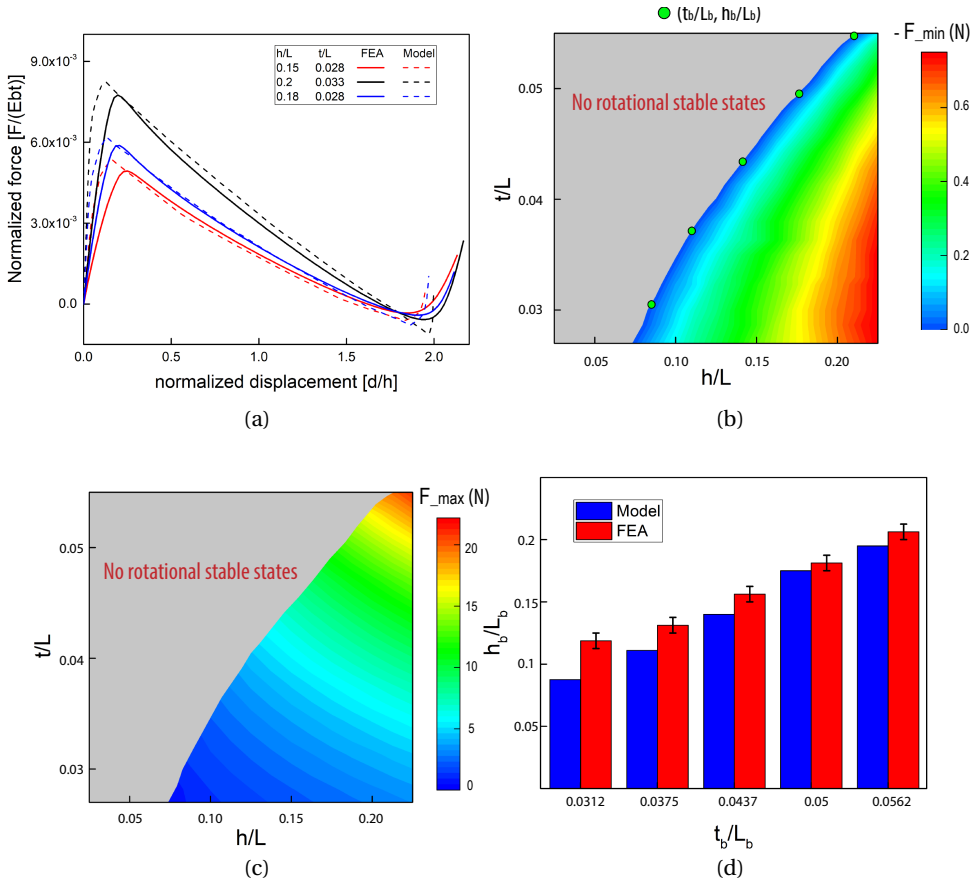

Figure 2.7: Identification of design space for rotational stable states as a function of t/L and h/L. (a) Theoretical predicted load-displacement curves for the units with different parameters. FEA results are used as references. (b) With changing t/L and h/L, the design space for rotational stable states is identified by the model. The grey area represents the situation, in which there are no rotational stable states; the colored region represents the range of parameter values, for which the structure does have rotational stable states. Green dots are specific data points (denoted as t_b/L_b and h_b/L_b) along the boundary. (c) The change of F_{max} with respect to t/L and h/L. (d) The t_b/L_b and h_b/L_b predicted by the model and FEA, respectively. The error bars marked in FEA represent that the simulated h_b/L_b that is exactly corresponding to $F_{min} = 0$ is located between the upper and lower limits.

2.5. MULTI-LAYER METASTRUCTURES WITH ROTATIONS

Via rationally designing the beam with specific geometric parameters, we can obtain the desired rotational states as well as the intrinsic translational states for the unit cell. By assembling such units in series, metastructures with multiple layers can be designed, which are able to exhibit large rotations and translations. To demonstrate the feasibility of the multi-layer metastructurese, we experimentally characterize their snapping transitions.

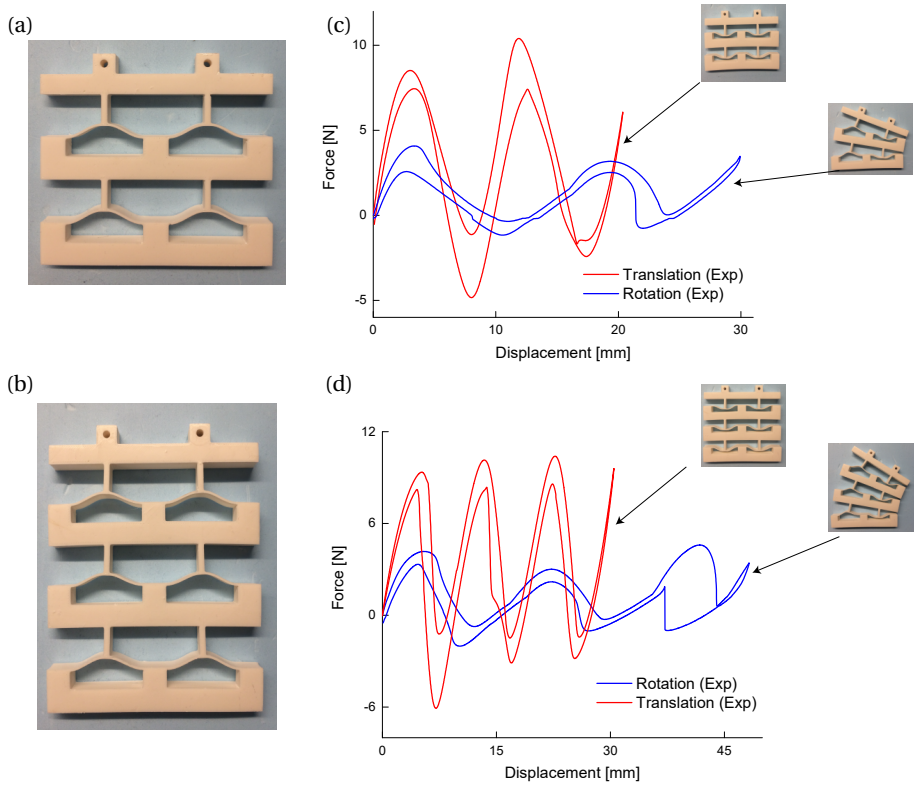

Figure 2.8: 2D multi-layer metastructures with serial arrangements of unit cells. (a) A two-layer metastructure. (b) A three-layer metastructure. (c) Experimentally characterized load-displacement curves for the translational and rotational snap-through of the two-layer metastructure. The metastructure can stabilize at their deformed states, as shown in the figure. (d) Snap-through responses of the three-layer metastructures. The translational and rotational transitions are characterized respectively.

Two-layer and three-layer metastructures are displayed in Fig. 2.8(a)–(b). As the unit cell possesses four stable states, the printed two-layer and three-layer metastructures have 4^2 and 4^3 stable states, respectively. Here, two primary deformation modes are selected and characterized by cyclic loading. The associated load-displacement responses are plotted in Fig. 2.8(c)–(d), where each layer exhibits evident snap-through behavior

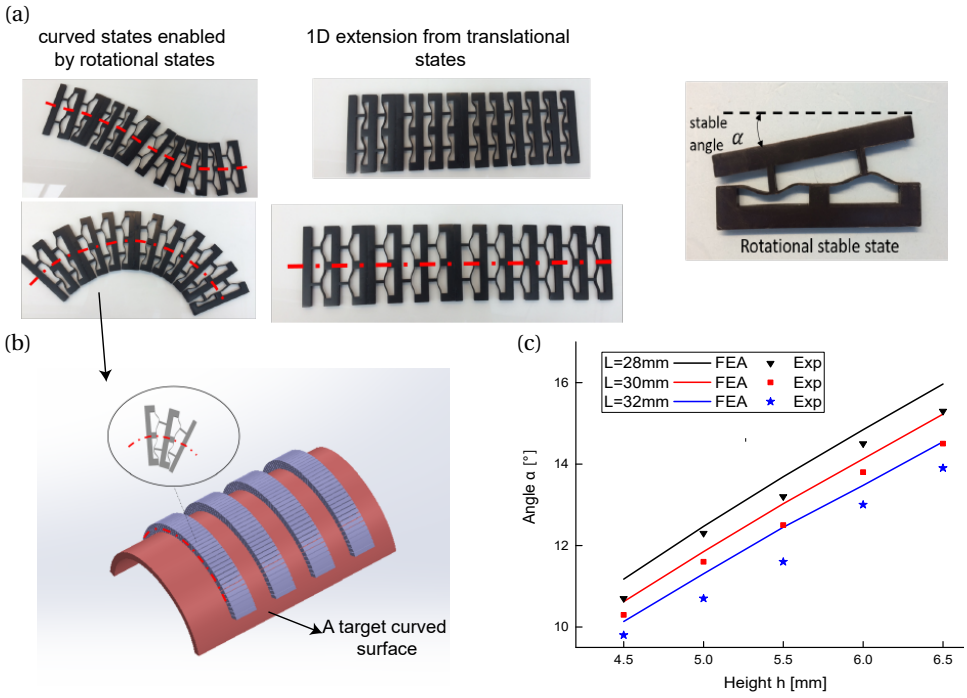

Figure 2.9: Demonstrations of conformal-morphing on a curved surface based on the rotational stable states. (a) An ensemble of unit cells stacked in series. By deforming in different transition modes, it can switch to curved shapes with different curvatures. The angle α is the stable angle achieved by a single unit's rotational transitions. (b) An illustrative example of conformal morphing on a spatial free-form surface. To realize shape-matching, our deformed metastructures (grey) can deform into a curved shape to match the target curved free-form shape (red). (c) The stable angle (α) is characterized experimentally and numerically, as a function of h for different L.

sequentially. In Fig. 2.8(d), a large difference between loading and unloading during the third snapping occurs. This happens due to the fact that during uniaxial loading, the top layer of the three-layer metastructure also generates a horizontal displacement, which can not be handled by the uniaxial testing. In terms of characterizing the rotations of a metastructure with more layers, the horizontal displacement of the metastructure needs to be taken into account. The multi-stable metastructures are able to stabilize at their deformed (translational and rotational) states after removal of loads. After unloading, the metastructure can be fully reversed back to the initial state, which means that they can be reused.

More importantly, from a kinematics perspective, the proposed multi-stable structure is capable of not only providing translational but also angular movements, which enriches the structure's shape-morphing ability. As shown in Fig. 2.9(a), the multi-layer metastucture can exhibit different curved shapes that are enabled by the unit's rotational states, aside from the 1D extension shown in this figure. Such deformed curved states can be useful for shape morphing, in which the ability to deform into curved shapes is

normally needed. An illustrative example is shown in Fig. 2.9(b), where conformal morphing can be realized. To match a target curved shape (denoted in red), it is possible to make the metastructures (marked in grey) deform to fit into the shape of the target curved shape via controlling the rotational stable state of each unit cell, while the translational states of the presented structures shown in Fig. 2.9(a) cannot realize the morphing behavior to match the curved surface. The largest rotational angle can be calculated as $n\alpha$, where n is the number of layers. Since the beam height (h) and length (L) have more substantial effects on α than the thickness (t), we plot the change of α with the variation of h and L, as shown in Fig. 2.9(c). It can be seen that α increases approximately in a linear manner with the increasing of the beam height. With larger h and L, the achievable angle α can be enlarged. Then, rotational angles can be programmed by adjusting the number of layers and the geometry of the unit cells. Meanwhile, it should also be noted that a large α requires a large distance between the upper and bottom frame. Here, we observe that a large h will lead to contact between the upper and bottom frame when reaching the rotational state (see Appendix A.3). Therefore, when designing the structure with a large h, the contact issue should be considered.

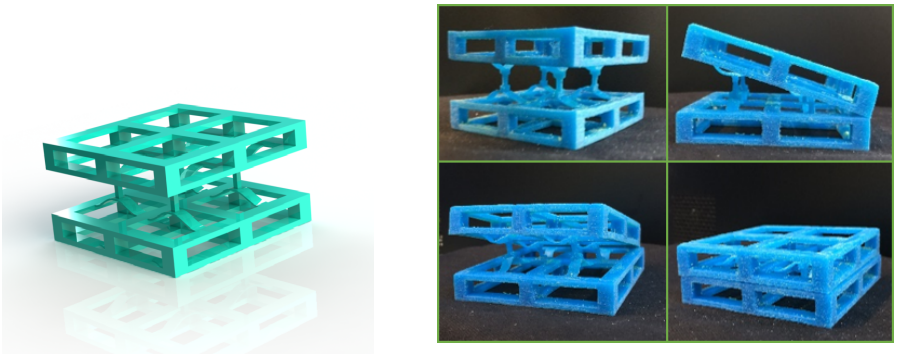

(a) (b)

Figure 2.10: 3D multi-stable metastructures with rotational states. (a) The metastructure is designed by arranging unit cells in an orthogonal pattern. (b) The fabricated prototype of the 3D metastructure. The structure is able to exhibit rotations along two directions, which result in four rotational stable states.

In addition, we demonstrate the rotations of a 3D multi-stable metastructure. This metastructure is shown in Fig. 2.10(a), and is designed with two units placed in an orthogonal pattern. It is fabricated using a poly-jet based multi-material printer (Objet350 Connex 3). From Fig. 2.10(b), it can be seen that this 3D metastructure is able to realize rotations along two directions, which is an extension of 2D structures. The rotational states in Fig. 2.10(b) can be seen as the deformations of two rows of 2D unit cells arranged in parallel. Therefore, it can be expected that the magnitude of this 3D structure's rotational force-displacement response, including force thresholds and stiffness, should be two times as large as a single 2D unit cell with the same length scales. This 3D structure

can be further extended to design bending actuators by stacking more unit cells. Overall, the design of 3D structure here paves the way for forming 3D deployable structures by patterning structures in x, y, z directions.

2.6. CONCLUSIONS

In this chapter, the rotational stable states of multi-stable beam-type metastructures have been presented, apart from the expected translational states. Both translational and rotational transitions exhibit negative stiffness (snap-through) behavior while the rotational transition exhibits more evident asymmetric characteristics as compared to the counterpart of translations. The parameters, including the beam height (h), thickness (t) and span (L), have been found paramount for rotational stability. Moreover, the criterion for reaching rotational states is established through a theoretical investigation. The proposed model, validated by finite element simulations, effectively predicts the rotational snap-through transitions in the negative stiffness interval and captures thresholds of h/L and t/L. It is shown that for realizing rotational states, h/L should be larger than critical values while t/L needs to be small, and t/L is more influential than h/L for tuning the maximum force of rotational transitions. This criterion serves as a guideline to tailor rotational snap-though behavior such as controlling force thresholds. Finally, we demonstrate the large rotations of metastructures with fabricated two- and three-dimensional metastructures, where the rotational stable states can be programmed by serially assembling units along multiple directions. With the proper units arrangement and design, the proposed multi-stable metastructures with rotational states can open up new opportunities for designing adaptive structures.

REFERENCES

[1] X. Zheng, H. Lee, T. H. Weisgraber, M. Shusteff, J. DeOtte, E. B. Duoss, J. D. Kuntz, M. M. Biener, Q. Ge, J. A. Jackson, *et al., Ultralight, ultrastiff mechanical metamaterials,* Science **344**, 1373 (2014).

[2] T. A. Schaedler, A. J. Jacobsen, A. Torrents, A. E. Sorensen, J. Lian, J. R. Greer, L. Valdevit, and W. B. Carter, *Ultralight metallic microlattices,* Science **334**, 962 (2011).

[3] L. R. Meza, S. Das, and J. R. Greer, *Strong, lightweight, and recoverable three-dimensional ceramic nanolattices,* Science **345**, 1322 (2014).

[4] T. A. Schaedler and W. B. Carter, *Architected cellular materials,* Annual Review of Materials Research **46**, 187 (2016).

[5] J. Bauer, L. R. Meza, T. A. Schaedler, R. Schwaiger, X. Zheng, and L. Valdevit, *Nanolattices: an emerging class of mechanical metamaterials,* Advanced Materials **29**, 1701850 (2017).

[6] X. Ren, R. Das, P. Tran, T. D. Ngo, and Y. M. Xie, *Auxetic metamaterials and structures: A review,* Smart materials and structures **27**, 023001 (2018).

[7] H. Wang, Y. Zhang, W. Lin, and Q.-H. Qin, *A novel two-dimensional mechanical metamaterial with negative poisson's ratio,* Computational Materials Science **171**, 109232 (2020).

[8] R. S. Lakes, *Negative-poisson's-ratio materials: auxetic solids,* Annual review of materials research **47**, 63 (2017).

[9] K. Takenaka, *Negative thermal expansion materials: technological key for control of thermal expansion,* Science and Technology of Advanced Materials **13**, 013001 (2012).

[10] Q. Wang, J. A. Jackson, Q. Ge, J. B. Hopkins, C. M. Spadaccini, and N. X. Fang, *Lightweight mechanical metamaterials with tunable negative thermal expansion,* Physical review letters **117**, 175901 (2016).

[11] L. Ai and X.-L. Gao, *Three-dimensional metamaterials with a negative poisson's ratio and a non-positive coefficient of thermal expansion,* International Journal of Mechanical Sciences **135**, 101 (2018).

[12] H. Zhu, T. Fan, Q. Peng, and D. Zhang, *Giant thermal expansion in 2d and 3d cellular materials,* Advanced Materials **30**, 1705048 (2018).

[13] F. Bobbert, S. Janbaz, T. van Manen, Y. Li, and A. Zadpoor, *Russian doll deployable meta-implants: Fusion of kirigami, origami, and multi-stability,* Materials & Design , 108624 (2020).

[14] J. Choi and R. Lakes, *Analysis of elastic modulus of conventional foams and of re-entrant foam materials with a negative poisson's ratio,* International Journal of Mechanical Sciences **37**, 51 (1995).

[15] A. A. Zadpoor, *Meta-biomaterials,* Biomaterials Science **8**, 18 (2020).

[16] F. Bobbert, S. Janbaz, and A. Zadpoor, *Towards deployable meta-implants,* Journal of Materials Chemistry B **6**, 3449 (2018).

[17] M. Schaffner, J. A. Faber, L. Pianegonda, P. A. Rühs, F. Coulter, and A. R. Studart, *3d printing of robotic soft actuators with programmable bioinspired architectures,* Nature communications **9**, 878 (2018).

[18] B. Gorissen, D. Melancon, N. Vasios, M. Torbati, and K. Bertoldi, *Inflatable soft jumper inspired by shell snapping,* Science Robotics **5** (2020).

[19] X. Zhao, G. Duan, A. Li, C. Chen, and X. Zhang, *Integrating microsystems with metamaterials towards metadevices,* Microsystems & nanoengineering **5**, 1 (2019).

[20] N. Hu and R. Burgueño, *Buckling-induced smart applications: recent advances and trends,* Smart Materials and Structures **24**, 063001 (2015).

[21] K. Bertoldi, V. Vitelli, J. Christensen, and M. van Hecke, *Flexible mechanical metamaterials,* Nature Reviews Materials **2**, 17066 (2017).

[22] G. Oliveri and J. T. Overvelde, *Inverse design of mechanical metamaterials that undergo buckling,* Advanced Functional Materials **30**, 1909033 (2020).

[23] Y. Kim, H. Yuk, R. Zhao, S. A. Chester, and X. Zhao, *Printing ferromagnetic domains for untethered fast-transforming soft materials,* Nature **558**, 274 (2018).

[24] S. Janbaz, F. Bobbert, M. Mirzaali, and A. Zadpoor, *Ultra-programmable buckling-driven soft cellular mechanisms,* Materials Horizons **6**, 1138 (2019).

[25] D. M. Correa, T. Klatt, S. Cortes, M. Haberman, D. Kovar, and C. Seepersad, *Negative stiffness honeycombs for recoverable shock isolation,* Rapid Prototyping Journal **21**, 193 (2015).

[26] F. Pan, Y. Li, Z. Li, J. Yang, B. Liu, and Y. Chen, *3d pixel mechanical metamaterials,* Advanced Materials **31**, 1900548 (2019).

[27] K. Bertoldi, *Harnessing instabilities to design tunable architected cellular materials,* Annual Review of Materials Research **47**, 51 (2017).

[28] D. Yang, B. Mosadegh, A. Ainla, B. Lee, F. Khashai, Z. Suo, K. Bertoldi, and G. M. Whitesides, *Buckling of elastomeric beams enables actuation of soft machines,* Advanced Materials **27**, 6323 (2015).

[29] A. Rafsanjani, K. Bertoldi, and A. R. Studart, *Programming soft robots with flexible mechanical metamaterials,* Science Robotics **4** (2019).

[30] G. Simitses and D. H. Hodges, *Fundamentals of structural stability* (Butterworth-Heinemann, 2006).

[31] H. Yang and L. Ma, *Multi-stable mechanical metamaterials with shape-reconfiguration and zero poisson's ratio,* Materials & Design **152**, 181 (2018).

[32] K. Che, C. Yuan, H. J. Qi, and J. Meaud, *Viscoelastic multistable architected materials with temperature-dependent snapping sequence,* Soft matter **14**, 2492 (2018).

[33] X. Tan, S. Chen, S. Zhu, B. Wang, P. Xu, K. Yao, and Y. Sun, *Reusable metamaterial via inelastic instability for energy absorption,* International Journal of Mechanical Sciences **155**, 509 (2019).

[34] J. Hua, H. Lei, Z. Zhang, C. Gao, and D. Fang, *Multistable cylindrical mechanical metastructures: Theoretical and experimental studies,* Journal of Applied Mechanics , 1 (2019).

[35] K. Che, C. Yuan, J. Wu, H. J. Qi, and J. Meaud, *Three-dimensional-printed multistable mechanical metamaterials with a deterministic deformation sequence,* Journal of Applied Mechanics **84**, 011004 (2017).

[36] H. Yang and L. Ma, *1d to 3d multi-stable architected materials with zero poisson's ratio and controllable thermal expansion,* Materials & Design **188**, 108430 (2020).

[37] J. Meaud and K. Che, *Tuning elastic wave propagation in multistable architected materials,* International Journal of Solids and Structures **122**, 69 (2017).

[38] L. Wu, X. Xi, B. Li, and J. Zhou, *Multi-stable mechanical structural materials,* Advanced Engineering Materials **20**, 1700599 (2018).

[39] S. Sun, N. An, G. Wang, M. Li, and J. Zhou, *Snap-back induced hysteresis in an elastic mechanical metamaterial under tension,* Applied Physics Letters **115**, 091901 (2019).

[40] C. S. Ha, R. S. Lakes, and M. E. Plesha, *Design, fabrication, and analysis of lattice exhibiting energy absorption via snap-through behavior,* Materials & Design **141**, 426 (2018).

[41] X. Tan, B. Wang, S. Chen, S. Zhu, and Y. Sun, *A novel cylindrical negative stiffness structure for shock isolation,* Composite Structures **214**, 397 (2019).

[42] T. Frenzel, C. Findeisen, M. Kadic, P. Gumbsch, and M. Wegener, *Tailored buckling microlattices as reusable light-weight shock absorbers,* Advanced Materials **28**, 5865 (2016).

[43] D. Restrepo, N. D. Mankame, and P. D. Zavattieri, *Phase transforming cellular materials,* Extreme Mechanics Letters **4**, 52 (2015).

[44] S. Shan, S. H. Kang, J. R. Raney, P. Wang, L. Fang, F. Candido, J. A. Lewis, and K. Bertoldi, *Multistable architected materials for trapping elastic strain energy,* Advanced Materials **27**, 4296 (2015).

[45] T. Chen, O. R. Bilal, K. Shea, and C. Daraio, *Harnessing bistability for directional propulsion of soft, untethered robots,* Proceedings of the National Academy of Sciences **115**, 5698 (2018).

[46] T. Chen, J. Mueller, and K. Shea, *Integrated design and simulation of tunable, multi-state structures fabricated monolithically with multi-material 3d printing,* Scientific reports **7**, 45671 (2017).

[47] M. Santer and S. Pellegrino, *Concept and design of a multistable plate structure,* Journal of Mechanical Design **133**, 081001 (2011).

[48] M. E. Pontecorvo, S. Barbarino, G. J. Murray, and F. S. Gandhi, *Bistable arches for morphing applications,* Journal of Intelligent Material Systems and Structures **24**, 274 (2013).

[49] C. Ren, Q. Li, and D. Yang, *Quasi-static and sound insulation performance of a multifunctional cylindrical cellular shell with bidirectional negative-stiffness metamaterial cores,* International Journal of Mechanical Sciences , 105662 (2020).

[50] X. Liu, F. Lamarque, E. Doré, and P. Pouille, *Multistable wireless micro-actuator based on antagonistic pre-shaped double beams,* Smart Materials and Structures **24**, 075028 (2015).

[51] K. Che, M. Rouleau, and J. Meaud, *Temperature-tunable time-dependent snapping of viscoelastic metastructures with snap-through instabilities,* Extreme Mechanics Letters **32**, 100528 (2019).

[52] H. Yang and L. Ma, *Multi-stable mechanical metamaterials by elastic buckling instability,* Journal of Materials Science **54**, 3509 (2019).

[53] M. Vangbo and Y. Bäcklund, *A lateral symmetrically bistable buckled beam,* Journal of Micromechanics and Microengineering **8**, 29 (1998).

[54] R. Marlow, *A general first-invariant hyperelastic constitutive model,* Constitutive Models for Rubber , 157 (2003).

[55] M. Alturki and R. Burgueño, *Multistable cosine-curved dome system for elastic energy dissipation,* Journal of Applied Mechanics **86**, 091002 (2019).

[56] J. Qiu, J. H. Lang, and A. H. Slocum, *A curved-beam bistable mechanism,* Journal of microelectromechanical systems **13**, 137 (2004).

[57] J. Cleary and H.-J. Su, *Modeling and experimental validation of actuating a bistable buckled beam via moment input,* Journal of Applied Mechanics **82**, 051005 (2015).

[58] B. Camescasse, A. Fernandes, and J. Pouget, *Bistable buckled beam: Elastica modeling and analysis of static actuation,* International Journal of Solids and Structures **50**, 2881 (2013).

[59] S. P. Timoshenko and J. M. Gere, *Theory of elastic stability* (Courier Corporation, 2009).

3

3D MULTI-STABLE METASTRUCTURES WITH ROTATIONAL AND TRANSLATIONAL STATES

In Chapter 2, the criteria for realizing rotational states have been defined to design planar structures with rotational degrees of freedom. In this chapter, we extend the concept of rotational states into three-dimensional (3D) structural designs such that a type of 3D multi-stable metastructures exhibiting both rotational and translational stable configurations is proposed based on 2D and 3D arrangements of bi-stable elements. The resulting level and tilted configurations are enabled by the rotational compliance, bi-stability and spatial arrangement of unit cells. The bi-stability of the unit cells and multi-stability of the metastructures are demonstrated and characterized by experiments and finite element analysis. Results show that transitions between level stable configurations are symmetric in terms of load-deflection response while switching to the tilted stable configurations leads to asymmetric mechanical responses. The tilted stable configurations are less stable than the level configurations. Moreover, we demonstrate that the level and tilted stable configurations of the metastructure depend on the parallel and serial arrangement of the unit cells.

This chapter is based on a journal paper: Zhang, Y., Wang, Q., Tichem, M. and van Keulen, F., (2019). Design and characterization of multi-stable mechanical metastructures with level and tilted stable configurations. Extreme Mechanics Letters, 34, p.100593.

3.1. INTRODUCTION

Mechanical metamaterials are rationally designed structured materials whose macroscopic properties are mainly determined by their structures rather than composition [1, 2]. This allows to realize unusual and novel properties for metamaterials. For example, mechanism-based auxetic metamaterials have been designed to obtain deployable structures [3, 4]. Phononic metamaterials have been developed to control and prohibit elastic waves in specific frequency ranges [5–7]. Other unconventional properties include ultra-lightweight but high stiffness [8], negative compressibility transitions [9] and high energy absorption [10].

In order to tune the properties of metamaterials after fabrication, metamaterials composed of multi-stable metastructures have been proposed and actively explored in recent years [11]. Multi-stable structures have multiple stable morphologies and are able to achieve significant geometrical changes by switching between different stable configurations. More importantly, these stable configurations do not require external loads to be maintained. The multi-stability has mainly been utilized in design of shape-changing structures and energy absorbers with tunable stiffness [12–15].

Many studies have demonstrated the design of multi-stable metastructures based on bi-stable elements exhibiting snap-through behavior. These designed structures are normally referred to as snap-through induced multi-stable structures (SIMS) [16–19]. Within the elastic regime, snap-through is a type of instability that causes a structure to jump from one stable configuration to the other when external loads beyond critical values are applied [20]. Thus, two stable configurations can be accommodated [21, 22]. The principle of snap-through based bi-stability can be applied to design smart metastructures over a wide range of length scales [11]. By combining bi-stable elements, multi-stability can be realized for metastructures [23–29]. For instance, Restrepo *et al.* [24] developed metastructures consisting of an array of bi-stable camber beams which can absorb energy under cyclic loading. Shan *et al.* [25] proposed a multi-stable structure using inclined straight beams for trapping elastic energy. Santer *et al.* [30] presented a multi-stable mechanism to morph surfaces. Since all the unit cells within the SIMS are identical, the deformation sequence is unpredictable when the structure is uniformly loaded. Che *et al.* [26] introduced geometry and material variations to acquire programmable behavior. Moreover, this snap-through behavior can also be triggered under tensile loading besides compressive loads [31].

Most studies on multi-stable metastructures are limited to translational state changes and only level stable configurations are explored due to the constraint of unit cells' rotational compliance. In previous chapter, by exploiting the rotational compliance, the hidden rotational degrees of freedom for two-dimensional (2D) metastructures have been presented for the first time, but relevance to applications normally requires designs to be highly effective in general three-dimensional (3D) settings. Therefore, we extend the previous methodology into a 3D structural design, and thus demonstrate a new type of 3D multi-stable metastructure allowing for both level and tilted stable configurations.

In this chapter, 3D bi-stable unit cells with snap-through behavior and rotational compliance are designed first. By a specific assembly of a number of unit cells, the resulting multi-stable metastructure is able to exhibit both translational and rotational macroscopic degrees of freedom (DOFs). That is, the resulting structures possess multi-

ple equilibrium states, including level and tilted stable configurations. These additional tilted stable configurations offer more design freedom for motion-related applications. Moreover, various tilted stable configurations can be obtained by combining the unit cells in different arrangements, which makes it possible to control the multi-stable property of metamaterials.

This chapter is organized as follows. Section 3.2 describes the geometry of the proposed unit cells and resulting multi-stable metastructures. The main features of the unit cells are highlighted and the associated level and tilted stable configurations are demonstrated. Section 3.3 describes experimental and numerical methods adopted in this work. The snap-through behavior of the proposed unit cells and the multi-stable metastructures are characterized in Section 3.4. In Section 3.5, the influence of unit cell arrangements on the resulting multi-stable behavior is studied. Moreover, the rotational states enabled by square units are demonstrated in Section 3.6.

3.2. STRUCTURE DESIGN

Here, we are targeting multi-stable metastructures, where bi-stable elements are used as basic unit cells. As shown in Fig. 3.1(a), a single bi-stable element allows for translational motion by switching among two stable configurations. It is illustrated in Fig. 3.1(b) that, the 1D arrangement of these elements forms a metastructure with two level stable configurations (LSCs) due to the translational motion. The corresponding metastructure may exhibit a relatively large stroke via transition between LSCs. If, in addition, the bi-stable unit cell provides rotational compliance, then it may be possible for the metastructure to exhibit additional tilted stable configurations (TSCs) next to the intrinsic LSCs (see Fig. 3.1(b)).

After combining the proposed unit cells into a metastructure, it can be observed in Fig. 3.2(a) that four stable configurations can be achieved for a metastructure composed of two unit cells: level (Configuration 1 and 4) and tilted stable configurations (Configuration 2 and 3). When unloaded, the metastructure can maintain its deformed shape in either level or tilted state. Different stable configurations can be realized by applying different loading conditions. For example, when the demonstrated metastructure is loaded in a LSC symmetrically, it responds with a translational transition to switch between two LSCs (Configuration 1 or 4). However, when an asymmetric load is applied, it transforms to a tilted stable configuration (Configuration 2 or 3).

According to the findings in Chapter 2, the rotational compliance and bi-stable behavior are essential for building 3D rotational metastructures. Therefore, a 3D unit cell with these two properties was proposed and studied, as depicted in Fig. 3.1(c). Specifically, a leaf spring with six strips (six-strip structure) was prestressed into a 3D curved shape by using two smaller frames. When this unit cell (Configuration 1) is mechanically deformed, the curved six-strip structure reconfigures into the other level stable configuration (Configuration 2), which results in a translation motion, see Fig. 3.1(c). Meanwhile, the rotational compliance ensures that the unit cell can achieve angular deformation, as shown in Fig. 3.1(d).

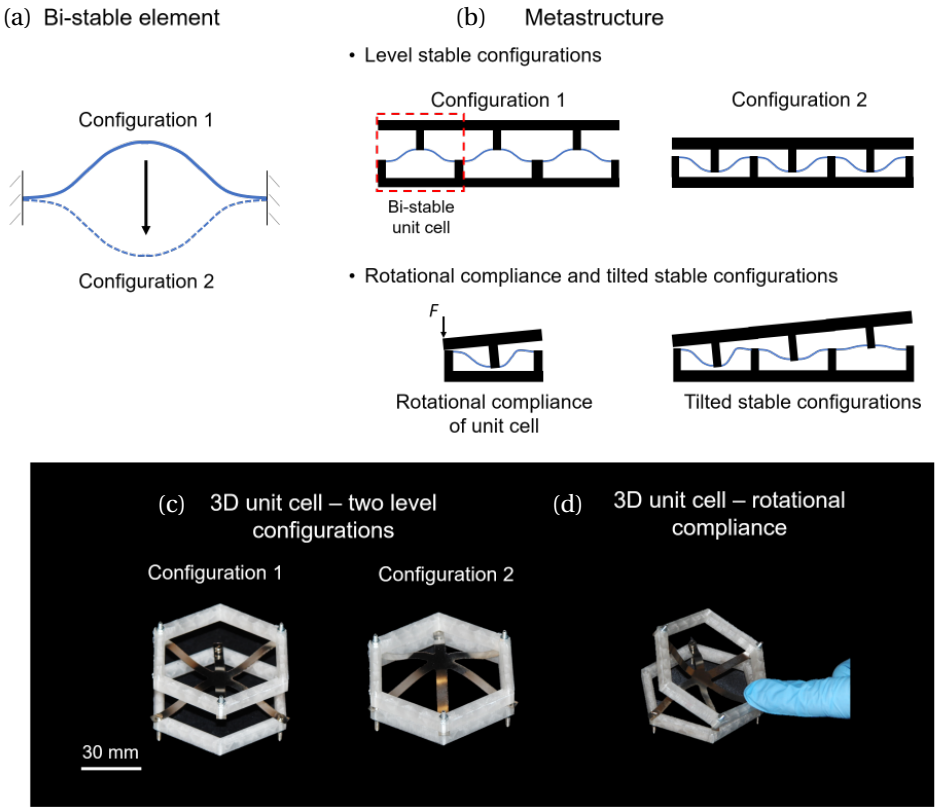

Figure 3.1: Design of 3D bi-stable unit cells. (a) A schematic of bi-stable behavior. (b) Schematics of a multi-stable metastructure exhibiting level stable configurations and rotational compliance. (c) The proposed 3D bi-stable unit cell with two level stable configurations. (d) Rotational compliance of the unit cell.

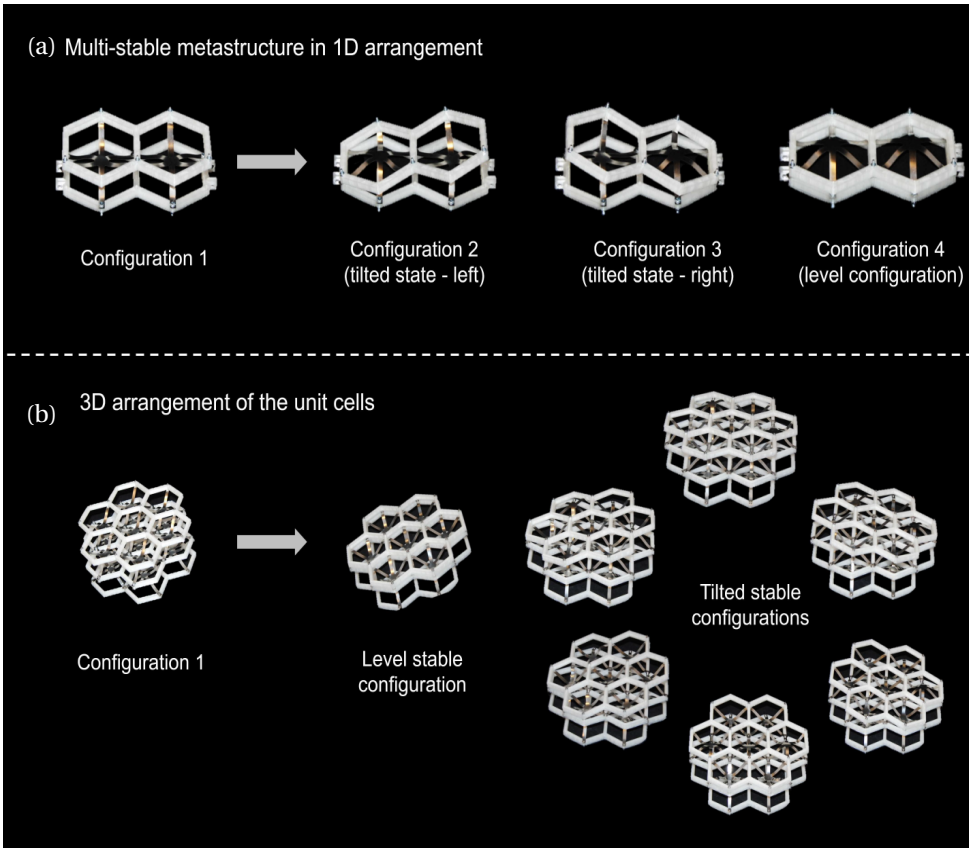

Figure 3.2: The proposed metastructures showing both level and tilted stable configurations. (a) A multi-stable metastructure consisting of two cells is obtained by 1D arrangement. Four stable states are found including LSCs and TSCs. (b) A 3D arrangement of unit cells resulting in multiple TSCs and LSCs.

Based on the proposed unit cells, it is possible to obtain different arrangements by repeating the unit cells. By a 3D arrangement of the unit cells, the resulting metastructure may have multiple TSCs along different directions. As an example, each layer of the arranged metastructure shown in Fig. 3.2(b) is able to exhibit six TSCs with different tilting orientations and two LSCs along the vertical direction (see Video). It should be noted that which particular level and tilted stable configurations can be realized depend on: *i*) the nonlinear properties of the unit cells, in particular their bi-stable behavior and rotational compliance; *ii*) the spatial arrangement of the unit cells. In order to identify the influence of arrangement on multi-stability, the mechanical responses of metastructures with different arrangements are experimentally determined, as discussed in Section 3.5.

3.3. METHODS

3.3.1. FABRICATION

Samples were manufactured following the procedure as illustrated in Fig. 3.3(a)–(d). The bi-stable unit cell is composed of three components, namely two frames and the six-strip structure. The flat six-strip structures were fabricated by laser-cutting 0.1 mm thick spring steel sheets (Alloy 1.4310, Jeveka, The Netherlands). The frames were printed from polylactic acid (PLA) using a fused deposition modeling printer (Prusa i3 MK2) and have been considered rigid in the numerical simulations. By connecting the frames with smaller in-plane dimensions, the six-strip structure was buckled into a curved configuration and the unit cell was assembled using screws as fasteners. The metastructures were obtained by connecting unit cells in different directions. Figure 3.3(d) illustrates an example of a 1D combination of unit cells for a multi-stable metastructure. Parameters of samples of this study are listed in the following Table 3.1.

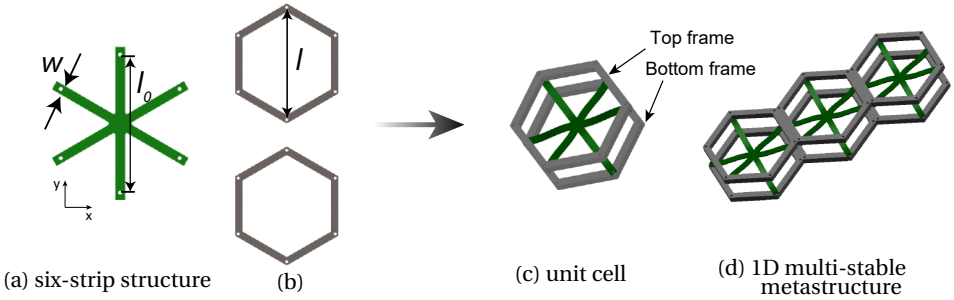

Figure 3.3: Schematics for fabrication of the presented unit cells and metastructures. (a) The flat six-strip element with an out-of-plane thickness t_e and its in-plane geometric parameters. (b) 3D printed frames with an out-of-plane thickness t_f and in-plane dimensions. (c) Assemble the bi-stable unit cell by connecting the six-strip structure to the two frames. (d) An assembly of the unit cells to obtain a multi-stable metastructure.

Table 3.1 Geometric parameters of bi-stable unit cells

Parameters	w	l_0	l	t_e	t_f
Values (mm)	5	73	69	0.1	6

3.3.2. EXPERIMENTS AND SIMULATIONS

To characterize the snap-through transitions, we investigated the mechanical behavior of structures using a uniaxial testing machine (ZwickRoell Z005, Germany). Uniaxial compression and tensile tests were conducted on fabricated samples to capture their snap-through transitions. Connectors were printed and used to transfer loading forces during loading tests. Quasi-static conditions were applied using a displacement control at a loading rate of 10 mm/min. During the mechanical deformation of the structures, we quantified the snap-through transitions as force-deflection curves. All the tests and measurements shown in this chapter were repeated three times for each sample. For each design, three samples were fabricated and tested to get mean values.

Nonlinear finite element analysis (FEA) was performed using ABAQUS to investigate in detail the local deformation of the designed structures. Because the strips experience only small deformations, a linear elastic constitutive model was used in the FEA. Four-node shell elements with reduced integration (S4R) were employed for the thin six-strip structure with Young's modulus $E = 180$ GPa and Poisson's ratio $\nu = 0.29$, consistent with the material we used in experiments. Frames were meshed using eight-node linear brick, reduced integration solid elements (C3D8R). A relatively high Young's modulus was assigned to the frames to mimic their rigidity. Pre-stresses were introduced to the metastructure by thermal loads. Specifically, thermal expansion coefficients were assigned to the top and bottom frames. By applying a controlled temperature drop, the frames shrank and resulted in the desired initial configuration of the modelled metastructures. The detailed modelling procedure we followed can be found in the Appendix B.

3.4. MECHANICAL PROPERTIES OF TRANSITIONS INTO LSCS AND TSCS

In this section, the mechanical properties of the designed unit cell as well as the associated metastructures are presented. The bi-stability of the unit cells and multi-stability of the metastructures are quantified, respectively. The results of experimental characterization will be given and discussed along with the numerical analysis.

3.4.1. BI-STABILITY OF THE UNIT CELL

To measure the responses of the presented unit cell under uniaxial loads, we firstly compressed the unit cell to Configuration 2 (denoted as loading) and then pulled it back to Configuration 1 (denoted as unloading), as depicted in Fig. 3.4(a)–(b). Main mechanical characteristics can be observed in Fig. 3.4(b): *i*) The bi-stable deformation behavior is evident from the force-deflection curve. In the initial phase, the force gradually in-

creases along with the axial displacement until the maximum critical compression force (F_{max}) is reached, as plotted in Fig. 3.4(b). A further deformation triggers elastic instability (i.e. snapping), where the structure shows negative stiffness. During the snapping phase, the force initially reduces to zero, and then becomes negative (tension). When contact between top and bottom frames occurs at a certain displacement (represented as the vertical dashed line in Fig. 3.4(b)), the negative force is balanced by the contact force, leading to the Configuration 2. *ii*) Symmetric behavior is observed, meaning that F_{max} is almost equal to that of the maximum tensile force (referred to F_{min} in Fig. 3.4(b)). This is due to the fact that the pre-stress is introduced to the flat six-strip structure. Similar behavior is also observed in other pre-stressed bi-stable designs in literature [32, 33]. *iii*) The reverse unloading process (black curve) follows nearly the same path as the loading (red curve), which demonstrates that the hysteresis is negligible for these structures.

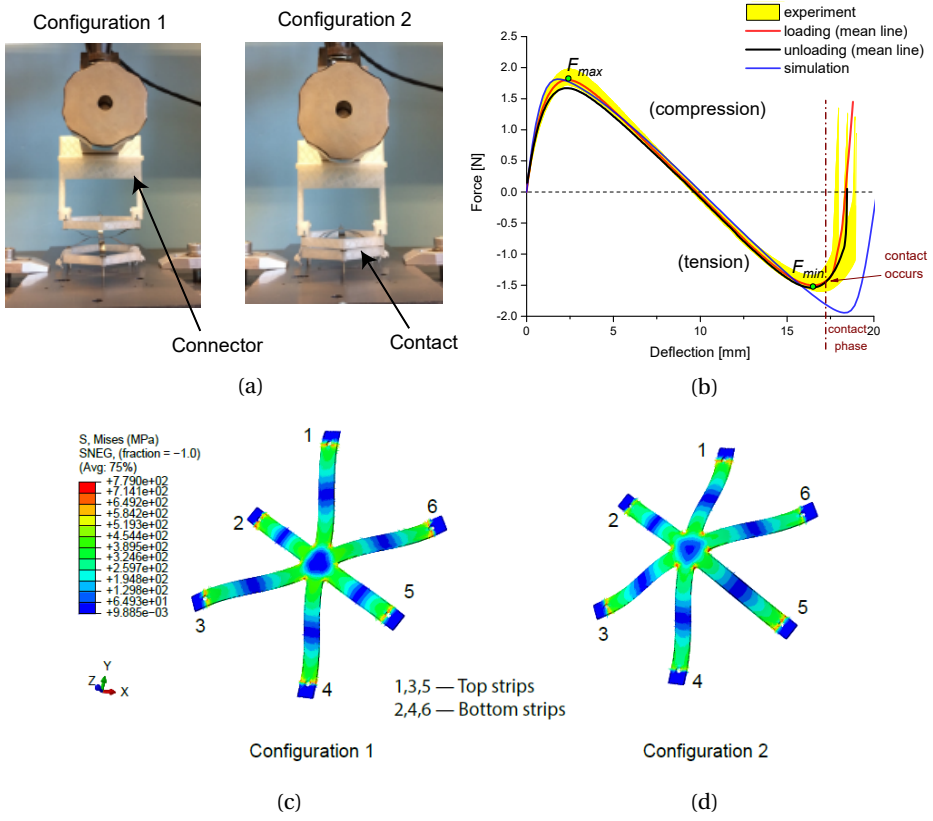

Figure 3.4: Snap-through behavior of the bi-stable unit cell. (a) The two stable configurations in experimental measurements. (b) Force-deflection curves for snap-through transitions between Configuration 1 and 2. The red and black curves represent the mean values of multiple experimental tests (yellow area) for loading and unloading, respectively. The dashed vertical line (contact) represents the situation that during loading, the top frame is in contact with the bottom frame. Blue curve denotes the snapping response obtained from FEA. (c)–(d) Contour plots for von Mises stress of the unit cell at Configuration 1 and 2, respectively.

In comparing numerical and experimental results, good agreement is observed before the contact occurs, as seen in Fig. 3.4(b). Since the frames are considered rigid, only the six-strip structure of the unit cell is modeled in FEA. It can be seen in Fig. 3.4(b) that the simulation reproduces the snapping response in experiments before the contact. The mismatch at the contact phase can be explained by the fact that the contact is not considered in simulations and thus, the six-strip structure is deformed further into the symmetric Configuration 2. In addition, the symmetric transition behavior is also demonstrated by the stress distributions in Fig. 3.4(c) and (d), where the two stable configurations correspond to the same level of strain energy.

3.4.2. MULTI-STABILITY OF THE METASTRUCTURE

The metastructures allowing for level and tilted configurations were characterized with representative samples which are 1D combination of two unit cells, as shown in Fig. 3.5(a). The loading response between LSCs is displayed in Fig. 3.5(b). It can be expected that compared to the snap-through of one unit cell, the critical force of this metastructure doubles while the maximal displacement remains unchanged. The characteristics of snapping transition are similar to the expected results, where the average F_{max} is around 2.8 N. In addition, integrating the force-deflection curve over the region of positive force and negative force (denoted as E_{in} and E_{out} in Fig. 3.5(b)), we find that E_{in} is almost equal to E_{out} as a result of the symmetric transition.

The transition to TSCs was realized by applying loads on one side of the top frame. As a result, the metastructure snaps from the initial to tilted configurations, as displayed in Fig. 3.6(a)–(b). Similarly, after the process of snapping and contact, the metastructure stabilizes at the TSC without external loads. This snapping behavior differs from the snapping behavior of the level configuration in two aspects: *i*) The critical compression force F_{max} (1 N in Fig. 3.6(b)) is smaller than that of LSCs (2.8 N in Fig. 3.5(b)). Therefore, less force/energy is required for the metastructure to switch into TSCs while the transition to LSCs requires larger actuation force. *ii*) The snapping response shown in Fig. 3.6(b) is not symmetric because curves in compression (positive) and tension (negative) loading are obviously different. The critical tension force F_{min} (-0.5 N) is lower as compared to F_{max} (1 N), indicating that the TSCs are less stable than the corresponding LSCs. This can also be explained from an energy perspective. It can observed that E_{out} in Fig. 3.6(b) is much smaller than E_{in}, implying that energy is trapped within the deformed stable TSCs. Therefore, when snapping to TSCs, the strips locally reconfigure to a higher energy, yet stable deformed state.

The corresponding numerical result agrees well with the experimental measurement, as plotted in Fig. 3.6(b). The stress evolution in Fig. 3.6(c)–(e) shows that the first cell experiences relatively larger deformation than the second cell. In particular, the three top strips (1,3,5) in the first cell snap into the other configuration during the initial loading stage. When this metastructure reaches the state as illustrated in Fig. 3.6(e), the Strip 3 already snapped to the other side. However, the Strip 1 and 5 have not been snapping fully. High stresses can be found in Strip 1 and 5, as shown in Fig. 3.6(e). The overall equilibrium of the tilted stable state can be interpreted as a combination of three force components: upward contact force from the bottom frame; downward pushing force applied by the first cell and upward pulling force generated in the second cell. A simplified

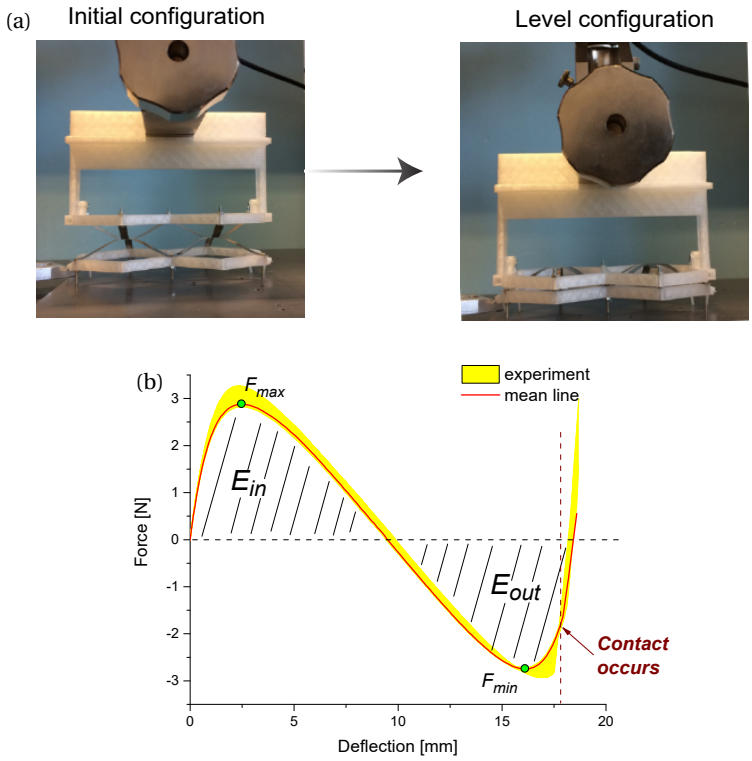

Figure 3.5: Characterization of snapping transitions from the initial configuration to the other level stable configuration for a metastructure composed of two bi-stable elements. (a) Two LSCs: initial and deformed level configurations. (b) Force-deflection curves corresponding to the snapping from the initial to level configuration. Red curve shows the mean values of multiple measurements.

analytical model for capturing the tilting transitions can be further developed based on the force equilibrium in future.

3.5. METASTRUCTURES WITH DIFFERENT ARRANGEMENTS

Here, two main arrangements of combining bi-stable mechanisms are studied and demonstrated: parallel in either one or two directions (1D and 2D), and serial arrangements. The serial arrangement represents the case of stacking bi-stable unit cells on top of each other, where the load is equally resisted by all unit cells but with different deformations for each. A parallel arrangement helps synthesizing new multi-stable characteristics from existing bi-stable units and it can be realized by in-plane patterning of the unit cells. Since the LSCs will be similar to the behavior discussed in previous section thus, from here on the main focus will be on the TSCs.

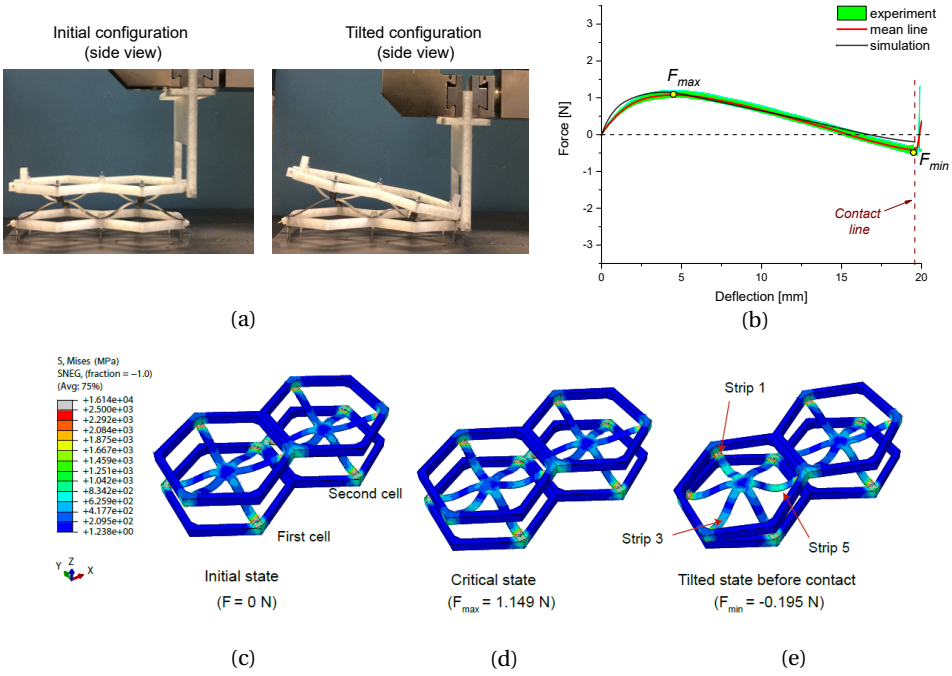

Figure 3.6: The tilting transitions of metastructures by experimental and numerical characterizations. (a) The initial configuration and the deformed tilted configuration. (b) Force-deflection diagrams for transitions from the initial to tilted configuration. Red line displays mean values of experimental results (green area); numerical result is plotted as black line. (c)–(e): FEA of snapping transitions: (c) represents the initial configuration of this metastructure. Then, the structure is loaded on the left side and (d) depicts the critical state where the maximum compression force F_{max} is reached. The stress distribution of the tilted state before the contact is shown in (e).

3.5.1. PARALLEL ARRANGEMENT: 1D

Metastructures with unit cells arranged in 1D are depicted in Fig. 3.7(a). Figure 3.7(b) depicts multiple force-deflection responses for switching from the initial configuration to different TSCs shown in Fig. 3.7(a). It is first found that these metastructures are able to exhibit TSCs, which is also demonstrated by experimental results shown in Fig. 3.7(b). Figure 3.7(c) presents the critical compression forces F_{max} and the resulting tilt angle θ (see Fig. 3.7(a)) at TSCs as a function of cell numbers. Non-proportional relations are reported as a result of the nonlinear behavior of the unit cells. With increasing the number of cells, the critical compression force increases while the tilt angle decreases.

3.5.2. PARALLEL ARRANGEMENT: 2D

The smallest 2D arrangement is composed of three unit cells, as seen in Fig. 3.8(a). Besides the stable initial and level configurations, multiple TSCs (i.e. tilting behavior along different directions) are realized for the metastructure. Furthermore, it is noted that the tilting axes depend on the in-plane symmetry of structure. As this structure has three axes of symmetry as shown in Fig. 3.8(a), we separate the TSCs into two categories: two-

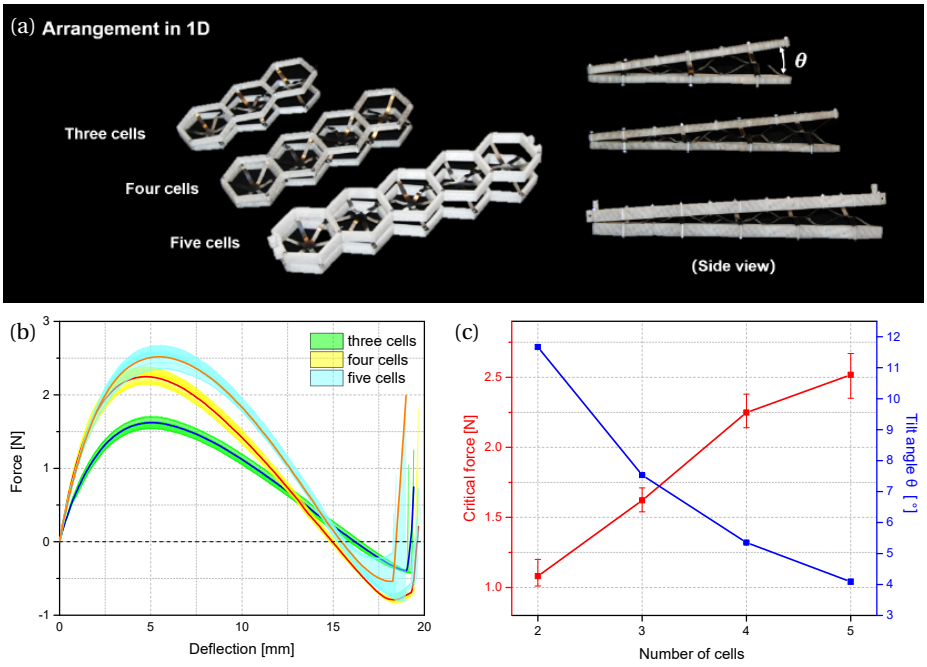

Figure 3.7: The 1D parallel arrangement of the unit cells. (a) Metastructures consisting of three, four and five unit cells. (b) The tilting response of these 1D metastructures: loading from the initial configuration into TSCs experimentally. The solid curves represent the mean values. (c) The maximal critical compression forces (F_{max}) and tilt angles (θ) as a function of the number of unit cells.

point tilting (Configuration 4,6,8) where there are two contact points at the TSCs and one-point tilting (Configuration 3,5,7) in which only one contact point is observed.

The characterization of snapping into LSCs and TSCs is displayed in Fig. 3.8(b) and (c), respectively. The snapping transition between LSCs shows a similar characteristic as the snap-through behavior of the unit cell. For the two-point tilting, the critical compression force is approximately two times larger than that of one-point tilting, as shown in Fig. 3.8(c). This can be explained by the fact that in case of two-point tilting two cells show snapping deflections whereas for one-point tilting, only the cell close to the loading point switches into the other stable configuration. The non-buckled unit cells mainly act as rotation points. The buckled unit cells essentially determine the snapping force of transitions. Moreover, the TSCs corresponding to the two-point tilting exhibit larger negative critical force (F_{min}) as compared to the one-point tilting, which implies that two-point TSCs are more stable than the one-point TSCs.

3.5.3. SERIAL ARRANGEMENT

As discussed, the in-plane parallel arrangements mainly affect the tilting behavior and resulting stable configurations. The influence of assembling unit cells in series is studied through a metastructure with two layers, as displayed in Fig. 3.9(a). Specifically, each

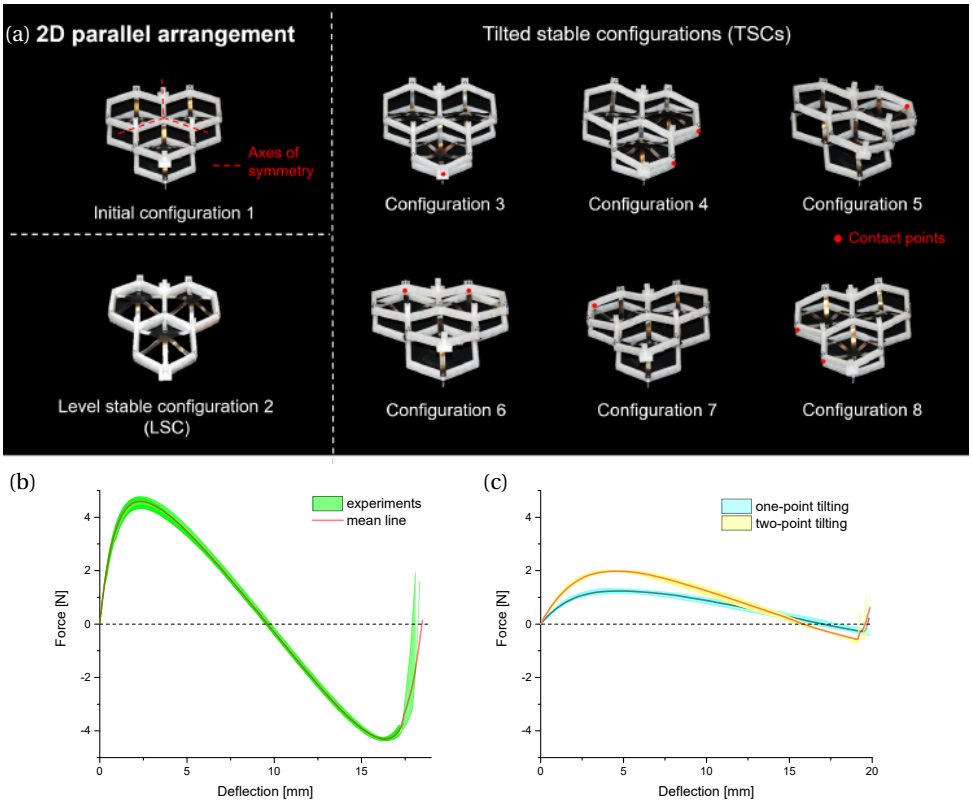

Figure 3.8: A 2D parallel arrangement of metastructure and its stable configurations. (a) The stable configurations include six TSCs and two LSCs. Two types of TSCs are found for the metastructure: two-point and one-point tilting. (b) The experimental force-deflection response of snapping between LSCs (from Configuration 1 to 2). (c) The force-deflection diagrams for two types of snapping transitions in experiments: one-point tilting (from Configuration 1 to 3, 5 or 7) and two-point tilting (from Configuration 1 to 4, 6 or 8).

layer exhibits four stable configurations and the demonstrated two-layer structure can realize sixteen stable configurations in total. In general, by stacking elements with x stable configurations, the resulting n layers metastructure can possess x^n stable configurations. Here, we choose four typical stable configurations realized by applying different loading conditions, as shown in Fig. 3.9(a): level and tilt tests. These two tests denote the snap-through transitions to the LSCs and TSCs, respectively. The results of tests are plotted in Fig. 3.9(b)–(c). Two sequential snap-through responses are captured in both tests. The amplitude of the second peak force is slightly larger than the first one, although they are designed to be the same. Discrepancies arise from manufacturing imperfections and assembling tolerances. The fluctuation of force-deflection curves in a particular region may be caused by the loading or structural imperfections.

For the proposed bi-stable unit cells, the basic behavior of arrangements can be summarized as follows: *i*) The 1D parallel arrangement results in two LSCs and TSCs with different tilting angles. *ii*) For 2D in-plane symmetric patterning of the unit cells, the

possible TSCs can be found based on the structural symmetry axes. *iii*) By serial arrangements, more LSCs and TSCs can be realized for the metastructure while each layer still exhibits multi-stable behavior independently. The presented multi-stable metastructures with various LSCs and TSCs can be further used as building blocks to construct multi-stable metamaterials. For instance, a multi-layer metamaterial can be formed as an assembly with both parallel and serial arrangements of the unit cell, as displayed in Fig. 3.2(b). Through controlling the layout of unit cells and the number of serial layers, the spatial positions and tilting angles of stable configurations can be tuned.

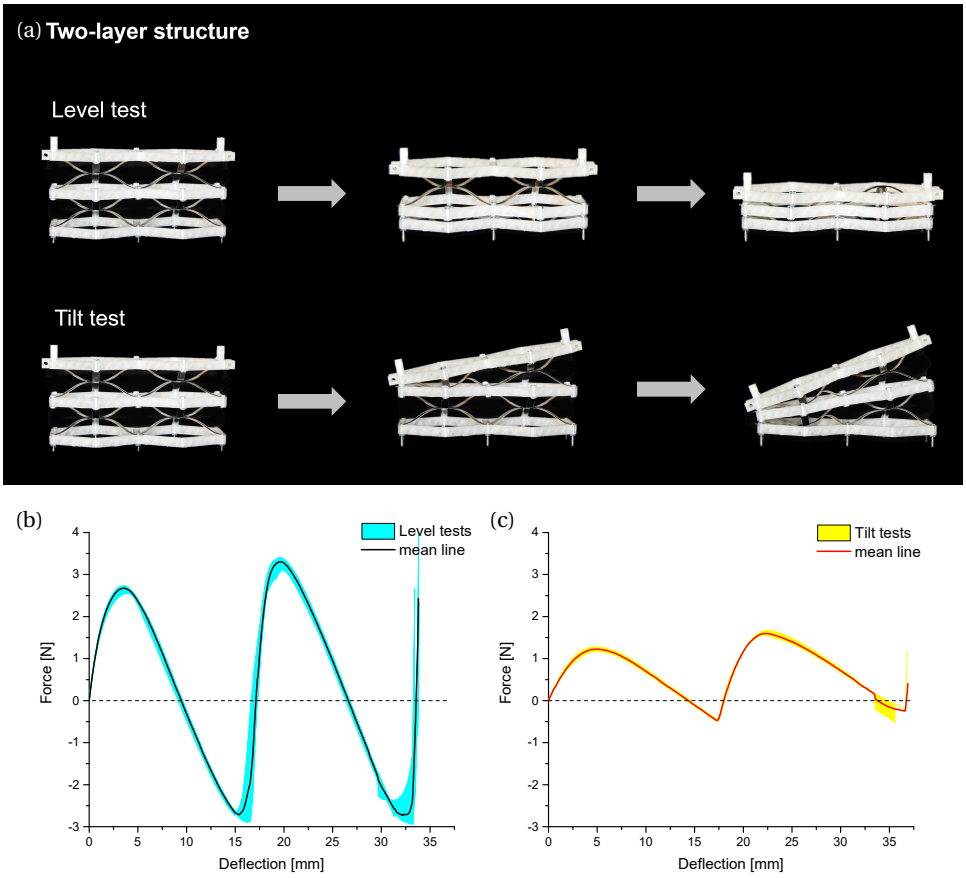

Figure 3.9: A two-layer metastructure obtained by serial arrangements of the unit cells. (a) Five out of sixteen stable configurations for the two-layer metastructure. Experimental tests were conducted via uniform loading (level tests) and loading on the left side (tilt tests). (b) The mechanical response of level tests, namely the snapping transitions to LSCs. (c) The mechanical response of tilting tests, namely the snapping transitions to TSCs.

3.6. METASTRUCTURES BASED ON SQUARE CELLS

Apart from hexagonal units, elements of square shapes, as another type of regular polygons, can also be adopted to construct periodic metastructures since they can fill up a plane without gaps or overlaps. In this section, associated multi-stable metastructures based on square-shape unit cells are designed as well to demonstrate the versatility of programming tilted stable states with different shapes. The resulting multi-stable metastructures are fabricated following the same procedure as the previous hexagonal structures.

Figure 3.10 presents the achievable stable configurations for square-shape multi-stable metastructures with 1D and 2D arrangements. Specifically, 1D arrangement of square units allows for both level and tilted stable states, while 2D arrangements result in four tilted stable configurations. The tilted configurations (1 and 2), denoted in Fig. 3.10(b), are symmetric with respect to the middle line of this structure. It can be anticipated that by combining more square units in 1D, the tilted configurations can still be retained, similar to hexagonal structures shown in Fig. 3.7(b). Moreover, for 2D arrangement demonstrated in Fig. 3.10(c), the four rotational snap-through transitions are supposed to exhibit the same characteristics even though imperfections introduced by manufacturing process may yield minor deviations on force-displacement responses. In addition, when compared with parallel hexagon patterns presented in Fig. 3.8(a), it can be concluded that the tilting behavior of such multi-stable mechanical metamaterials is determined by a comprehensive effect of shapes of unit cells and arrangements, such that parallel arrangement of hexagonal and square unit cells lead to distinct tilting directions. This further demonstrates that the rotational properties of multi-stable metastructures can be programmed and tuned by adopting different unit cells or arrangements.

3.7. CONCLUSIONS

In this work, we have proposed a new type of 3D bi-stable unit cell which allows the corresponding metastructures to exhibit both level and tilted stable configurations (LSCs and TSCs respectively). The pre-stress gives rise to the LSCs and the rotational compliance of the unit cell paves the way for the TSCs. The snapping responses of the unit cells and metastructures were studied both experimentally and numerically. Results show that the transition to LSCs exhibits symmetric behavior in terms of maximal critical compression and tension force, without energy trapping. For transitions to the TSCs, the load-deflection responses are asymmetric in such a way that the critical tension force is smaller than the maximal compression force, resulting in a deformed tilted stable state with higher strain energy. This indicates that TSCs are less stable when exposed to an external stimulus. Moreover, the metastructures are capable of exhibiting TSCs in multiple directions. Two main arrangements with different metastructures have been demonstrated and studied with hexagonal and square shape unit cells. It has been shown that the tilting directions of in-plane symmetric patterning are determined by the symmetry axes of the metastructures while a number of LSCs can be accomplished by serial arrangements. Based on these arrangements, metastructures with multiple LSCs and TSCs can be designed and used to build reconfigurable metamaterials.

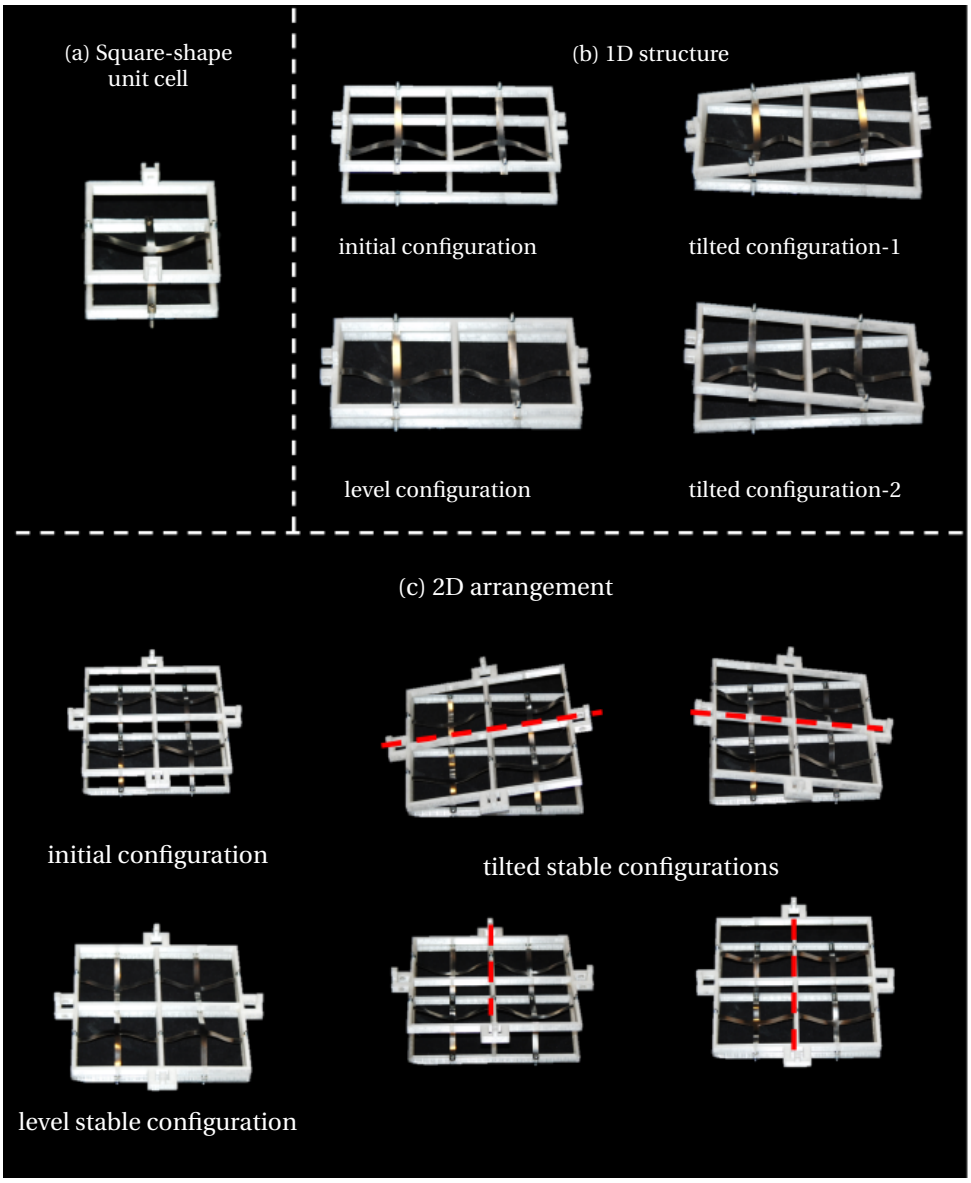

Figure 3.10: Level and tilted stable states of square-shape multi-stable metastructures. (a) A square-shape unit cell. (b) Similar to hexagonal elemets, 1D assembly of square unit cells enables both level and tilted stable states for metastructures. (c) 2D arrangement of square unit cells yields four tilted stable configurations, along two perpendicular directions that are denoted as red dashed lines in this figure.

REFERENCES

[1] T. A. Schaedler and W. B. Carter, *Architected cellular materials,* Annual Review of Materials Research **46**, 187 (2016).

[2] K. Bertoldi, V. Vitelli, J. Christensen, and M. van Hecke, *Flexible mechanical metamaterials,* Nature Reviews Materials **2**, 17066 (2017).

[3] X. Ren, R. Das, P. Tran, T. D. Ngo, and Y. M. Xie, *Auxetic metamaterials and structures: A review,* Smart Materials and Structures **27**, 023001 (2018).

[4] K. Bertoldi, P. M. Reis, S. Willshaw, and T. Mullin, *Negative poisson's ratio behavior induced by an elastic instability,* Advanced Materials **22**, 361 (2010).

[5] M. I. Hussein, M. J. Leamy, and M. Ruzzene, *Dynamics of phononic materials and structures: Historical origins, recent progress, and future outlook,* Applied Mechanics Reviews **66**, 040802 (2014).

[6] S. Babaee, N. Viard, P. Wang, N. X. Fang, and K. Bertoldi, *Harnessing deformation to switch on and off the propagation of sound,* Advanced Materials **28**, 1631 (2016).

[7] J. Meaud and K. Che, *Tuning elastic wave propagation in multistable architected materials,* International Journal of Solids and Structures **122**, 69 (2017).

[8] X. Zheng, H. Lee, T. H. Weisgraber, M. Shusteff, J. DeOtte, E. B. Duoss, J. D. Kuntz, M. M. Biener, Q. Ge, J. A. Jackson, *et al.*, *Ultralight, ultrastiff mechanical metamaterials,* Science **344**, 1373 (2014).

[9] Z. G. Nicolaou and A. E. Motter, *Mechanical metamaterials with negative compressibility transitions,* Nature materials **11**, 608 (2012).

[10] J.-H. Lee, L. Wang, S. Kooi, M. C. Boyce, and E. L. Thomas, *Enhanced energy dissipation in periodic epoxy nanoframes,* Nano letters **10**, 2592 (2010).

[11] K. Bertoldi, *Harnessing instabilities to design tunable architected cellular materials,* Annual Review of Materials Research **47**, 51 (2017).

[12] M. E. Pontecorvo, S. Barbarino, G. J. Murray, and F. S. Gandhi, *Bistable arches for morphing applications,* Journal of Intelligent Material Systems and Structures **24**, 274 (2013).

[13] D. M. Correa, C. C. Seepersad, and M. R. Haberman, *Mechanical design of negative stiffness honeycomb materials,* Integrating Materials and Manufacturing Innovation **4**, 10 (2015).

[14] N. Hu and R. Burgueño, *Buckling-induced smart applications: recent advances and trends,* Smart Materials and Structures **24**, 063001 (2015).

[15] C. G. Diaconu, P. M. Weaver, and F. Mattioni, *Concepts for morphing airfoil sections using bi-stable laminated composite structures,* Thin-Walled Structures **46**, 689 (2008).

[16] Y. S. Oh and S. Kota, *Synthesis of multistable equilibrium compliant mechanisms using combinations of bistable mechanisms,* Journal of Mechanical Design **131**, 021002 (2009).

[17] B. Haghpanah, L. Salari-Sharif, P. Pourrajab, J. Hopkins, and L. Valdevit, *Multistable shape-reconfigurable architected materials,* Advanced Materials **28**, 7915 (2016).

[18] C. Findeisen, J. Hohe, M. Kadic, and P. Gumbsch, *Characteristics of mechanical metamaterials based on buckling elements,* Journal of the Mechanics and Physics of Solids **102**, 151 (2017).

[19] K. Che, C. Yuan, H. J. Qi, and J. Meaud, *Viscoelastic multistable architected materials with temperature-dependent snapping sequence,* Soft matter **14**, 2492 (2018).

[20] G. Simitses and D. H. Hodges, *Fundamentals of structural stability* (Butterworth-Heinemann, 2006).

[21] Q. Chen, X. Zhang, and B. Zhu, *Design of buckling-induced mechanical metamaterials for energy absorption using topology optimization,* Structural and Multidisciplinary Optimization **58**, 1395 (2018).

[22] P. Cazottes, A. Fernandes, J. Pouget, and M. Hafez, *Bistable buckled beam: modeling of actuating force and experimental validations,* Journal of Mechanical Design **131**, 101001 (2009).

[23] T. Chen, J. Mueller, and K. Shea, *Integrated design and simulation of tunable, multi-state structures fabricated monolithically with multi-material 3d printing,* Scientific Reports **7**, 45671 (2017).

[24] D. Restrepo, N. D. Mankame, and P. D. Zavattieri, *Phase transforming cellular materials,* Extreme Mechanics Letters **4**, 52 (2015).

[25] S. Shan, S. H. Kang, J. R. Raney, P. Wang, L. Fang, F. Candido, J. A. Lewis, and K. Bertoldi, *Multistable architected materials for trapping elastic strain energy,* Advanced Materials **27**, 4296 (2015).

[26] K. Che, C. Yuan, J. Wu, H. J. Qi, and J. Meaud, *Three-dimensional-printed multistable mechanical metamaterials with a deterministic deformation sequence,* Journal of Applied Mechanics **84**, 011004 (2017).

[27] T. Frenzel, C. Findeisen, M. Kadic, P. Gumbsch, and M. Wegener, *Tailored buckling microlattices as reusable light-weight shock absorbers,* Advanced Materials **28**, 5865 (2016).

[28] X. Tan, B. Wang, S. Chen, S. Zhu, and Y. Sun, *A novel cylindrical negative stiffness structure for shock isolation,* Composite Structures **214**, 397 (2019).

[29] H. Yang and L. Ma, *Multi-stable mechanical metamaterials with shape-reconfiguration and zero poisson's ratio,* Materials & Design **152**, 181 (2018).

[30] M. Santer and S. Pellegrino, *Concept and design of a multistable plate structure,* Journal of Mechanical Design **133**, 081001 (2011).

[31] A. Rafsanjani, A. Akbarzadeh, and D. Pasini, *Snapping mechanical metamaterials under tension,* Advanced Materials **27**, 5931 (2015).

[32] B. Camescasse, A. Fernandes, and J. Pouget, *Bistable buckled beam: Elastica modeling and analysis of static actuation,* International Journal of Solids and Structures **50**, 2881 (2013).

[33] M. Vangbo, *An analytical analysis of a compressed bistable buckled beam,* Sensors and Actuators A: Physical **69**, 212 (1998).

4

MULTI-STABLE METASTRUCTURES FOR ENERGY ABSORPTION

Multi-stable metastructures composed of curved beams can switch to a series of stable configurations via elastic snap-through transitions. The elastic deformations allow metastructures to function as reusable energy absorbers. However, conventional metastructure designs based on solid beams often result in relatively low energy dissipation. In this chapter, it is found that by increasing the beam unit's bending stiffness while keeping the volume/mass constant, energy dissipation of the metastructure can be largely improved. Based on this observation, we propose two types of structural designs (lattice and hollow cross-section design) as building blocks for multi-stable metastructures. The lattice design is realized by incorporating lattice structures into pre-shaped beams while for the hollow cross-section design, a box-shaped cross section is adopted. The proposed structures are experimentally characterized under cyclic loading and are shown to exhibit sequential snap-through transitions with relatively large energy dissipation. Results show the snap-through behavior can be further tailored through tuning structural in-plane thickness. Effects of geometric parameters on snap-through, local buckling and bi-stability are investigated, and the feasible design domains for selecting proper lattice and cross-section geometries are identified. In addition, we demonstrate that the proposed design is not restricted to beams, and can be extended to shell structures.

This chapter is based on a journal paper: Y. Zhang, M. Tichem, F. van Keulen, (2021). A Novel Design of Multi-stable Metastructures for Energy Dissipation, Materials & Design, p.110234.

4.1. INTRODUCTION

Energy absorping materials play important roles in protecting delicate objects and mitigating impact in many fields, for example, automobiles, aircraft and civil engineering [1]. To realize energy absorption, a number of strategies have been proposed to dissipate energy during a crash, including lightweight honeycomb structures [2, 3], sandwich structures [4–6], and metallic foams [7, 8]. The energy dissipation of these structures is mostly associated with plastic deformations and thus it results in inevitable structural damage.

Recently, owing to its potential of achieving energy absorption with elastic deformations, the concept of designing mechanical metastructures with snap-through behavior has been proposed and extensively studied [9, 10]. Mechanical metastructures are rationally designed periodic structures that exhibit novel functionalities from their elementary structures rather than material properties. The snap-through property is a type of buckling behavior that causes a structure to "jump" from one configuration to the other when the applied load exceeds a critical value. To build metastructures exhibiting snap-through behavior, pre-shaped curved beams, as structural elements that exhibit snap-through behavior, have commonly been adopted [11, 12]. For metastructures composed of a number of curved beams, a sequential snap-through behavior and negative stiffness can be observed in the quasi-static load-deflection curves [13]. Moreover, these metastructures often exhibit a series of stable deformed configurations and are, thus, referred to as multi-stable beam-type metastructures (MBMs) [14, 15]. The multi-stability enables metastructures to retain their deformed configurations without the need for continuous external loading, facilitating motion- and energy-related functionalities [9]. For instance, it has been demonstrated that multi-stability can be utilized to design mechanical logic gates for Boolean computations [16]. With regard to energy absorption, the MBMs can realize an hysteresis loop under a quasi-static loading-unloading cycle, whereas energy is dissipated through a dynamic snap-through process [17–19]. Unlike structures which dissipate energy by means of plastic deformations, these metastructures undergo elastic deformations and the deformed structure can be fully reversed back to its initial configuration. As a result, these metastructures can be reused as shock absorbers multiple times. Moreover, the energy absorption is rate independent in the sense that when the external loading frequency is significantly lower than the metastructure's lowest eigenfrequency, the resulting hysteresis is hardly affected by the loading rate [20–22].

Many prototypes of MBMs have been demonstrated and studied in literature. Different geometries have been proposed, including planar [23–30], three-dimensional (3D) cylindrical [14, 31, 32], hexagonal [33, 34] and cubic geometries [35–37]. For instance, Restrepo *et al.* [24] and Zhang *et al.* [38] investigated energy dissipation of multi-stable metastructures comprising curved beams arranged in one (1D) and two directions (2D). Hua *et al.* [31] extended the planar beams to spatial curved beams for developing cylinder-shape metastructures. Ha *et al.* [35] combined six curved beams into a 3D unit cell and presented a metastructure design for realizing energy absorption in three directions. While these previous studies focused on multi-stable metastructures under compressive loads, Sun *et al.* [25] presented a type of multi-stable structure consisting of two non-identical elements, to achieve energy absorption under tension.

For multi-stable metastructures consisting of snapping units, their energy dissipation capability is closely connected with the unit cells' snap-through behavior [24, 39]. That is, snap-through units with stiffer mechanical responses will lead to an improvement of metastructures' energy dissipation. In the case of MBM, most previous studies have concentrated on using solid beam units to design metastructures. In this paper, we aim to develop new designs for MBMs to realize better energy dissipation than the solid beam designs. Specifically, it is found that by increasing the beam units' bending stiffness to a large extent, the corresponding metastructures can exhibit an improved energy dissipation. Based on this observation, we propose two types of snapping beams with enhanced bending stiffness as building blocks to construct metastructures. That is, for a planar design, lattice structures are introduced into the curved beam to obtain an hierarchical beam. Another strategy is to design hollow beams with box-shaped cross sections. Compared with previously studied solid beams, the proposed designs enable dissipation of more energy without using more material. Moreover, the proposed designs introduce additional design parameters, providing a larger design space to tune the snap-through features. In addition, this concept of increasing structural bending stiffness can be extended to shell structures.

The remainder of this paper is organized as follows. The working principle of the proposed design is firstly discussed in Section 4.2. The concept of lattice and cross-section designs is elaborated in Section 4.3, where the key geometric parameters are specified and categorized. Furthermore, the experimental and numerical approaches we used are discussed. Section 4.4 presents the mechanical properties of unit cells comprising hierarchical and hollow beams. The effect of geometric parameters on snap-through transition is explored. In Section 4.5, we investigate the deformation characteristics of multi-stable metastructures under cyclic loading. The energy dissipation is evaluated both experimentally and analytically. A quantitative comparison between the proposed and traditional designs is discussed. In Section 4.6, we demonstrate the potential of extending the proposed design to develop lattice-based shells. Conclusions are presented in Section 4.7.

4.2. DESIGN PRINCIPLE

The structural design in this work is based on the pre-shaped curved solid beam, as illustrated in Fig. 4.1(a). The beam's geometry can be described as:

$$y(x) = \frac{H}{2}(1 - \cos(2\pi \frac{x}{L})) \tag{4.1}$$

where H, L, T, B represent height, span, in-plane thickness and out-of-plane width of the beam, respectively. The effective bending and axial stiffness of the beam are denoted as EI/L^3 and EA/L, respectively. When a force (denoted as F) is applied at the center, as shown in Fig. 4.1(a), the beam can exhibit a snap-through transition and may reach the second stable state (curved dashed line). Here, the force-displacement ($F-d$) response of the beam is studied analytically. An approximate analytical model is adopted, based on the principle of mode superposition. It has been shown that the model can provide a good estimate of the snap-through transition [31, 40, 41]. Here, the first seven buckling modes are employed as a basis, and governing equations are derived on the basis of the

minimum total potential energy principle (see Appendix C.1).

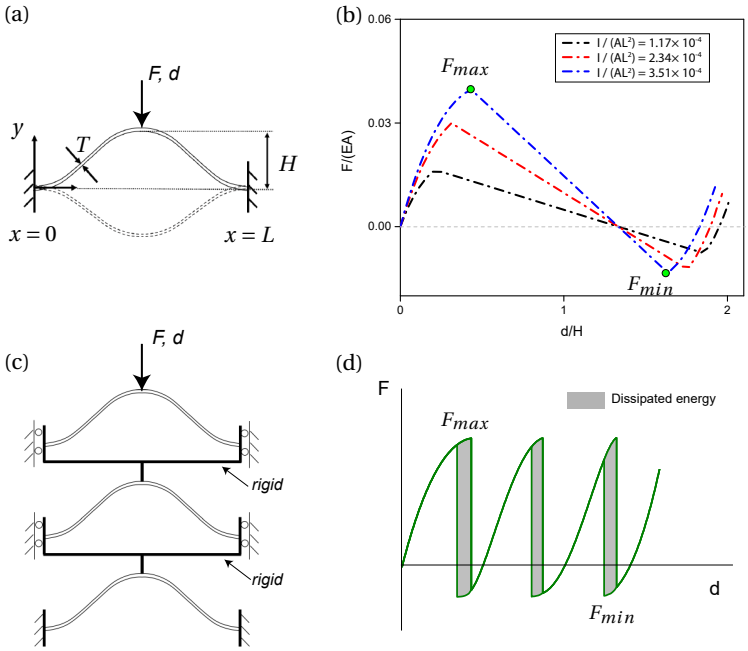

Figure 4.1: Pre-shaped solid beams and the effect of bending stiffness on snap-through behavior. (a) A pre-shaped solid beam. The out-of-plane dimension is denoted as B. (b) The force-displacement curves predicted by the analytical model are shown, where cross-sectional area is kept as a constant value ($A = 12$ mm^2). Snap-through responses of beams with different relative bending stiffness are presented. (c) A system composed of three pre-shaped beams arranged in series. (d) The force-displacement curve of the three-beam system under a displacement-controlled loading cycle is illustrated.

The resulting force-displacement curves obtained from the analytical analysis are shown in Fig. 4.1(b), where snap-through transitions of structures with different bending stiffness but the same cross-sectional area (A) are presented. During the displacement-controlled loading, two critical forces (denoted as F_{max} and F_{min}) are identified, and the structure exhibits a negative tangent stiffness after reaching F_{max}. It can be noted that when enlarging the structure's effective bending stiffness, both F_{max} and F_{min} increase, and the absolute value of the negative tangent stiffness increases as well. The effect of bending stiffness on the snap-through behavior indicates that when the axial stiffness of the structure is kept unchanged, increasing the bending stiffness can effectively result in a stiffer mechanical response.

Increasing the absolute values of F_{max} and F_{min} enables to enhance the energy dissipation. For a multi-stable metastructure consisting of serially arranged curved beams, an hysteresis can be realized under a displacement-controlled loading-unloading cycle [20, 24]. Fig. 4.1(c) shows a three-beam system for which the displacement at the top is prescribed. Due to unavoidable imperfections in practice, the element with the smallest F_{max} becomes unstable first and will snap. As a result, a dynamic process is initiated, leading to dissipation of energy. This dissipated energy is converted to heat in

turn. The other two beam units initially follow the stable unloading equilibrium without energy dissipation. Consequently, the corresponding force-displacement curve shows three "jumps" (see Fig. 4.1(d)). Similarly, for the unloading path, jumps will happen upon reaching F_{min}, resulting in the unstable transition of one element. After a loading-unloading cycle, an hysteresis loop, representing the energy dissipation of the metastructure, can be identified. It can be noted that the resulting hysteresis loop is closely associated with the beam unit's snap-through behavior. For the same amount of material, when adopting structural units with enhanced bending stiffness, it can be expected that better energy dissipation can be realized.

4.3. STRUCTURE DESIGN AND METHODS

Following the concept of enlarging the relative bending stiffness, we present two types of structural design with improved energy dissipation. Note that the traditional solid beam whose geometry can be described by Eqn. (4.1) is also studied for comparison, where H, T, L and B are referred to as global shape parameters.

4.3.1. LATTICE DESIGN

The lattice design studied in this paper is focused on planar structures (x-y plane) that can be extruded along the out-of-plane (z) direction. As illustrated in Fig. 4.2(a), lattice structures (LSs) are incorporated into a pre-shaped beam to form a hierarchical beam. Similar to the solid beam, global shape of the hierarchical beam can be described by H, L, T and B (conform Eqn. (4.1)). The distance between the top and bottom skin is denoted as T_v. The internal LS geometry can be described by two lattice parameters, i.e. t and θ, as depicted in Fig. 4.2(a). In addition, solid reinforcements with thickness D and $2D$ are introduced at the boundary and center, respectively (see Fig. 4.2(a)). The number of lattice cells (denoted as n_c) within the hierarchical beam is determined based on the following relation:

$$n_c = \text{int}[\frac{\int_0^L \sqrt{1+(\frac{dy}{dx})^2}dx - 4D}{2T_v\tan(\theta)+\frac{2t}{\cos(\theta)}}]-1, \tag{4.2}$$

where int represents a function that returns the integer part of a decimal number. Note that the hierarchical beam's mechanical properties are determined by a collective effect of the curved shape and the embedded lattices. As presented in Fig. 4.2(b), the designed hierarchical beam is then combined with rigid frames (in grey) to create a unit cell. By patterning such unit cells in 2D and 3D, multi-stable metastructures can be constructed accordingly (see Fig. 4.2(c)).

4.3.2. HOLLOW CROSS-SECTION DESIGN

Next to the lattice-based design, we also investigate hollow beams with a box-shaped cross section, as presented in Fig. 4.2(d)–(f). It can be seen that in addition to the global shape parameters, the hollow beam has an internal cross section that can be described by b_1 and t_1 (see Fig. 4.2(d)). These curved beams with a box-shaped cross section are referred to as hollow beams in the remainder of this paper. Hollow beams are constructed

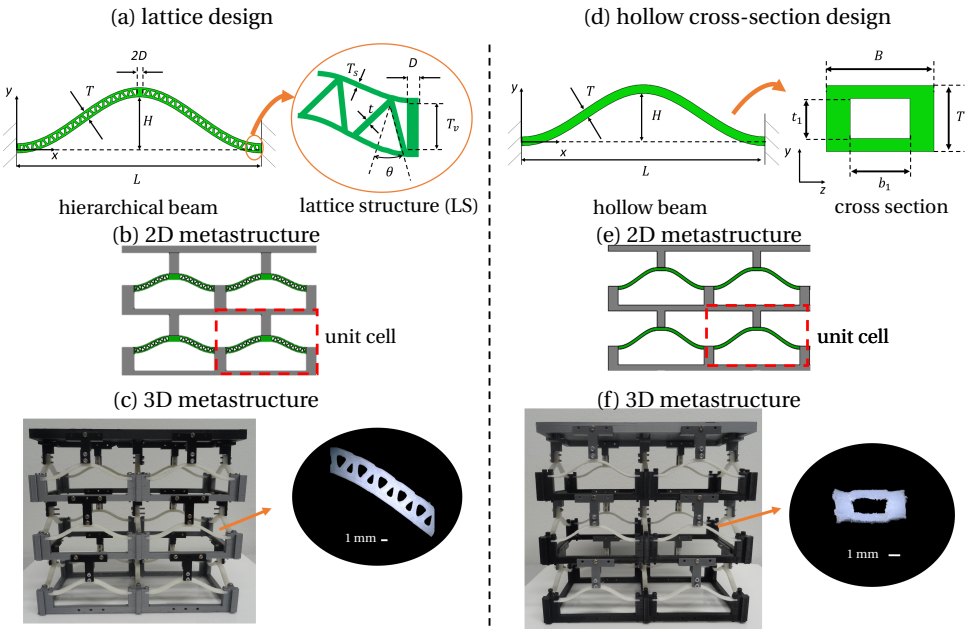

Figure 4.2: A schematic of the proposed designs. (a)–(c): The developed lattice-based metastructures. Geometric parameters of the hierarchical beam are depicted in (a). (d)–(f): Metastructures based on hollow beams with box-shaped cross sections.

by sweeping the box-shaped profile along the curved path (i.e. conform Eqn. (4.1)). The associated 2D and 3D metastructures are demonstrated in Fig. 4.2(e) and (f).

4.3.3. FABRICATION AND EXPERIMENTS

To experimentally evaluate the proposed structures, a series of samples is fabricated using fused deposition printing (Prusa i3-MK3 printer). The hierarchical, hollow and solid beams are printed with thermoplastic elastomers (Flex 98, RS), and frames are printed with a stiff material (polylactic acid, PLA). The beams and frames are assembled into unit cells by using screws. 3D multi-stable metastructures shown in Fig. 4.2(c) and (f) are built by assembling a series of unit cells. The material property of the elastomer is characterized by standard tensile measurements according to ASTM D638-14. The measured Young's modulus and Poisson's ratio are 87 MPa and 0.4, respectively.

Uniaxial loading tests are conducted to characterize the mechanical behavior. A displacement-controlled loading is applied using a universal testing system (ZwickRoell Z005). Specimens are loaded at the top with a crosshead speed of 10 mm/min, whereas the bottom edge of the specimen is fully clamped. The detailed information on the experimental setup can be found in Appendix C.2.

4.3.4. NUMERICAL SIMULATIONS

To simulate the snap-through transition, finite element analysis (FEA) is carried out using ABAQUS (Standard, 2017). In the case of hierarchical beams, 2D structural models are constructed. Triangular and quadrilateral plane-stress elements (CPS3 and CPS4) are used. Mesh convergence tests have been conducted to ensure accuracy. Boundary conditions are assigned in such a way that the left and right end are fully constrained, and a vertical displacement is applied at the center. For the hollow beams, eight-node solid elements (C3D8) are employed. Using the measured Young's modulus and Poisson's ratio, a linear elastic constitutive relation is adopted.

In addition to quasi-static simulations, impact simulations are carried out to investigate the protective capabilities of the proposed metastructures. For this, we investigate the impact performance of metastructures using ABAQUS/Explicit. Based on the material properties of PLA and elastomers, the mass density of frames and beam elements are taken as 1240 kg/m^3 and 1140 kg/m^3, respectively. A rectangular object with a mass density of 7900 kg/m^3 is placed above the metastructure. The object has a Young's modulus of 210 GPa and a Poisson's ratio of 0.3. An initial velocity and a gravitational acceleration of 9.8 m/s^2 are introduced.

4.4. MECHANICAL BEHAVIOR OF UNIT CELLS

In this section, we investigate and present the mechanical properties of unit cells. The snap-through transitions are analyzed experimentally and numerically.

4.4.1. SNAP-THROUGH BEHAVIOR

Hierarchical, hollow and solid beams with the same volume (V) are constructed, and their geometric parameters are depicted in Table 1 below. It should be noted that H, L, and B of the hierarchical and hollow beam are the same for all beams, and are fixed throughout this study. In contrast, the hierarchical and hollow beam have a larger in-plane thickness T than the solid beam, which leads to an enhanced bending stiffness. Here, the unit cell's snap-through behavior is characterized experimentally and numerically. In the numerical model, 37314 elements are used for meshing the 2D hierarchical geometry. In case of the hollow beam, the geometry is modeled with 72314 solid elements. The measured and simulated force-displacement ($F-d$) curves are shown in Fig. 4.3(b), where the displacement (d) is normalized by H. It can be observed that the experimental and numerical results are in a good agreement, and all three configurations exhibit snap-through transitions. Upon loading, F gradually reaches the maximum force (denoted as F_{max}). As the displacement increases further, the tangent stiffness switches to a negative value until the minimum force (denoted as F_{min}) is reached. Next, the tangent stiffness becomes positive again and the deformed stable state (State 2) shown in Fig. 4.3(a) can be realized. After releasing the load, the unit cell can stabilize at the State 2. When compared with the solid beam, both the hierarchical and the hollow beam can realize larger F_{max} and F_{min} due to the enlarged bending stiffness. Note that for the hierarchical and hollow beam, it is possible to tune T while keeping the volume unchanged. This tuning of T may result in further increase of F_{max} and F_{min}, as investigated in Section 4.4.2.

Table 1. Geometric parameters of unit cells.

	H [mm]	L [mm]	B [mm]	T [mm]	D [mm]	t/T_v	θ [°]	b_1/B	t_1/T	V [mm³]	bending stiffness [N/m]
hierarchical beam	16	80	6	2.55	1.0	0.4	25	\	\	999	**1.13** [*]
hollow beam	16	80	6	2.55	\	\	\	0.53	0.50	999	**1.29** [*]
solid beam	16	80	6	1.9	\	\	\	\	\	999	**0.58**

[*] The bending stiffness of the hierarchical and hollow beam is calculated using Eqn. (3) and (4), respectively.

4

The enhanced bending stiffness causes the beam to deform into a stable state with an higher strain energy. Here, strain energy (P) of the unit cell is derived by calculating the integral of F with respect to d, as shown in Fig. 4.3(c). It can be seen that State 2 of each beam corresponds to a local minimum in the strain energy, which mainly consists of bending and compression energy. After removing the external load, the strain energy can be stored within the deformed state (i.e. energy trapping [15]). For the hierarchical and hollow beams, the enlarged bending stiffness enables the structure to store more bending energy within the deformed stable state, enhancing the structure's energy trapping capability.

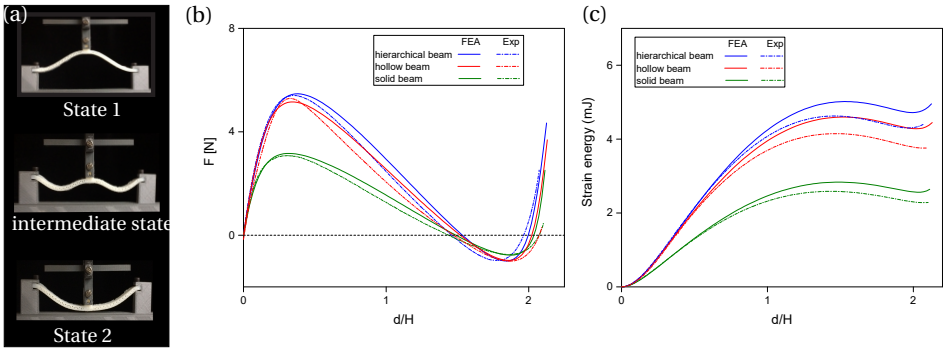

Figure 4.3: Snap-through behavior of unit cells. (a) Snapshots of a hierarchical beam during the un-axial loading. (b) The measured and simulated force-displacement curves of the hierarchical, hollow and solid beams. (c) Evolution of the unit cell's strain energy during the uniaxial loading.

4.4.2. TUNING OF SNAP-THROUGH BEHAVIOR

a. Hierarchical beams

For given H, L, and B, the hierarchical beam's bending stiffness can be further tuned by varying T, whereas the volume is kept constant. As noted in [42, 43], the hierarchical beam's bending stiffness (D_l) can be approximated as:

$$D_l = \frac{EI_2}{L^3(1-\nu^2\frac{I_1}{I_1+I_2})}, \text{ with } I_1 = \frac{t(T_v)^3}{6\cos(\theta)}, \; I_2 = B\frac{T_s^3+3T_s(T_v+T_s)^2}{6}, \text{ and } T_s = \frac{T-T_v}{2}, \tag{4.3}$$

where E and ν represent Young's modulus and Poisson's ratio of the material, and T_s represents thickness of the skin (see Fig. 4.2(a)). From Eqn. (4.3), it can be seen that changing lattice parameters (t and θ) has minor influence on the bending stiffness, whereas D_l can be effectively tuned by changing the in-plane thickness T. Thus, we study effects of T on the critical loads (F_{max} and F_{min}). Furthermore, it is worth mentioning that the hierarchical beam normally has lower axial stiffness than the solid beam with the same volume [42]. This is because the inclined lattice planes could not effectively bear the axial load, resulting in a reduction of their axial stiffness. Specifically, the thickness T is varied, while the volume is kept constant by adjusting t. Simulated and measured results are shown in Fig. 4.4(a), where F_{max} and F_{min} of the hierarchical beams are normalized by the counterpart of the solid beam. It can be seen that as compared to F_{min}, F_{max} is more sensitive to the change of the thickness. As T increases, it is possible to increase F_{max} to be two times as large as that of the solid beam. The increase of the critical load is mainly attributed to increasing of the bending stiffness. However, further increasing T will result in local buckling, which causes the strain and stress to increase dramatically at the local region. For example, when T shown in Fig. 4.4(a) is taken as 2.8 mm, local buckling happens for segments near the boundary (see Fig. 4.4(b)). This local buckling behavior is caused by the fact that under the constant volume constraint, increasing the thickness (T) leads to a decrease of the lattice thickness t. As a result, slenderness of the segment and the lattice are increased, making the structure prone to buckling.

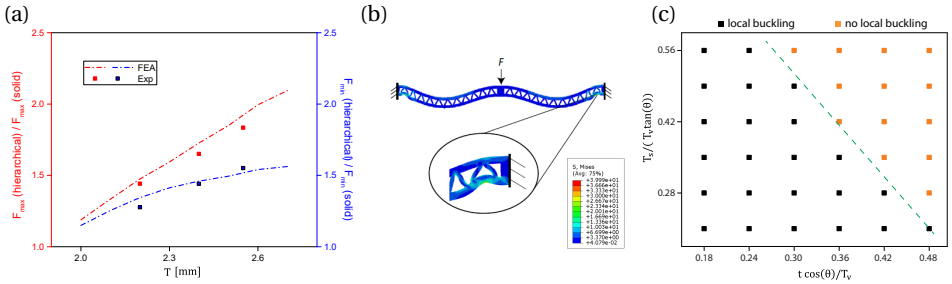

Figure 4.4: Tuning the hierarchical beam's snap-through behavior via varying the thickness T. (a) Experimentally and numerically characterized critical loads as a function of T. (b) The local buckling. (c) Effect of the lattice parameters on the local buckling.

To further explore the effect of the lattice parameters on the local buckling, a parametric study is carried out using finite element models. The corresponding results are shown in Fig. 4.4(c). In this figure, t and T_s are normalized by $\frac{T_v}{\cos(\theta)}$ and $T_v\tan(\theta)$, respectively. Orange dots represent that the hierarchical beam is able to snap into the second stable state without local buckling. Black dots indicate that local buckling behavior occurs. For relatively large t and T_s, the structure exhibits no local buckling. However, when t and T_s are reduced, the outer skin or the inner lattice become thinner, leading to

local buckling. In order to achieve proper energy dissipation, it is important to ensure the lattice geometry to fall into the orange region.

b. Hollow beams

For hollow beams, the overall thickness T can also be tuned, whereas the volume is kept constant. Note that due to the volume constraint, the hollow beam has the same axial stiffness as that of the solid beam because they have the same cross-sectional area. Here, T of the hollow beam is varied and its influence on the critical loads is studied. When varying T, t_1 is adjusted subsequently for keeping the volume constant. In particular, the hollow beam's bending stiffness (D_h) can be expressed as:

$$D_h = \frac{1 - \frac{b_1}{B}(\frac{t_1}{T})^3}{12L^3}(BT^3). \tag{4.4}$$

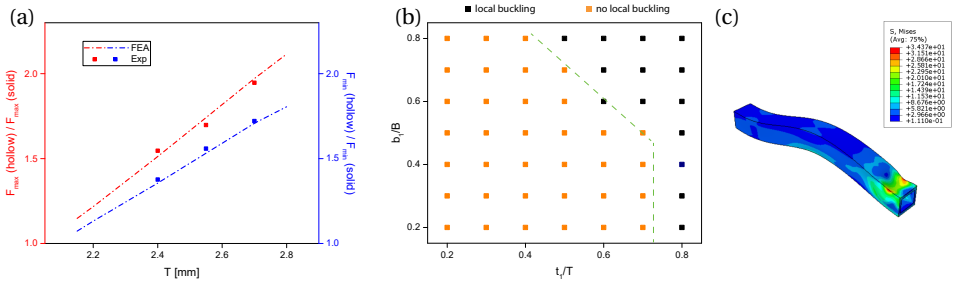

Figure 4.5: Tuning the critical loads for the hollow beam. (a) Experimentally and numerically characterized critical loads are plotted as a function of T. (b) The effect of the inner cross-sectional parameters (b_1 and t_1) on local buckling. (c) The local buckling of the hollow beam.

It can be noted from Eqn. (4.4) that T has a dominant effect on D_h. Results presented in Fig. 4.5(a) verify that enlarging T can lead to an increase of both F_{max} and F_{min} when compared with the solid beam. Moreover, it can be observed that by tuning the thickness, F_{max} of the hollow beam can be two times larger than that of the solid beam. Although further increasing T can give rise to larger D_h, the snap-through transition will be suppressed by local buckling, similar to the hierarchical beam. For the hollow beam, as the volume is kept constant, increasing T causes t_1 to increase rapidly. Consequently, t_1/T increases at close to 1 and the hollow beams' walls become thinner. Effects of b_1/B and t_1/T on local buckling are studied numerically. From Fig. 4.5(b), it can be seen that when b_1/B or t_1/T is close to 1, local buckling occurs, as illustrated in Fig. 4.5(c). During the loading, the slender wall experiences high compressive stresses due to the bending as well as the axial compression. As a result, the hollow beam can not realize the second stable state. It can be expected that changing the thickness (T) offers the potential to further enhance the metastructure's energy dissipation, whereas it has to be constrained within a certain range to avoid local buckling.

4.4.3. BI-STABLE BEHAVIOR

Previous studies have shown that the ratio of the height to the thickness (H/T) is an important quantity for solid beams to realize bi-stable behavior [40, 44]. When H/T of the solid beam is smaller than a certain value, the structure exhibits mono-stable behavior ($F_{min} > 0$). As compared to the solid beam, the hierarchical and the hollow beam have different geometric parameters, making their bi-stable criterion distinct from the solid beam. Here, bi-stability of the hierarchical and hollow beam is studied numerically.

For hierarchical beams, the lattice parameters (t and θ) have a minor influence on F_{min} because changing lattice parameters results in a small variation of the bending stiffness (see Eqn. (4.3)). As a result, varying t and θ do not affect bi-stability much (see Appendix C.3). Based on this observation, we study the bi-stability criterion for hierarchical beams on the basis of two normalized quantities H/T and T_v/T, as presented in Fig. 4.6(a). In this figure, the yellow region indicates bi-stability ($F_{min} < 0$), while the grey area represents mono-stable behavior. The boundary corresponding to $F_{min} = 0$ is denoted as a red curve. Note that when T_v equals zero, it corresponds to the solid beam. Results show that the required H/T for the hierarchical beam to realize bi-stability is larger than that of the solid beam. Different from the solid beam, the hierarchical beam's bi-stability criterion is not only dependent on H/T, but also is influenced by T_v/T. When T_v increases, a larger H/T is required for achieving the second stable state. This happens because tuning T_v results in an evident change of the bending stiffness, which will affect F_{min} significantly.

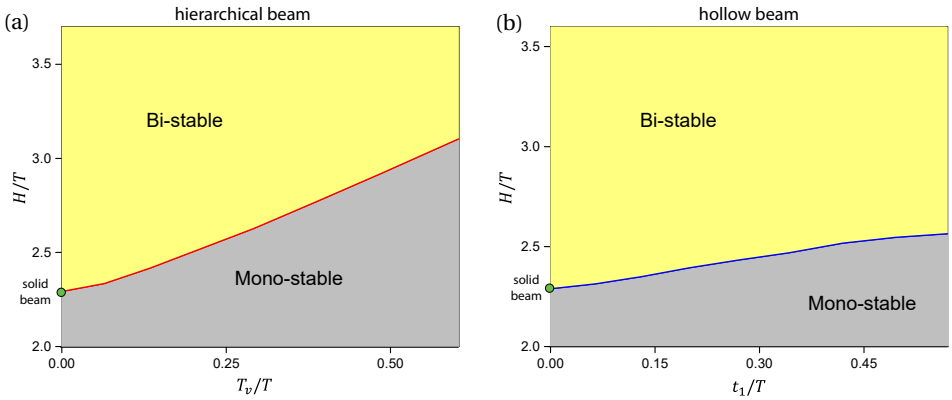

Figure 4.6: The bi-stable criterion for the hierarchical and hollow beam. (a) With changing H/T and T_v/T, the bi-stable region for hierarchical beams can be identified. (b) For the hollow beam, the bi-stable region is plotted as a function of H/T and t_1/T.

In addition, the bi-stability criterion for hollow beams is investigated based on two normalized quantities H/T and t_1/T. From Fig. 4.6(b), it can be noted that for low values of H/T, the structure exhibits mono-stable behavior. The critical H/T corresponding to $F_{min} = 0$ (blue curve) increases as t_1/T increases. Therefore, when designing bi-stable hollow beams, both H and t_1 should be properly selected. Compared to the hierarchical beam, variation of the critical H/T for bi-stability is not significant. This is because

the effect of t_1 on the structural bending stiffness is not as evident as that of T_v (see Eqn. (4.4)).

4.5. MULTI-STABLE METASTRUCTURES

In this section, the energy dissipation of metastructures is investigated. As discussed in Section 4.2, metastructures comprising a series of snap-through units can achieve energy dissipation such that the dissipated energy can be quantified as an hysteresis loop in the loading-unloading process. Here we analyze the metastructures' hysteresis characteristics and study their energy absorption capability. Note that the metastructures are formed by arranging the unit cells in three directions, leading to multiple stable configurations for the metastructures (see Fig. 4.7(a)). Due to inevitable manufacturing imperfections, units will exhibit slightly different critical loads, resulting in a sequential snap-through transition.

4.5.1. ENERGY ABSORPTION UNDER A LOADING-UNLOADING CYCLE

Based on the proposed lattice-based and hollow cross-section design, five-layer multi-stable metastructures are studied. Furthermore, metastructures consisting of solid beams (traditional design) are also fabricated. For the sake of simplicity, metastructures based on the lattice, hollow cross-section and traditional design are referred to as LM, HM, and TM, respectively, in the remainder of this chapter. It should be noted that LM, HM, and TM have the same mass.

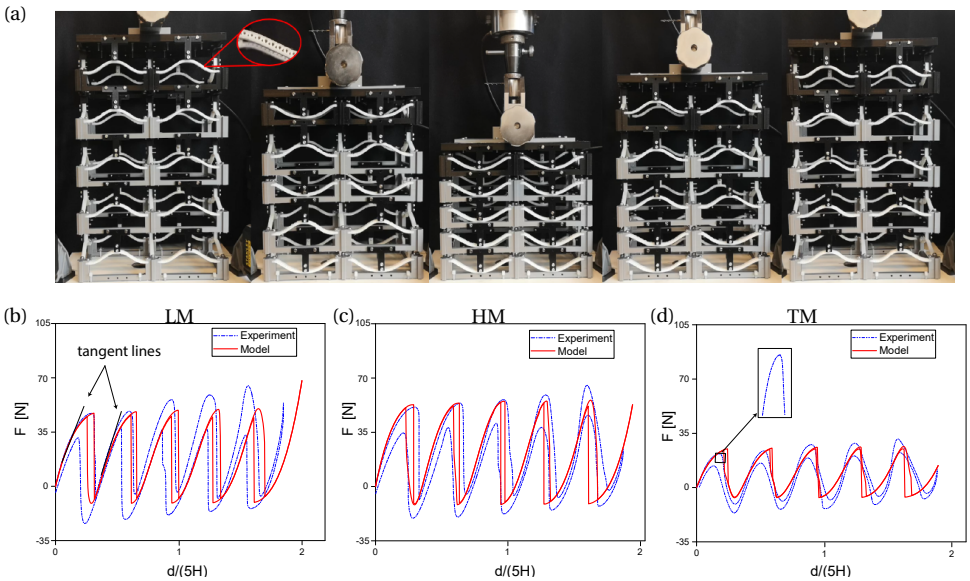

Figure 4.7: Mechanical responses of multi-stable metastructures under displacement-controlled cyclic loading. (a) Different deformation stages of the LM in a loading-unloading test. (b)–(d) Force-displacement curves of the LM, HM, and TM under a complete displacement-controlled loading and unloading cycle.

Cyclic loading tests are performed on each metastructure. Figure 4.7(a) shows different stages of the loading-unloading process of the LM. During loading, the snap-through sequence (i.e. which layer snaps first) is mainly determined by the inevitable manufacturing and assembly imperfections, which cause a sequential buckling from the weakest to the strongest layer. Measured force-displacement responses of the LM, HM and TM under a complete displacement-controlled loading–unloading cycle are denoted as blue dashed lines in Fig. 4.7(b)–(d). It can be seen that as the displacement increases, the slope of tangent lines, as highlighted in Fig. 4.7(b), increases. This is due to the fact that the stiffness of each layer's deformed state is larger than that of the initial state. As a result, when more layers flip into the deformed state, the effective tangent stiffness increases. Moreover, a force drop can be clearly observed when reaching F_{max}, in particular, for the LM and HM. That is, one layer jumps from one configuration to another with some mechanical energy dissipated to heat. Similarly, during the unloading process, when the minimum force is reached, the load increases suddenly, resulting in a configurational transformation. Consequently, an hysteresis can be identified, as displayed in the figures. It should be noted that the force drop also occurs for the TM (see Fig. 4.7(d)) even though it is not as evident as that of the LM and HM. In addition, force-displacement curves of the metastructures may be influenced by the polymer's cyclic softening, which will result in a reduction of critical loads after a few loading-unloading cycles [45]. Here, it is found that for the thermoplastic elastomer we used, the softening effect is small (see Appendix C.4).

Moreover, results shown in Fig. 4.7(b)–(d) indicate that for a given amount of material, the proposed lattice-based and hollow cross-section design can effectively give rise to a larger hysteresis loop (i.e. energy dissipation capability) when compared with the TM. The critical forces, in particular F_{max}, are significantly increased due to the enhanced bending stiffness. As discussed in Section 4.2, the increase of the bending stiffness generates higher critical forces, enhancing the energy absorption for multi-stable metastructures. As a result, evident and large hysteresis can be captured in the LM and HM.

In addition to the qualitative comparison, we also investigate the energy dissipation quantitatively. Specifically, an analytical calculation is carried out to predict the force-displacement response of n-layer metastructures. The analytical model is based on the following steps: i) the measured force-displacement curve of the unit cell is firstly fitted as a polynomial function $F(d)$. Next, the corresponding strain energy $P(d)$ is obtained by an integration of $F(d)$ with respect to d. ii) each layer of the n-layer metastructure is assumed as a structural element whose behavior is governed by $F(d)$ and $P(d)$. Hence, the metastructure possesses n degrees of freedom, which are defined as $(d_1, d_2, d_3 ... d_n)$. Note that d_i represents deformation of the i-th layer. iii) in order to obtain the force-displacement curve, we solve the following optimization problem:

$$\begin{aligned} &\min_{d_i} \quad E(d_1, d_2, d_3 ... d_n) \\ &\text{subject to} \quad d_1 + d_2 + d_3 ... + d_n = d_{inp}, \end{aligned} \tag{4.5}$$

where $E(d_1, d_2, d_3 ... d_n)$ is the strain energy of the n-layer metastructure, and d_{inp} is the prescribed displacement at the top of the metastructure. Once $(d_1, d_2, d_3 ... d_n)$ are solved,

the reaction force can be obtained by substituting one component d_i to compute $F(d_i)$. To ensure a sequential snapping deformation, we introduce imperfections by varying the critical loads of each layer by 0.5%. This optimization problem is solved using the fmincon interior-point algorithm implemented in Matlab. Calculated results are plotted as red lines in Fig. 4.7(b)–(d). From the figures, it can be seen that the model is able to capture the hysteresis loop caused by the snap-through transition associated with the force jump, well demonstrating the dynamic snapping as well as the energy dissipation. In addition, it is noted that there is a quantitative difference of dissipated energy between the experiments and models. That is, the area of the hysteresis loop in experiment is larger than that of the models, with differences in the range of 30%–50%. This discrepancy is caused by two factors: i) In experiments, apart from the dynamic snapping, the viscosity of polymers also contribute to the hysteresis loop, enlarging the dissipated energy. In the model, the viscous material damping is not taken into account as our focus is on the snap-through induced energy dissipation. It can be expected the error can be largely reduced when an appropriate visco-elastic constitutive relation is adopted; ii) Due to inevitable manufacturing imperfections, the beam units' mechanical properties (e.g, critical forces) are different even though they are designed to be identical. This also causes the difference between the experiments and models in terms of the amount of dissipated energy.

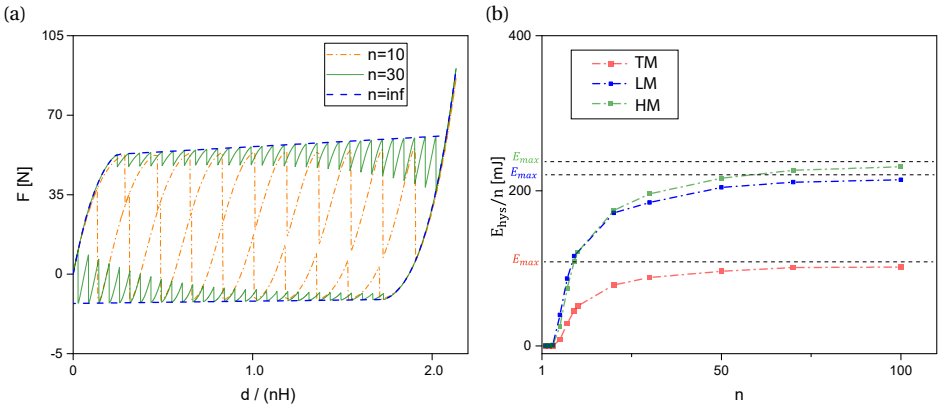

Figure 4.8: Energy dissipation of n-layer metastructures. (a) The predicted force-displacement curves of n-layer metastructures. (b) The comparison between the LM, HM, and TM in terms of energy dissipation. E_{max} represents the maximal energy that can be dissipated per layer in a load-unloading process.

Using this model, we further investigate the relation between the energy dissipation and the number of layers. Force-displacement responses of metastructures with different amount (n) of layers are shown in Fig. 4.8(a). It can be seen that as n increases, more layers experience the force jump. Furthermore, it can be seen that the enclosed hysteresis for each jump (loading-unloading) becomes larger as n increases, leading to an increase of the energy dissipation of each layer [23, 24]. For instance, compared to the 10-layer metastructure, an enlarged hysteresis can be observed for the 30-layer metastructure. When n becomes very large, the associated hysteresis will be enclosed by

two straight lines at F_{max} and F_{min}, as illustrated in Fig. 4.8(a). In this case, each layer reaches its maximum energy dissipation capacity, which can be approximated as:

$$E_{max} \approx 2H(F_{max} - F_{min}), \tag{4.6}$$

where E_{max} is the maximal hysteresis area that can be achieved for each layer under a loading-unloading cycle (i.e. the area enclosed by the blue dashed curves in Fig. 4.8(a)). Therefore, in order to improve the energy absorption, it is important to increase the absolute value of both F_{max} and F_{min}.

Figure 4.8(b) presents quantitative comparison of the n-layer LM, HM, and TM in terms of energy dissipation. Here, area of the hysteresis loop (denoted as E_{hys}) is divided by n, which represents energy dissipation per layer. Results show that as n increases, there is a dramatic increase of E_{hys}/n. Further increasing n will cause E_{hys}/n to converge to the theoretical limit, namely E_{max} (see Fig. 4.8(b)). Furthermore, it can be seen that the metastructure's energy dissipation can be largely enhanced by the proposed designs. Note that for the LM and HM, this enhancement can be further tuned by changing its in-plane thickness (T), whereas the total volume is kept constant. Therefore, as compared to TM, the proposed LM and HM offer a larger design space to tune the energy dissipation. It should be noted that in case of fabricating LM or HM with small features, more precise printing technique, like stereolithography (SLA), can be used. Apart from high resolutions, the SLA process also allows to print 3D metastructures directly without the manual assembly, simplifying the fabrication process.

4.5.2. CUSHION PERFORMANCE OF METASTRUCTURES UNDER IMPACT

In addition to energy dissipation under quasi-static cyclic loading, multi-stable metastructures can also function as a buffer to protect an object from impact. To demonstrate this protective capability, here we study impact performance of the metastructures numerically. In particular, 2D structural geometries for the LM and TM are constructed, and the structural dimensions can be found in Table 1. Figure 4.9(a) displays different stages of a three-layer LM's deformations under an impact load, for which an object with an initial velocity (v_0) drops from a certain height (h_0) above the metastructure. As shown in this figure, all three layers snap into the deformed state. Note that the number of snapped layers depends on the object's mechanical energy. The impact energy capacity (E_{imp}) for the multi-stable metastructure represents a critical mechanical energy that causes all layers to snap during the impact loading [15, 46]. Here, a range of v_0 is given in the finite element models, and the impact energy is obtained by calculating the sum of the gravitational potential and kinetic energy of the object. It can be expected that as the impact energy increases, more layers will snap. In the numerical models, the critical impact energy that causes all layers to snap is monitored, namely E_{imp}. Results for multiple LMs and TMs with different layers are presented in Fig. 4.9(b). It can be seen that the introduced lattice is able to improve the structural cushion performance by means of sustaining a larger range of impact energy. Moreover, the impact force experienced by the ground is extracted from the simulations. Figure 4.9(c) presents the peak force for the LM and TM design when different v_0 is taken. It can be seen that the proposed LM design leads to a smaller impact force compared to the TM, indicating better cushion performance in force mitigation. Since the LM exhibits similar snap-through response

as the HM, it can be expected that the HM design can also enhance the structural impact performance when compared with the TM.

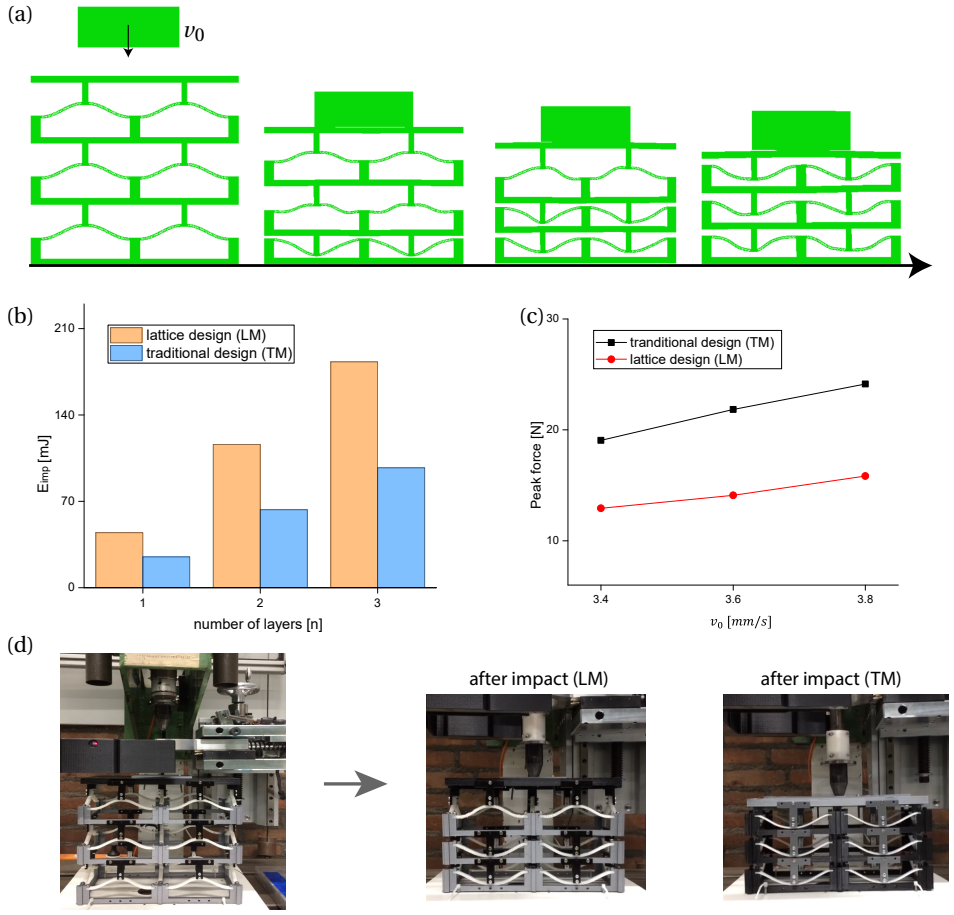

Figure 4.9: Protective capability of multi-stable metastructures. (a) Different stages of metastructures' deformations under an impact. (b) The simulated critical mechanical energy (E_{imp}) of the LM and TM. (c) Simulated peak forces for the TM and LM design. (d) Experimental demonstration of the impact performance for the LM and TM.

To demonstrate this improvement of cushion performance in practice, we perform a drop test using an in-house impact setup. As shown in Fig. 4.9(d), an impactor with a mass of 1.7 kg drops from a controlled height to the top surface of metastructures. Under the same initial height (160 mm), two layers of LM snap into the deformed state during the impact loading, whereas all three layers of the TM flip to the deformed state. This demonstrates that compared to the TM, the proposed designs enable metastructures to carry a larger range of impact loads with an enhanced cushion performance.

4.6. EXTENSION TO SHELLS

The proposed design strategy of increasing structural bending stiffness is not restricted to beams and can be extended to shell structures. In this section, we demonstrate this potential by developing a type of lattice-based shell with enhanced bending stiffness. As shown in Fig. 4.10(a), a shell structure can be constructed by a revolution of the 2D beam profile along the axis of rotation. Here, a lattice-based beam design is adopted, resulting in a hierarchical shell. A real demonstration of the shell structure fabricated with stereolithography printing (Prusa SL-1S) is presented in Fig. 4.10(b). Dimensions of the associated hierarchical beam profile are shown in the inset table.

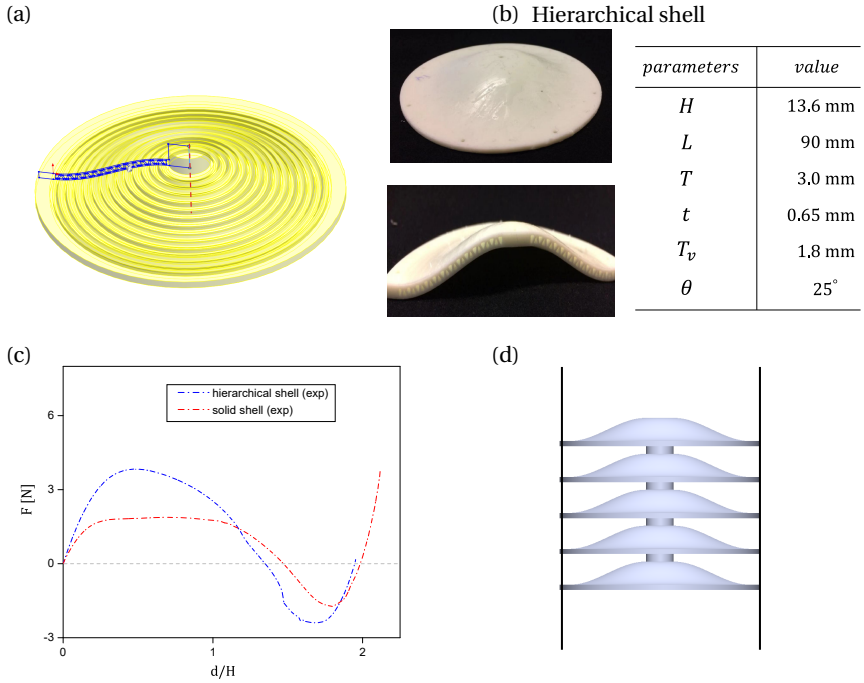

parameters	*value*
H	13.6 mm
L	90 mm
T	3.0 mm
t	0.65 mm
T_v	1.8 mm
θ	25°

Figure 4.10: The lattice-based shell structures. (a) The shell structure is developed by a revolution of the hierarchical beam profile (in blue) along the axis of rotation (red dashed line). (b) A real demonstration of the shell and its cross section. Geometric parameters are depicted. (c) The experimentally characterized force-displacement responses of the hierarchical and the solid shell. (d) An illustration of a serial arrangement of hierarchical shells for energy absorption.

To demonstrate the improvement of mechanical response, we also fabricate solid shells with the same mass and conduct displacement-controlled loading tests. Measured force-displacement curves in Fig. 4.10(c) show that the hierarchical shell is able to enhance the snap-through transition in such a way that it exhibits larger critical loads than the solid shell. More importantly, it can be expected that when connecting multiple hierarchical shells in series, as illustrated in Fig. 4.10(d), the entire system is able to achieve a stiffer mechanical response than the previously reported structure that comprises a series of solid shells [47]. As a result, the energy dissipation capability of the shell

structures can be effectively improved. The extension to shells here demonstrates generalization of the proposed concept, which can be used for enhancing energy dissipation of the solid shells. Although the lattice-based shell structure shows similarities with the hierarchical beam in terms of snap-through responses, its design space and energy absorption capability differ from that of the beam-type metastructures. Future research will be conducted to investigate energy dissipation of the hierarchical shells.

4.7. CONCLUSIONS

This paper presents a novel design of multi-stable metastructures with enhanced energy dissipation, based on the improvement of the structural bending stiffness. It is found that tuning the unit cells' bending stiffness while keeping the volume constant can result in a large benefit in terms of critical forces and energy dissipation. Two types of structural designs (the lattice-based and hollow cross-section design) are proposed for multi-stable metastructures. The snap-through transitions have been studied based on experimental and numerical approaches. Results show that snap-through transitions of the proposed structures can be further tuned by changing the beam thickness, leading to an effective tuning of the bending stiffness. Further increasing thickness will result in local buckling, which has been identified for the lattice-based and hollow cross-section design. Furthermore, it has been shown that as compared to metastructures consisting of solid beams, the proposed structures can lead to an improved energy dissipation by approximately a factor two. Moreover, the presented designs enable metastructures to sustain a larger impact energy with an enhanced impact performance. It has been demonstrated that the proposed strategy is not only applicable to beams, but also can be extended to shell structures. Our findings provide a new way to enhance the performance of multi-stable metastrutures for the application of energy absorption.

REFERENCES

[1] J. C. Dixon, *The shock absorber handbook* (John Wiley & Sons, 2008).

[2] C. Shen, G. Lu, and T. Yu, *Dynamic behavior of graded honeycombs–a finite element study,* Composite structures **98**, 282 (2013).

[3] Z. Wang, *Recent advances in novel metallic honeycomb structure,* Composites Part B: Engineering **166**, 731 (2019).

[4] W. He, L. Yao, X. Meng, G. Sun, D. Xie, and J. Liu, *Effect of structural parameters on low-velocity impact behavior of aluminum honeycomb sandwich structures with cfrp face sheets,* Thin-Walled Structures **137**, 411 (2019).

[5] G. Sun, D. Chen, X. Huo, G. Zheng, and Q. Li, *Experimental and numerical studies on indentation and perforation characteristics of honeycomb sandwich panels,* Composite Structures **184**, 110 (2018).

[6] G. Sun, X. Huo, D. Chen, and Q. Li, *Experimental and numerical study on honeycomb sandwich panels under bending and in-panel compression,* Materials & Design **133**, 154 (2017).

[7] J. Shen, G. Lu, and D. Ruan, *Compressive behaviour of closed-cell aluminium foams at high strain rates,* Composites Part B: Engineering **41**, 678 (2010).

[8] M. Islam, M. Kader, P. Hazell, J. Escobedo, A. Brown, and M. Saadatfar, *Effects of impactor shape on the deformation and energy absorption of closed cell aluminium foams under low velocity impact,* Materials & Design **191**, 108599 (2020).

[9] N. Hu and R. Burgueño, *Buckling-induced smart applications: recent advances and trends,* Smart Materials and Structures **24**, 063001 (2015).

[10] K. Bertoldi, V. Vitelli, J. Christensen, and M. van Hecke, *Flexible mechanical metamaterials,* Nature Reviews Materials **2**, 17066 (2017).

[11] A. Rafsanjani, K. Bertoldi, and A. R. Studart, *Programming soft robots with flexible mechanical metamaterials,* Science Robotics **4** (2019).

[12] H. Y. Jeong, S.-C. An, Y. Lim, M. J. Jeong, N. Kim, and Y. C. Jun, *3d and 4d printing of multistable structures,* Applied Sciences **10**, 7254 (2020).

[13] G. Simitses and D. H. Hodges, *Fundamentals of structural stability* (Butterworth-Heinemann, 2006).

[14] X. Tan, S. Chen, B. Wang, S. Zhu, L. Wu, and Y. Sun, *Design, fabrication, and characterization of multistable mechanical metamaterials for trapping energy,* Extreme Mechanics Letters **28**, 8 (2019).

[15] S. Shan, S. H. Kang, J. R. Raney, P. Wang, L. Fang, F. Candido, J. A. Lewis, and K. Bertoldi, *Multistable architected materials for trapping elastic strain energy,* Advanced Materials **27**, 4296 (2015).

[16] Y. Song, R. M. Panas, S. Chizari, L. A. Shaw, J. A. Jackson, J. B. Hopkins, and A. J. Pascall, *Additively manufacturable micro-mechanical logic gates,* Nature communications **10**, 1 (2019).

[17] D. M. Correa, T. Klatt, S. Cortes, M. Haberman, D. Kovar, and C. Seepersad, *Negative stiffness honeycombs for recoverable shock isolation,* Rapid Prototyping Journal **21**, 193 (2015).

[18] G. Puglisi and L. Truskinovsky, *Mechanics of a discrete chain with bi-stable elements,* Journal of the Mechanics and Physics of Solids **48**, 1 (2000).

[19] R. C. Rogers and L. Truskinovsky, *Discretization and hysteresis,* Physica B: Condensed Matter **233**, 370 (1997).

[20] C. Findeisen, J. Hohe, M. Kadic, and P. Gumbsch, *Characteristics of mechanical metamaterials based on buckling elements,* Journal of the Mechanics and Physics of Solids **102**, 151 (2017).

[21] G. Puglisi and L. Truskinovsky, *Rate independent hysteresis in a bi-stable chain,* Journal of the Mechanics and Physics of Solids **50**, 165 (2002).

[22] I. Benichou and S. Givli, *Structures undergoing discrete phase transformation,* Journal of the Mechanics and Physics of Solids **61**, 94 (2013).

[23] S. Liu, A. I. Azad, and R. Burgueño, *Architected materials for tailorable shear behavior with energy dissipation,* Extreme Mechanics Letters **28**, 1 (2019).

[24] D. Restrepo, N. D. Mankame, and P. D. Zavattieri, *Phase transforming cellular materials,* Extreme Mechanics Letters **4**, 52 (2015).

[25] S. Sun, N. An, G. Wang, M. Li, and J. Zhou, *Snap-back induced hysteresis in an elastic mechanical metamaterial under tension,* Applied Physics Letters **115**, 091901 (2019).

[26] H. Yang and L. Ma, *Multi-stable mechanical metamaterials with shape-reconfiguration and zero poisson's ratio,* Materials & Design **152**, 181 (2018).

[27] D. A. Debeau and M. R. Haberman, *Impact behavior of negative stiffness honeycomb materials,* Journal of Materials Research **33**, 290 (2018).

[28] K. Che, C. Yuan, J. Wu, H. J. Qi, and J. Meaud, *Three-dimensional-printed multistable mechanical metamaterials with a deterministic deformation sequence,* Journal of Applied Mechanics **84**, 011004 (2017).

[29] A. Rafsanjani, A. Akbarzadeh, and D. Pasini, *Snapping mechanical metamaterials under tension,* Advanced Materials **27**, 5931 (2015).

[30] T. A. Hewage, K. L. Alderson, A. Alderson, and F. Scarpa, *Double-negative mechanical metamaterials displaying simultaneous negative stiffness and negative poisson's ratio properties,* Advanced Materials **28**, 10323 (2016).

[31] J. Hua, H. Lei, Z. Zhang, C. Gao, and D. Fang, *Multistable cylindrical mechanical metastructures: Theoretical and experimental studies,* Journal of Applied Mechanics , 1 (2019).

[32] H. Yang and L. Ma, *1d and 2d snapping mechanical metamaterials with cylindrical topology,* International Journal of Solids and Structures (2020).

[33] T. Frenzel, C. Findeisen, M. Kadic, P. Gumbsch, and M. Wegener, *Tailored buckling microlattices as reusable light-weight shock absorbers,* Advanced Materials **28**, 5865 (2016).

[34] Y. Zhang, Q. Wang, M. Tichem, and F. van Keulen, *Design and characterization of multi-stable mechanical metastructures with level and tilted stable configurations,* Extreme Mechanics Letters **34**, 100593 (2020).

[35] C. S. Ha, R. S. Lakes, and M. E. Plesha, *Cubic negative stiffness lattice structure for energy absorption: Numerical and experimental studies,* International Journal of Solids and Structures **178**, 127 (2019).

[36] C. S. Ha, R. S. Lakes, and M. E. Plesha, *Design, fabrication, and analysis of lattice exhibiting energy absorption via snap-through behavior,* Materials & Design **141**, 426 (2018).

[37] C. Ren, D. Yang, and H. Qin, *Mechanical performance of multidirectional buckling-based negative stiffness metamaterials: an analytical and numerical study,* Materials **11**, 1078 (2018).

[38] Y. Zhang, D. Restrepo, M. Velay-Lizancos, N. D. Mankame, and P. D. Zavattieri, *Energy dissipation in functionally two-dimensional phase transforming cellular materials,* Scientific reports **9**, 1 (2019).

[39] B. Haghpanah, A. Shirazi, L. Salari-Sharif, A. G. Izard, and L. Valdevit, *Elastic architected materials with extreme damping capacity,* Extreme Mechanics Letters **17**, 56 (2017).

[40] J. Qiu, J. H. Lang, and A. H. Slocum, *A curved-beam bistable mechanism,* Journal of microelectromechanical systems **13**, 137 (2004).

[41] Y. Zhang, M. Tichem, and F. van Keulen, *Rotational snap-through behavior of multistable beam-type metastructures,* International Journal of Mechanical Sciences **193**, 106172 (2021).

[42] T.-S. Lok and Q.-H. Cheng, *Elastic stiffness properties and behavior of truss-core sandwich panel,* Journal of Structural Engineering **126**, 552 (2000).

[43] D. Zangani, M. Robinson, and A. Gibson, *Evaluation of stiffness terms for z-cored sandwich panels,* Applied Composite Materials **14**, 159 (2007).

[44] J. Hua, H. Lei, C.-F. Gao, X. Guo, and D. Fang, *Parameters analysis and optimization of a typical multistable mechanical metamaterial,* Extreme Mechanics Letters **35**, 100640 (2020).

[45] A. Avanzini and D. Gallina, *Effect of cyclic strain on the mechanical behavior of a thermoplastic polyurethane,* Journal of engineering materials and technology **133** (2011).

[46] F. Pan, Y. Li, Z. Li, J. Yang, B. Liu, and Y. Chen, *3d pixel mechanical metamaterials,* Advanced Materials **31**, 1900548 (2019).

[47] M. Alturki and R. Burgueño, *Multistable cosine-curved dome system for elastic energy dissipation,* Journal of Applied Mechanics **86**, 091002 (2019).

5

DESIGN OF A METASTRUCTURE-BASED MULTI-STABLE SURFACE

The snap-through transition of multi-stable metastructures is not only beneficial for energy absorption, but also is advantageous to shape reconfiguration. In this chapter, we present the design of a metastructure-based morphing surface that is able to exhibit a series of stable configurations with different curvatures. Using theoretical, numerical, and experimental approaches, we study the snap-through transition between the initially flat and the curved stable configurations. Effects of geometric parameters on the snap-through and curvatures are systematically investigated. Results show that the beam thickness is important for tuning the snap-through response, while the curvature can be tuned by changing the beam height and the horizontal span of the structures. Furthermore, an analytical model is developed to investigate the structural nonlinear deformations. It is shown that the proposed model can predict the snap-through transition properly. The structural stability can be controlled by setting proper values for t/L and h/L (t, h, and L represents the beam thickness, height and span, respectively). Finally, it is demonstrated that based on two-dimensional arrangements of bi-stable elements, various stable configurations, like corrugations in different directions, can be imposed to the surface.

This chapter is based on a journal paper: Y. Zhang, M. Tichem, F. van Keulen, (2021). Concept and Design of a Metastructure-Based Multi-stable Surface, Extreme Mechanics Letters, (accepted).

5.1. INTRODUCTION

Imparting a curvature change to a surface is important for applications of morphing airfoils [1–4], deployable structures [5, 6], adaptive optical devices [7–9], and fluid control [10, 11]. Surfaces that are capable of changing their shapes into a series of deformed configurations are often referred to as morphing surfaces [12, 13]. The reconfigurability of morphing surfaces makes it possible to realize tunable functionalities. For instance, a change of surface topography can lead to different focal properties for optical display applications [14]. To retain a curved surface, bi-stability has been commonly explored to avoid prolonged actuation after shape reconfiguration.

In order to realize stable configurations, various bi-stable structural prototypes, e.g., compliant plates and shells, have been presented in literature [15, 16]. For instance, one type of bi-stable morphing structures is the composite laminate shell, which can exhibit two stable cylindrical shapes [17]. The bi-stability is mainly attributed to residual stresses introduced during the manufacturing process, causing the shell to be curved after cooling. Thus, the laminated shells' mechanical properties and stable configurations are highly dependent on the laminate's in-plane layups [18]. However, there are a few limitations for the bi-stable laminated shells, namely, i) they are difficult to fabricate at small scale; ii) the choice of materials is limited. Alternatively, bi-stable behavior can be achieved by using homogeneous materials in a spherical cap-type shell design [19–21]. Under compression, the cap-shaped shells can flip into an 'inverted' stable state. Analytical and numerical studies have demonstrated that the snap-through transition of the spherical shells can be tuned by changing the shell's geometry, such as thickness and radius [22, 23]. Moreover, Loukaides *et al.* [24] extended these cap-shaped shells to a grid-shell design with inner structures, for which the snap-through transition can be further manipulated by tuning local geometries.

Apart from bi-stability, multi-stable behavior can also be implemented into morphing surfaces. From the perspective of structural morphing, multi-stability allows for more versatile designs. To achieve this, a few studies have focused on combining multiple bi-stable shells to design multi-stable structures. Following this strategy, many multi-stable surfaces have been presented [25–30]. For example, Dai *et al.* [26] designed a type of morphing surfaces by assembling few bi-stable shells, demonstrating the potential to realize a wavy skin for shape morphing. Cui *et al.* [25] characterized the coupling effects between bi-stable elements and demonstrated a quad-stable surface design. However, the mechanical response of these multi-stable surfaces can be significantly affected by the joints and only a few stable configurations, e.g., cylindrical shapes, can be achieved.

To enrich the degree of multi-stability, we propose and study a new concept of morphing surface design, for which multi-stable beam-type metastructures (MBMs) are exploited to control deformations of the surface. MBMs are periodic structures that feature bi-stable snapping beams [31–36]. In terms of kinematics, multi-stable metastructures are capable of realizing a large translational motion via snap-through behavior, creating opportunities for motion-related applications. For instance, Bobbert *et al.* [37] designed deployable implants based on MBMs. Liu *et al.* [38] demonstrated the application of MBMs in motion systems. From these demonstrations it can be noted that the MBMs' stable configurations can be programmed by a proper arrangement of the unit cells. Subsequently, these arrangements can serve as the basis for designing morphing surfaces

with new features. To the best of our knowledge, the potential of using MBMs to control surface morphology has not been studied, and the associated design requirements are still unclear.

In this work, we investigate the possibility of using MBMs to impart curvature changes to a surface and study the accessible stable configurations. In Section 5.2, we present the design concept and discuss the stable curved configurations. Effects of geometric parameters on the curved states are studied both experimentally and numerically in Section 5.3. Moreover, an analytical model is proposed to examine the design criteria for ensuring stability of the structure. In Section 5.4, we extend the MBM design to a two-dimensional (2D) arrangement of unit cells and investigate the corresponding stable configurations. Conclusions are presented in Section 5.5.

5.2. DESIGN CONCEPT AND METHODS

5.2.1. STRUCTURAL DESIGN

The proposed design concept is based on multi-stable metastructures consisting of an array of bi-stable elements. As shown in Fig. 5.1(a), a pre-shaped curved beam (marked in orange) plays a pivotal role in ensuring bi-stable behavior. When an applied load exceeds a critical value, the pre-shaped beam can exhibit snap-through behavior and is capable of maintaining the deformed configuration (denoted by the dashed line) after removing the applied loads [39]. The beam's initial shape ($w(x)$) can be expressed as:

$$w(x) = \frac{h}{2}(1 - \cos(\pi \frac{2x}{L})), \tag{5.1}$$

where x represents a horizontal coordinate, and h, t, and L denote the beam height, thickness and length, respectively. Out-of-plane thickness is denoted as b. Next, the morphing surface is realized by connecting a compliant plate with a multi-stable metastructure. As illustrated in Fig. 5.1(b), the multi-stable metastructure here consists of three bi-stable elements that are arranged in one direction (1D), and a thin plate (marked in green) is connected to the multi-stable metastructure at the top. As depicted in this figure, L_t and m represent the top plate's effective span and thickness, respectively. The plate's curvature can be controlled by deforming a bi-stable element. For example, flipping the center bi-stable element can result in stable local curvature that can be retained without supplying actuation (see Fig. 5.1(b)). This deformed state with local curvature is referred to as stable curved configuration in the remainder of this chapter. Figure 5.1(b) also presents an experimental demonstration of the same design.

Next to the 1D arrangement, bi-stable elements can be arranged in two directions to design morphing surfaces. Figure 5.1(c) shows a multi-stable metastructure comprising two-dimensional (2D) arrangements of bi-stable elements. By connecting this metastructure with a compliant plate, it is possible to achieve stable curved configurations oriented in multiple directions, which results from a collective effect of the plate's compliance and the beams' bi-stability. As illustrated by the dot lines in Fig. 5.1(c), the curved configuration of the surface can be oriented in different directions. To explore this further, morphing surfaces based on 2D arrangements of bi-stable elements are designed in Section 5.4.

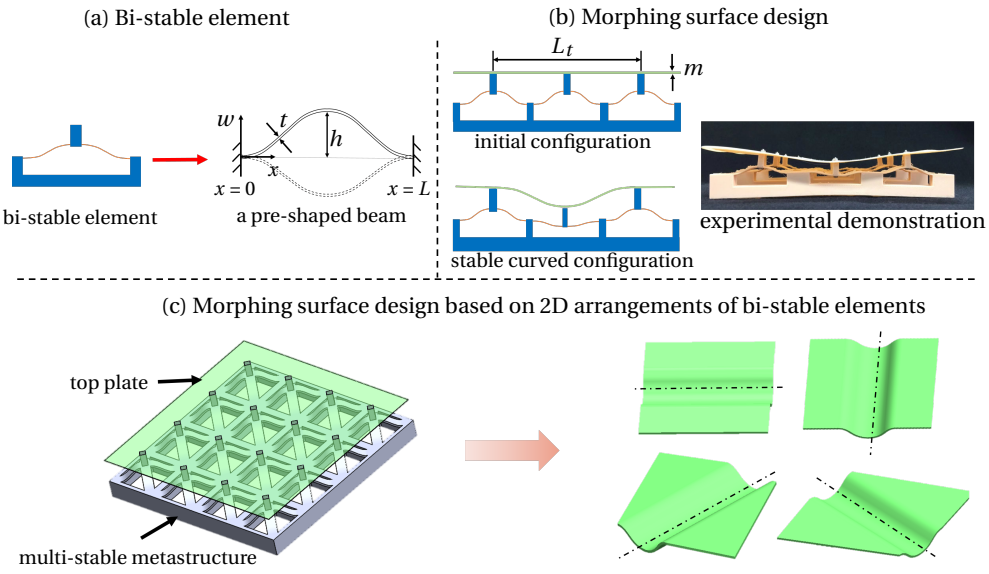

Figure 5.1: Schematic diagram of the proposed multi-stable surface design. (a) For each bi-stable element, a pre-shaped curved beam is able to snap into a second stable state (illustrated by curved dashed lines). (b) Morphing surface design. A thin compliant plate is connected with a multi-stable metastructure here composed of three bi-stable elements. When the center element snaps, the plate can stabilize at the curved configuration. Picture on the right shows an experimental demonstration of the stable curved configuration. (c) Morphing surface design based on 2D arrangements of bi-stable elements. When multiple bi-stable elements snap, the curved stable configurations can be oriented in different directions, as depicted by the dot lines.

5.2.2. FABRICATION AND EXPERIMENTS

Samples are fabricated based on a process of 3D printing and manual assembly. Specifically, the multi-stable metastructures are manufactured using a fused deposition printer (Prusa MK3s) with thermoplastic elastomers (TPU). In this work, the thin plates are printed with the same material. Then, the multi-stable metastructure and the thin plate are connected using screws. In order to determine material properties of TPU, standard tensile measurements are performed on multiple printed dumbbell specimens according to the ASTM D638-14 standard (see Appendix D.2).

Uniaxial loading tests are carried out to investigate the snap-through transition. A universal testing system (Zwick-005) is used to exert displacement-controlled loading. Rigid connectors are printed with stiff material (polylactide) for connecting the machine head with specimens (see Fig. 5.2(a)). During the loading, the displacement of the top is controlled with a speed of 10 mm/min, while the bottom of a sample is fully clamped. Moreover, the curvature of the deformed top plate is characterized experimentally. It can be noted that the plate's curvature at the deformed state is not uniform (see Fig. 5.1(b)). Here, an average curvature (denoted as κ) is defined. As shown in Fig. 5.2(a), two red markers with a distance of $L_t/2$ are added to the undeformed plate and we take photographs of the deformed curved configurations. Using image analysis software (ImageJ), lines perpendicular to the plate at the two markers are drawn, forming an angle β,

as highlighted in Fig. 5.2(a). Then, the average curvature κ is given by:

$$\kappa = \frac{2\beta}{L_t}. \tag{5.2}$$

5.2.3. NUMERICAL SIMULATIONS

Finite element models (FEM) based on ABAQUS/Standard (2017) are used to simulate snap-through transitions. The measured stress-strain curves of TPU are imported into the FEM, in which a hyper-elastic material model (Marlow potential [40]) is adopted. Eight-node solid elements (C3D8) are used and mesh convergence studies have been conducted to ensure accuracy. Boundary conditions are defined in such a way that the bottom of the structures is fully constrained and displacements are applied on the top. The reaction force is collected from the nodes with prescribed displacements. Note that the mean curvature κ is also quantified numerically.

5.3. STABLE CURVED CONFIGURATION

As discussed in the previous section, the structural snap-through transition involves deformations of both the metastructure and the top plate. In order to reveal the mechanical characteristics, in this section, snap-through transitions from the initial to the deformed curved configurations are investigated. Effects of geometric parameters are analyzed both experimentally and numerically. Moreover, to enable a deep understanding of the mechanical response, an analytical model is developed.

5.3.1. SNAP-THROUGH TRANSITIONS

As shown in Fig. 5.2(a), the snap-through transition from the initial flat to the deformed curved configuration is characterized. Figure 5.2(b) presents force-displacement curves for multiple structures with different geometric parameters, where the force (F) and displacement (d) are normalized by Ebt and h, respectively. E represents Young's modulus of the material. In the figure, it can be noted that the structure first exhibits a positive tangent stiffness before reaching the maximum force (denoted as F_{max}). Next, the structure exhibits a negative tangent stiffness during the continued loading until the minimum force (F_{min}) is reached. Finally, the structure snaps into the stable curved configuration with a positive tangent stiffness. It can be noted that during loading the center bi-stable elements snap while the adjacent beam elements (left and right beside the center element) are rotated, causing the force-displacement curves to be different from that of a single pre-shaped beam. To characterize the rotations of the adjacent elements, an analytical study has been performed in the following section. Furthermore, experimental and numerical results indicate that the snap-through response is dependent on both h/L and t/L, as a result of the beam's bi-stability. For instance, increasing h/L leads to an evident change of F_{max}, as presented in the figure. The resulting curvature κ is also influenced by t/L and h/L. In order to evaluate the effect of geometric parameters on the snap-through, a parametric study is performed.

Results for metastructures with different geometries are presented in Fig. 5.2(c)–(d), where κ and F_{max} are plotted as a function of h/L and t/L. In these two figures, it can be seen that κ is more sensitive to h/L than t/L such that increasing h/L leads to a distinct

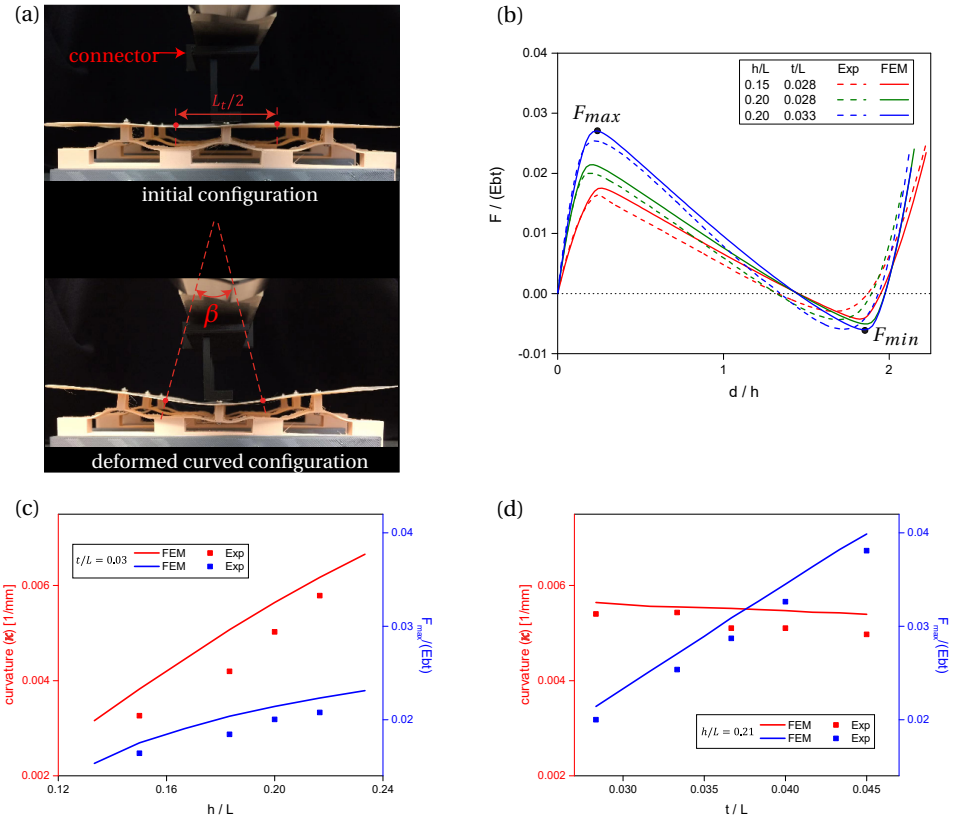

Figure 5.2: The snap-through transition from the initial to the curved configuration. (a) The displacement-controlled loading is applied at the center of top plate, resulting in the deformed curved configuration. (b) Measured and simulated force-displacement curves for different samples (L = 30 mm, m= 1.2mm). (c)–(d) The curvature κ of the stable configuration and the maximum force F_{max} are plotted as a function of h/L and t/L, respectively.

change of κ, while varying t/L has a minor effect on κ. This is because the displacement from the initial to curved configuration is mainly determined by h rather than t. In contrast, it can be noted that t/L is more influential for tuning F_{max} when compared to h/L (see Fig. 5.2(d)). This is due to the fact that as t increases, the beam's bending and axial stiffness will increase significantly, leading to a stiffer mechanical response. In case of varying h, the change of structural bending stiffness is not as large as that for t, resulting in a smaller change of F_{max}.

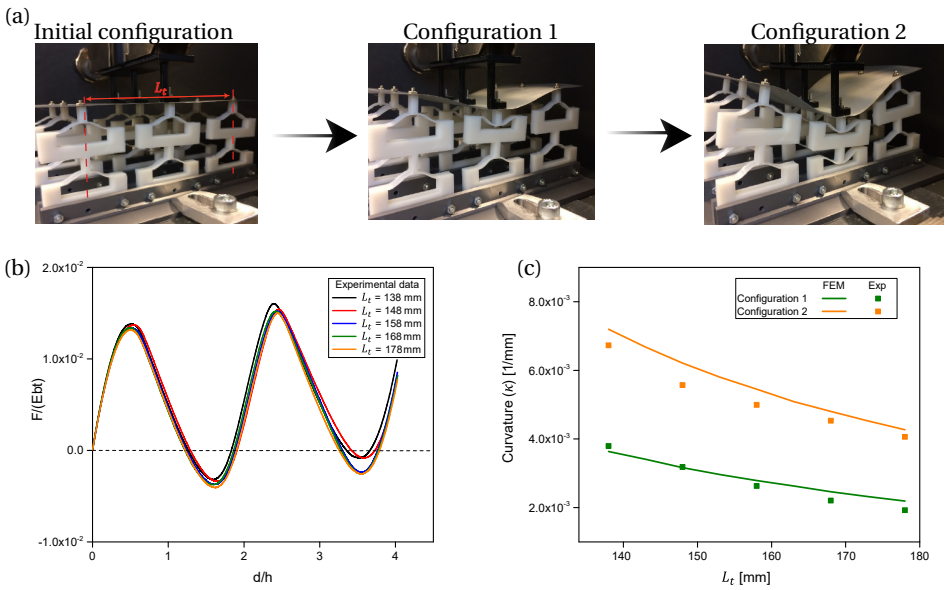

Figure 5.3: Curved stable configurations of a compliant plate connected with a two-layer multi-stable metastructure. (a) The two-layer structure is composed of multiple bi-stable elements (t = 0.85 mm, h = 6 mm, L = 40 mm). Snapshots of structural deformations during uniaxial loading are shown. The first and second deformed stable configuration are denoted as Configuration 1 and 2, respectively. (b) Experimentally measured force-displacement responses for different L_t. (c) The measured and simulated κ of Configuration 1 and 2 as a function of L_t.

Next, we study the curved configurations for a compliant plate connected with a two-layer multi-stable metastructure. Multiple bi-stable elements are arranged in horizontal and vertical directions, as shown in Fig. 5.3(a). During uniaxial loading, the structure is able to stabilize at each of two deformed configurations (denoted as Configuration 1 and 2), indicating if only one of the serial bi-stable elements is flipped, or both. Note that here the center element at the top layer first snap, as shown in Configuration 1. It is possible that the element at the bottom layer snap first. The snapping sequence (i.e., which layer first snaps) is mainly determined by inevitable manufacturing imperfections. Measured force-displacement curves are displayed in Fig. 5.3(b), where two sequential snap-through responses are captured. Moreover, different L_t are taken and results in Fig. 5.3(c) show the κ decreases when increasing L_t. Considering the effect of h as discussed before, it can be expected that the curvature κ can be effectively tuned via controlling h/L_t.

5.3.2. BI-STABILITY CRITERION

In the previous section, it is found that the snap-through response from the initial to the curved stable configuration can be tuned by varying the bi-stable elements' geometric parameters. Here, an analytical model is developed to study the relation between the geometric parameters and the structural stability.

MODEL DESCRIPTION

As shown in Fig. 5.4(a), the structure is composed of three bi-stable elements (left, center, and right) and a top plate. Note that the transition from the initially flat to the curved stable configuration involves: i) the snap-through of the center element; ii) rotations of the left and right (adjacent) bi-stable elements; iii) deformations of the top plate. Here, a simplified 2D structural geometry is proposed, as illustrated in Fig. 5.4(b). In this figure, the straight beam (marked in green) represents the top plate, and the center bi-stable element shown in Fig. 5.4(a) is simplified as a pre-shaped beam (highlighted in orange). To capture the rotational deformation of adjacent elements, we introduce two torsional springs with a rotational stiffness K_t on either end of the straight beam (see Fig. 5.4(b)). In doing so, the left and right bi-stable elements in Fig. 5.4(a) are simplified as two torsional springs in the model. Therefore, the geometry here consists of one straight beam, one pre-shaped beam at the center combined with a rigid connector (in black), and two torsional springs at two ends (see Fig. 5.4(b)) .

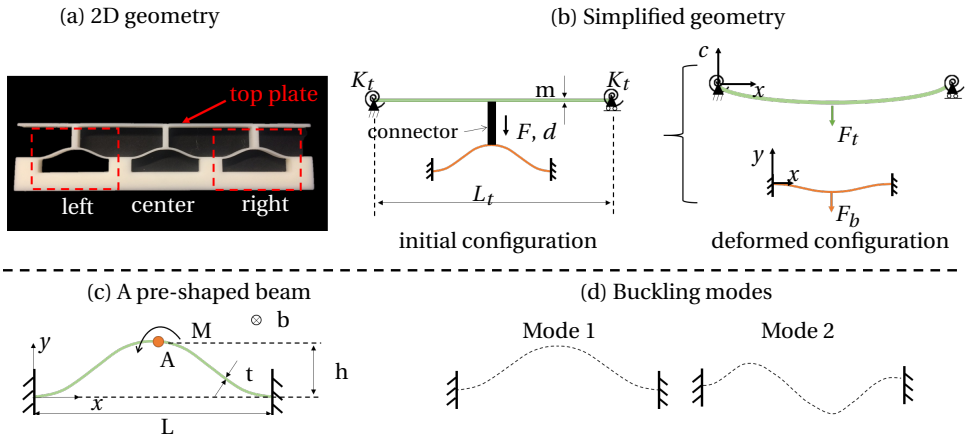

Figure 5.4: Modelling the snap-through transition. (a) A physical demonstration of a basic structural element. (b) Illustration of the simplified geometry. The top plate is assumed as a straight beam (in green) and the center bi-stable element is simplified as a pre-shaped beam (in orange). Left and right bi-stable elements are simplified as two torsional springs with a rotational stiffness (K_t). (c) The stiffness K_t arises from rotation of a pre-shaped beam subjected to a moment at Point A ($x = L/2$). (e) Illustration of the first two buckling modes for a clamped-clamped straight beam under axial compression.

As shown in Fig. 5.4(b), a vertical displacement (d) is prescribed at the rigid connector and the resulting force F is calculated. Note that both the straight and the pre-shaped beam experience the same vertical displacement (d) at the center. Thus, F can be decomposed into two parts, namely:

$$F = F_t + F_b, \tag{5.3}$$

where F_t is the resulting force related to the straight beam's deformation and F_b represents the force associated with the curved center beam's deflection (see Fig. 5.4(b)). Here, we solve F by calculating F_t and F_b separately. Note that notations (t, h, L, m, b and L_t) shown in Fig. 5.4 are consistent with those defined before.

a. Calculation of K_t

For deriving F_t, it is necessary to first determine the rotational stiffness K_t. As discussed before, K_t results from the rotations of adjacent elements (i.e., pre-shaped beams). That is, when a moment (M) is applied at the center of a pre-shaped beam (see Fig. 5.4(c)), K_t can be obtained by calculating the slope of $M-\theta$ curve, where θ is the resulting rotation at Point A in the figure. Previous studies have shown that for a pre-shaped beam, employing buckling modes as bases can give a good approximation of the snap-through behavior [33, 39]. Here, the $M-\theta$ relation is derived based on the principle of mode superposition and minimum total potential energy. According to Euler-Bernoulli theory [41], buckling modes of a clamped-clamped beam under axial compression can be expressed as:

$$y_i = 1-\cos(N_i\frac{x}{L}) \text{ and } N_i=(i+1)\pi, \text{ when } i=1,3,5... \tag{5.4}$$

$$y_i = 1-2\frac{x}{L}-\cos(N_i\frac{x}{L})+\frac{2}{N_i}\sin(N_i\frac{x}{L}) \text{ and } N_i=2.86\pi,4.92\pi,6.94\pi... \text{ when } i=2,4,6... \tag{5.5}$$

where y_i represents i-th buckling mode in the x–y coordinate system shown in Fig. 5.4(c). The first two mode shapes are illustrated in Fig. 5.4(d). Using the buckling modes, the beam's deformed shape (y) under a moment can be defined as:

$$y=\sum_{i\in\{1,2,4,6,8\}} A_i y_i \text{ and } y_0=\frac{h}{2}y_1, \tag{5.6}$$

where y_0 represents the initial curved shape. A row vector is defined as $\mathbf{A}=\{A_1,A_2,A_4,A_6,A_8\}$, which includes the unknown coefficients that need to be solved. Next, governing equations can be obtained by taking the derivative of total potential energy with respect to each component in $\mathbf{A}$. We solve the resulting system of equations numerically by scanning M in a certain range, by which $\mathbf{A}$ and the $M-\theta$ curves can be obtained (refer to Appendix D.1.1).

b. Derivation of F_t

With the derived K_t, we can calculate the straight beam's deformation and the associated force F_t. For a flat beam, when the force F_t is applied at the center (i.e., $x=L_t/2$), as presented in Fig. 5.4(b), the resulting displacement can be expressed as:

$$c(x)=\frac{S_1}{6}x^3+\frac{S_2}{2}x^2+S_3x+S_4 \text{ for } x\in[0,\frac{L_t}{2}], \tag{5.7}$$

where $c(x)$ is a Cartesian coordinate system depicted in Fig. 5.4(b), and S_1,S_2,S_3,S_4 are unknown coefficients. By substituting boundary conditions, relation between F_t and d is derived as:

$$d=c(\frac{L_t}{2})=\frac{-F_t}{12EI_t}(\frac{L_t}{2})^3+\frac{F_tL_t^2}{32EI_t(\frac{L_t}{2}+\frac{EI_t}{K_t})}(\frac{L_t}{2})^2+\frac{F_tL_t^2}{8K_tL_t+16EI_t}(\frac{L_t}{2}), \tag{5.8}$$

where EI_t is the bending stiffness of the straight beam. The detailed derivation for Eqn. (5.8) can be found in Appendix D.1.2.

c. Derivation of F_b

Next, the force F_b related to the beam's snap-through is calculated. For the pre-shaped beam subjected to a vertical force (F_b) in the center, as demonstrated in Fig. 5.4(b), the corresponding load-displacement response can be derived based on the mode superposition principle, similar to the procedure we discussed before for deriving the rotational stiffness. Here, the first nine symmetric buckling modes are employed as basis and the deformed shape is expressed as:

$$y = \sum_{i\in\{1,3,5,7,9\}} B_i y_i, \tag{5.9}$$

where $\mathbf{B} = \{B_1, B_3, B_5, B_7, B_9\}$ represents unknown coefficients and y_i is the buckling mode (see Eqn. (5.4)). The total potential energy consists of the strain energy (U_s) as a function of $\mathbf{B}$ and the potential energy (U_p) due to the load F_b, namely:

$$U = U_s(\mathbf{B}) + U_p \quad \text{and} \quad U_p = -F_b d. \tag{5.10}$$

Based on the minimum total potential energy principle, a system of five equations is obtained, which can be solved numerically (refer to Appendix C.1).

MODEL RESULTS

Following the discussed procedure, we first look into K_t as predicted by the analytical model. In particular, Fig. 5.5(a) shows M-θ curves for beams with different geometric parameters, where K_t is the tangent slope of each curve. From the figure it can be noted that a good agreement between the analytical and numerical result is realized, verifying the proposed model. In addition, it can be seen that K_t is dependent on both h/L and t/L. Using the analytical model, the influence of h and t on K_t are studied, as plotted in Fig. 5.5(b). Note that K_t in the figure is obtained by computing the tangent slope to the $M-\theta$ curve at rotation θ= 0.2. From the figure, it can be seen that K_t is sensitive to the variation of t/L, while varying h/L has a smaller effect on K_t as opposed to t/L. This is mainly due to the fact that varying t has a significant influence on the structural bending stiffness as well as the bending energy during deformations. Therefore, the rotational stiffness of a pre-shaped beam can be effectively tuned by changing the thickness t.

Snap-through transitions predicted by the analytical model are presented in Fig. 5.5(c). To validate the model, results from finite element simulations are added, as shown in the figure. It can be seen that the model is able to predict the snap-through response properly. Both analytical and numerical results confirm that the snap-through characteristics can be tuned by changing the geometric parameters (e.g., h/L and t/L). Moreover, using this analytical model, we study the bi-stability criterion that enables the top plate to maintain the curved configurations. As shown in Fig. 5.6(a) and (b), phase diagrams allowing for the stable curved configuration are defined on the basis of the normalized quantities (h/L and t/L). In particular, these figures display the variation of $|F_{min}|$ (absolute value) and F_{max} with respect to h/L and t/L. The colored region indicates configurations at which the top plate is able to stabilize ($F_{min} < 0$), while the grey area indicates

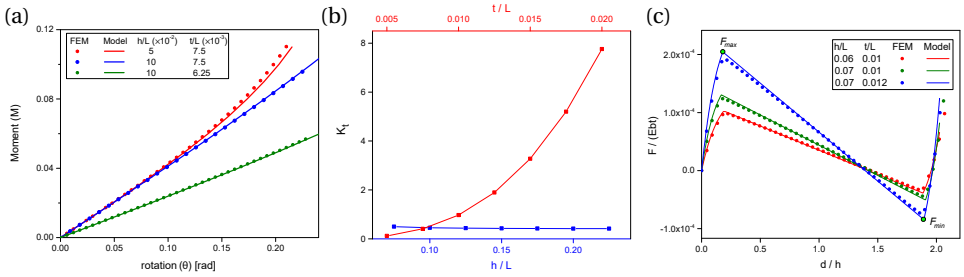

Figure 5.5: The predicted K_t and force-displacement responses from the analytical model. (a) The moment versus rotation ($M-\theta$) for a pre-shaped beam ($b=4$ mm) when subjected to an applied moment. The torsional stiffness K_t can be derived by calculating the tangent slope of $M(\theta)$, as denoted in this figure. (b) Effects of h/L and t/L on K_t are investigated analytically. Here, t/L is taken as 7.5×10^{-3} when varying h/L, while in case of changing t/L, h/L is kept unchanged as 6.25×10^{-2}. (c) A comparison of snap-through responses predicted by the analytical model and FEM.

that the plate recovers to the initial configuration after removing the loads (i.e. mono-stable behavior). It can be interpreted that when h/L of bi-stable elements is given, the corresponding t/L needs to be selected within a certain range in order to realize the stable curved configuration. When t/L is smaller than a certain value (0.012 as shown in Fig. 5.6(a)), mono-stable behavior occurs. This is because a small t/L cannot provide sufficient F_{min} for the top plate to maintain the deformed state. In addition, it can be observed that F_{max} and $|F_{min}|$ exhibit different sensitivities for parameter variations. To maximize F_{max}, large h/L and t/L are required. In case of $|F_{min}|$, it shows a nonlinear relation with respect to t/L. That is, further increasing t/L will lead to a decrease of $|F_{min}|$, resulting in mono-stable behavior. Using the proposed model, we can rapidly identify the region for realizing curved stable configurations and select proper geometric parameters.

5.4. 2D ARRANGEMENTS OF BI-STABLE UNITS

As discussed in Section 5.2, for the top plate, 2D arrangements of bi-stable units can lead to multiple curved configurations oriented in different directions. This section presents the multi-stable metastructures with 2D arrangements of bi-stable elements and studies the deformed configurations for the top plate. Here, multi-stable metastructures are designed by considering an in-plane periodic arrangement of bi-stable units. The unit based on the snapping beam is illustrated in Fig. 5.7(a), where the picture on the right shows an experimental demonstration of a multi-stable metastructure consisting of 4×4 bi-stable units. A thin plate is then connected with the multi-stable metastructure at the top.

Through controlling snap-through deformations locally, the structure is capable of achieving a series of deformed stable configurations. Fig. 5.7(b) displays a few stable configurations of the top plate, where the dashed red lines highlight bi-stable units that have snapped into the second stable state. From the figure, it can be noted that the top plate can not only exhibit curved stable states in x and y direction, but also is able

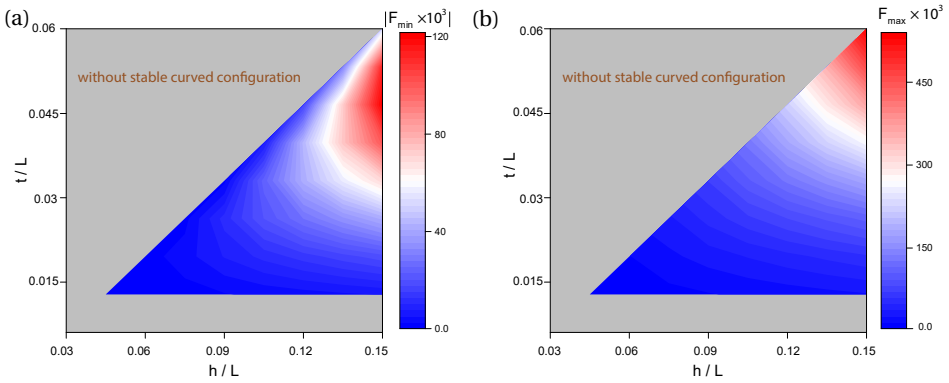

Figure 5.6: Stability criterion for the stable curved configuration. (a)–(b) The variation of F_{max} and $|F_{min}|$ as a function of t/L and h/L. The proper design space for realizing the stable curved configuration is denoted in color, while the grey region represents mono-stable behavior. The latter indicates the structure cannot retain the stable curved configuration.

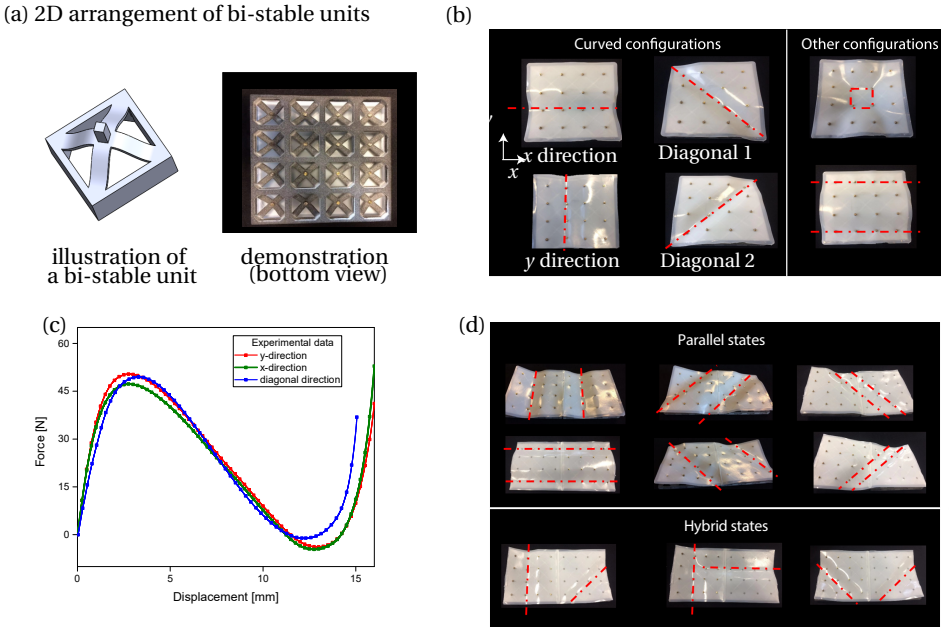

Figure 5.7: Multi-stable surface designs based on 2D arrangements of bi-stable units. (a) A bi-stable unit based on the snapping beam is illustrated. On the right, an experimental demonstration of the metastructure is displayed. (b) The representative deformed stable configurations of the top plate. (c) Measured force-displacement curves corresponding to transitions from the initial to x direction, y direction, and Diagonal 1 configuration. (d) By combining more bi-stable elements, multiple stable deformed configurations, including the parallel and hybrid states, can be realized.

to realize stable deformations in two diagonal orientations (denoted as Diagonal 1 and 2 in Fig. 5.7(b)). The multiple curved configurations in different directions are mainly caused by the in-plane arrangement of bi-stable elements as well as the compliance of the plate. Here, we characterize the snap-through transitions from the initial to x direction, y direction, and Diagonal 1 configuration, respectively. For each configuration, a displacement-controlled loading is applied to the units highlighted by the dashed red lines and the total force is measured. Results in Fig. 5.7(c) indicate that the three snap-through transitions exhibit similar force-displacement characteristics. This is due to the fact that the snap-through response of each case mainly results from deformations of the top plate and four snapped bi-stable units. Thus, critical loads are almost the same for all three cases. Moreover, it should be noted that other stable configurations can also be realized. For instance, deforming four bi-stable elements in the middle can result in a local curvature for the plate, as shown in Fig. 5.7(b).

By arranging more bi-stable units, more stable configurations can be realized. Here, we build a multi-stable metastructure with an arrangement of 8×4 bi-stable elements and connect it with a thin plate. As demonstrated in Fig. 5.7(d), various morphological states can be achieved. The deformed configurations can be classified into two representative groups: parallel and hybrid states. That is, two parallel curved configurations can be achieved in x, y, and diagonal directions, respectively (see Fig. 5.7(d)). The hybrid stable states in the figure demonstrate that it is possible to combine two curved configurations with different directions to generate hybrid deformed states, making surface morphology distinct from the parallel states.

However, it should be noted that arranging a large number of bi-stable units may limit further extension of the parallel and hybrid states. This is because when more units are arranged, the surface's in-plane motions will be constrained, generating large resistant forces against the stable deformed configurations. In order to address this, surfaces consisting of meso-structures can be employed for mitigating effects of the in-plane deformations. Previous studies have demonstrated that introducing mesostructures into a plate can be an effective way to design highly flexible surfaces with low in-plane stiffness [42, 43]. In doing so, it is possible to extend the presented stable configurations (e.g., parallel and hybrid states) to a large extent. Here, we design a mesostructure-based surface comprising curved leaf springs, as shown in Fig. 5.8(a). The planar structure is then connected to a multi-stable metastructure consisting of 16×8 bi-stable elements. By controlling multiple units' snap-through deformations, a series of surface morphology can be obtained. Specifically, parallel states in y direction are presented in Fig. 5.8(b), which verifies the feasibility of extending the stable states to a large extent. Moreover, Fig. 5.8(c) shows that the curved stable configurations can be effectively aligned in different directions, as denoted by the red dashed lines. To highlight this, a rubber sheet (the red surface in Fig. 5.8(c)) is placed on top of the planar structure, which clearly shows the deformed configurations that mimic corrugated patterns. It can be expected that based on the proposed design, the stable patterns can be further extended by adding more bi-stable elements. The curvature change can be utilized to realize tunable functionalities, such as adaptive deformable mirrors.

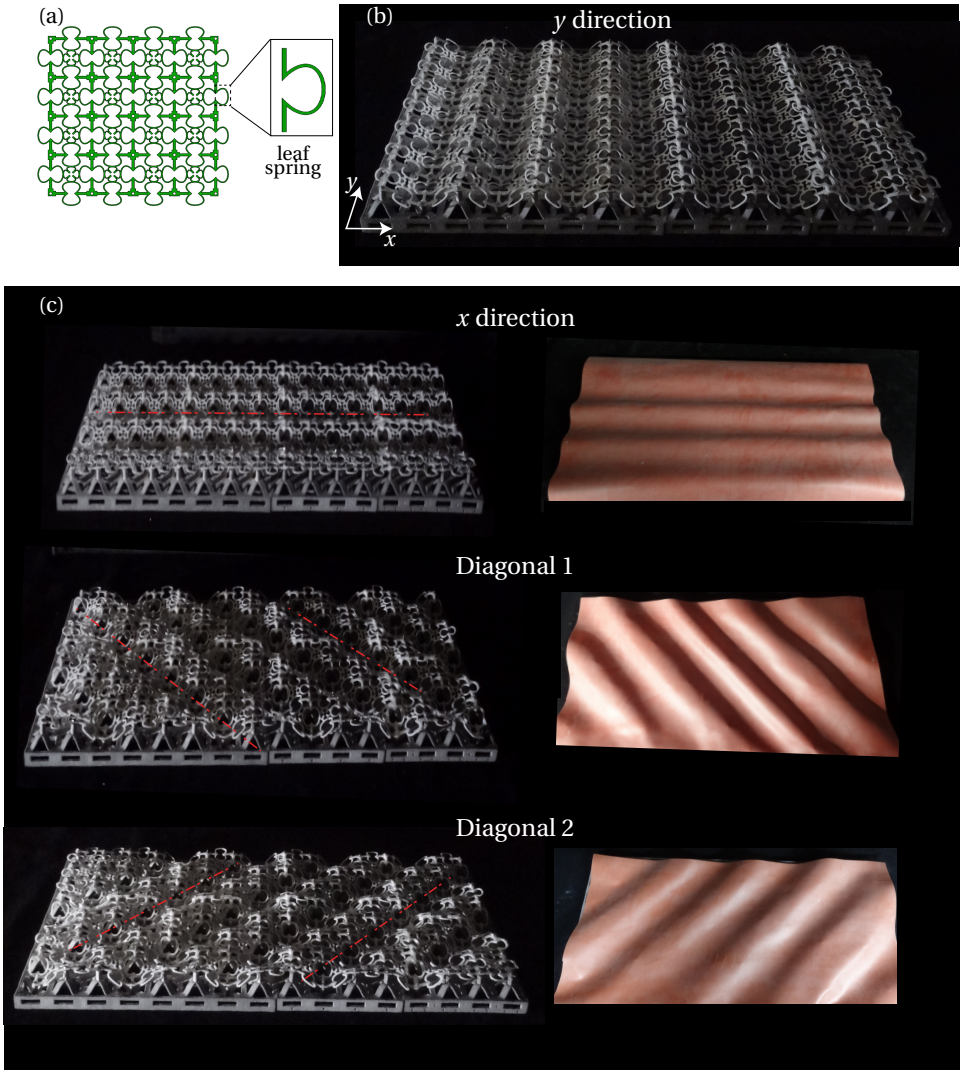

Figure 5.8: Programming of curved stable configurations via arranging a large number of bi-stable units. (a) A mesostructure-surface design is based on curved leaf springs. The illustrated curved leaf spring on the right can exhibit relatively large in-plane compliance. (b) An experimental demonstration of multiple parallel stable configurations enabled by a multi-stable metastructure (16×8 units) and the mesostructure-based surface design. (c) The parallel states can be oriented in different directions to realize corrugated patterns, as highlighted by the red dashed lines.

5.5. CONCLUSIONS

This work presents a design of multi-stable surfaces based on beam-type metastructures. The presented design allows for a series of curved configurations in multiple directions, enabled by a collective effect of the beams' bi-stability and the surface's compliance. The snap-through deformations of the structures are investigated and effects of geometric parameters are analyzed. Results show that h/L of the bi-stable element is important for tuning the stable curvature, while t/L plays a paramount role in adjusting the snap-through response. Moreover, an analytical model that can accurately predict the snap-through transition is proposed. Using the model, the design criterion for realizing stable configurations is studied as a function of h/L and t/L. It is found that in order to achieve a stable configuration, h/L should be large, while t/L needs to be constrained within a certain range. This criterion can serve as a guideline for tuning the snap-through response and manipulating stability of the deformed states. Moreover, we have applied this design concept to 2D arrangements of bi-stable units and have demonstrated the resulting stable configurations (e.g., parallel and hybrid states). In order to extend the deformed configurations to a large extent, a meso-structure based surface is designed. It is demonstrated that the stable configurations can be extended further with the meso-structure based surfaces, enabling corrugations in different directions. With proper arrangements of bi-stable elements, the proposed design can be explored to develop functional surfaces with tunable properties.

REFERENCES

[1] S. Barbarino, O. Bilgen, R. M. Ajaj, M. I. Friswell, and D. J. Inman, *A review of morphing aircraft,* Journal of intelligent material systems and structures **22**, 823 (2011).

[2] C. G. Diaconu, P. M. Weaver, and F. Mattioni, *Concepts for morphing airfoil sections using bi-stable laminated composite structures,* Thin-Walled Structures **46**, 689 (2008).

[3] G. Arena, R. MJ Groh, A. Brinkmeyer, R. Theunissen, P. M. Weaver, and A. Pirrera, *Adaptive compliant structures for flow regulation,* Proceedings of the Royal Society A: Mathematical, Physical and Engineering Sciences **473**, 20170334 (2017).

[4] S. Daynes, P. Weaver, and J. Trevarthen, *A morphing composite air inlet with multiple stable shapes,* Journal of intelligent material systems and structures **22**, 961 (2011).

[5] J. Wu, J. Li, and S. Yan, *Design of deployable bistable structures for morphing skin and its structural optimization,* Engineering Optimization **46**, 745 (2014).

[6] X. Lachenal, S. Daynes, and P. M. Weaver, *Review of morphing concepts and materials for wind turbine blade applications,* Wind energy **16**, 283 (2013).

[7] Y. Lu, H. Yue, Z. Deng, and H. Tzou, *Distributed sensing signal analysis of deformable plate/membrane mirrors,* Mechanical Systems and Signal Processing **96**, 393 (2017).

[8] M. Hendrikx, J. ter Schiphorst, E. P. van Heeswijk, G. Koçer, C. Knie, D. Bléger, S. Hecht, P. Jonkheijm, D. J. Broer, and A. P. Schenning, *Re-and preconfigurable multistable visible light responsive surface topographies,* Small **14**, 1803274 (2018).

[9] Y. Shen, Q. Zou, B. Wan, X. She, R. You, Y. Luo, and C. Jin, *High-contrast dynamic reflecting system based on pneumatic micro/nanoscale surface morphing,* ACS Applied Materials & Interfaces (2020).

[10] O. Peretz, A. K. Mishra, R. F. Shepherd, and A. D. Gat, *Underactuated fluidic control of a continuous multistable membrane,* Proceedings of the National Academy of Sciences **117**, 5217 (2020).

[11] S. Jiao and M. Liu, *Snap-through in graphene nanochannels: With application to fluidic control,* ACS Applied Materials & Interfaces (2020).

[12] Y. Park, G. Vella, and K. J. Loh, *Bio-inspired active skins for surface morphing,* Scientific reports **9**, 1 (2019).

[13] Y. Park and K. J. Loh, *Surface morphing of geometrically patterned active skins,* MRS Advances **5**, 743 (2020).

[14] D. P. Holmes and A. J. Crosby, *Snapping surfaces,* Advanced Materials **19**, 3589 (2007).

[15] N. Hu and R. Burgueño, *Buckling-induced smart applications: recent advances and trends,* Smart Materials and Structures **24**, 063001 (2015).

[16] D. P. Holmes, *Elasticity and stability of shape-shifting structures,* Current opinion in colloid & interface science **40**, 118 (2019).

[17] S. Guest and S. Pellegrino, *Analytical models for bistable cylindrical shells,* Proceedings of the Royal Society A: Mathematical, Physical and Engineering Sciences **462**, 839 (2006).

[18] A. F. Arrieta, I. K. Kuder, T. Waeber, and P. Ermanni, *Variable stiffness characteristics of embeddable multi-stable composites,* Composites Science and Technology **97**, 12 (2014).

[19] A. Madhukar, D. Perlitz, M. Grigola, D. Gai, and K. J. Hsia, *Bistable characteristics of thick-walled axisymmetric domes,* International Journal of Solids and Structures **51**, 2590 (2014).

[20] Z. Chen, Q. Guo, C. Majidi, W. Chen, D. J. Srolovitz, and M. P. Haataja, *Nonlinear geometric effects in mechanical bistable morphing structures,* Physical review letters **109**, 114302 (2012).

[21] M. Alturki and R. Burgueño, *Response characterization of multistable shallow domes with cosine-curved profile,* Thin-Walled Structures **140**, 74 (2019).

[22] A. Brinkmeyer, M. Santer, A. Pirrera, and P. Weaver, *Pseudo-bistable self-actuated domes for morphing applications,* International Journal of Solids and Structures **49**, 1077 (2012).

[23] M. Taffetani, X. Jiang, D. P. Holmes, and D. Vella, *Static bistability of spherical caps,* Proceedings of the Royal Society A: Mathematical, Physical and Engineering Sciences **474**, 20170910 (2018).

[24] E. Loukaides and K. Seffen, *Multistable grid and honeycomb shells,* International Journal of Solids and Structures **59**, 46 (2015).

[25] Y. Cui and M. Santer, *Highly multistable composite surfaces,* Composite Structures **124**, 44 (2015).

[26] F. Dai, H. Li, and S. Du, *A multi-stable wavy skin based on bi-stable laminates,* Composites Part A: Applied Science and Manufacturing **45**, 102 (2013).

[27] F. Dai, H. Li, and S. Du, *Design and analysis of a tri-stable structure based on bi-stable laminates,* Composites Part A: Applied Science and Manufacturing **43**, 1497 (2012).

[28] Y. Cui and M. Santer, *Characterisation of tessellated bistable composite laminates,* Composite Structures **137**, 93 (2016).

[29] A. Norman, K. Seffen, and S. Guest, *Multistable corrugated shells,* Proceedings of the Royal Society A: Mathematical, Physical and Engineering Sciences **464**, 1653 (2008).

[30] G. Risso, M. Sakovsky, and P. Ermanni, *Highly multi-stable frp grids for shape adaptation,* in *AIAA Scitech 2021 Forum* (2021) p. 1493.

[31] S. Shan, S. H. Kang, J. R. Raney, P. Wang, L. Fang, F. Candido, J. A. Lewis, and K. Bertoldi, *Multistable architected materials for trapping elastic strain energy,* Advanced Materials **27**, 4296 (2015).

[32] Y. Zhang, Q. Wang, M. Tichem, and F. van Keulen, *Design and characterization of multi-stable mechanical metastructures with level and tilted stable configurations,* Extreme Mechanics Letters **34**, 100593 (2020).

[33] K. Che, C. Yuan, J. Wu, H. Jerry Qi, and J. Meaud, *Three-dimensional-printed multistable mechanical metamaterials with a deterministic deformation sequence,* Journal of Applied Mechanics **84** (2017).

[34] S. M. Montgomery, X. Kuang, C. D. Armstrong, and H. J. Qi, *Recent advances in additive manufacturing of active mechanical metamaterials,* Current Opinion in Solid State and Materials Science **24**, 100869 (2020).

[35] T. Frenzel, C. Findeisen, M. Kadic, P. Gumbsch, and M. Wegener, *Tailored buckling microlattices as reusable light-weight shock absorbers,* Advanced Materials **28**, 5865 (2016).

[36] D. Restrepo, N. D. Mankame, and P. D. Zavattieri, *Phase transforming cellular materials,* Extreme Mechanics Letters **4**, 52 (2015).

[37] F. Bobbert, S. Janbaz, T. van Manen, Y. Li, and A. Zadpoor, *Russian doll deployable meta-implants: Fusion of kirigami, origami, and multi-stability,* Materials & Design **191**, 108624 (2020).

[38] X. Liu, F. Lamarque, E. Doré, and P. Pouille, *Multistable wireless micro-actuator based on antagonistic pre-shaped double beams,* Smart Materials and Structures **24**, 075028 (2015).

[39] J. Qiu, J. H. Lang, and A. H. Slocum, *A curved-beam bistable mechanism,* Journal of microelectromechanical systems **13**, 137 (2004).

[40] R. Marlow, *A general first-invariant hyperelastic constitutive model,* Constitutive Models for Rubber , 157 (2003).

[41] S. P. Timoshenko and J. M. Gere, *Theory of elastic stability* (Courier Corporation, 2009).

[42] T. van Manen, S. Janbaz, M. Ganjian, and A. A. Zadpoor, *Kirigami-enabled self-folding origami,* Materials Today **32**, 59 (2020).

[43] M. J. Mirzaali, A. Ghorbani, K. Nakatani, M. Nouri-Goushki, N. Tümer, S. J. P. Callens, S. Janbaz, A. Accardo, J. Bico, M. Habibi, and A. A. Zadpoor, *Curvature induced by deflection in thick meta-plates,* Advanced Materials , 2008082 (2021).

6

Conclusions and Recommendations

In this chapter, conclusions on the research presented in previous chapters are provided and recommendations for further study are briefly discussed.

6.1. CONCLUSIONS

This dissertation aims to provide strategies for designing multi-stable metastructures with novel functionalities as well as structural kinematics, and to give insights into the non-linear mechanics of the proposed metastructure design. In the previous four chapters, progress has been made to achieve the principal research goals that are defined in Chapter 1:

1. *Design and model multi-stable metastructures that exhibit both translational and rotational stable states.*

Chapter 2 addresses this by introducing the concept of rotational compliance into the metastructure design. It is found that the rotational compliance that is controlled by the beam's geometric parameters (height h, thickness t, and span L) play a crucial role in determining the rotational stability. To capture the translational and rotational transition, an analytical model has been developed. This model can predict the force-displacement responses properly. Using the proposed model, we can rapidly explore the design space for realizing rotational states and for tuning critical snapping forces, as a function of h/L and t/L.

As a result, the accessible multi-stability is expanded into translational and rotational stable configurations. The stability arises from the arrangements of a number of unit cells exhibiting bi-stability and certain rotational compliance. Moreover, it is shown that rotational transition requires a smaller actuation force and snaps to a deformed state with a lower strain energy as compared to its translational counterpart. This indicates that the rotational states are more sensitive to external disturbances than the translational states. On the other hand, the inherent translations are not affected by the rotations, which ensures the metastructure is able to switch to either translational or rotational stable configurations. As such, the allowable states of multi-stable structrues are further enriched for shape reconfiguration, making it possible to achieve more complex deformations.

The concept of rotational compliance is not only suitable for two-dimensional (2D) structures as studied above, but also applicable to three-dimensional (3D) structural designs. More importantly, from the perspective of shape-shifting applications, developing 3D reconfigurable structures is more attractive. In Chapter 3, we present the extension to 3D metastructures which allows for both translational and rotational states. Distinct from the 2D design, the proposed 3D structures are capable of rendering a series of rotational states in different directions, depending on the unit cell arrangements. The parallel and serial arrangements demonstrated in this chapter clearly reveal the relation between the patterning of unit cells and the allowable rotations. That is, for the in-plane assembly, it is the symmetry axes that determine the rotational directions, while the serial arrangement can lead to a number of stable states (i.e., 2^n configurations and n stands for the number of layers in series). Together with investigations in previous chapters, it can be concluded that the proposed concept of incorporating rotations into multi-stable structures can open up new pathways to enrich metastructures' kinematics and reconfigurability for the application to deployable structures.

The following research objective of this dissertation is focused on functionalities of the multi-stable metastructures, where the studied kinematics plays an important role in realizing energy dissipation and morphing surface.

2. *Develop designs to improve metastructures' energy dissipation.*

To address this, multi-stable metastructures with lattice reinforcements and box-shaped cross sections have been proposed and studied in Chapter 4. It is found that mechanical properties and energy dissipation of multi-stable metastructures can be greatly improved by enlarging the structural bending stiffness. In this process, the overall thickness plays an important role in tuning the stiffness. However, the tuning of thickness should be limited within a certain range to avoid local buckling, as shown in this chapter. Moreover, quasi-static tests show that, as compared to solid-beam based metastructure designs, the studied structures give rise to a stiffer mechanical response as well as an evident negative stiffness, resulting in a large benefit in terms of critical forces and energy dissipation. It has been found that these metastructures are capable of realizing a larger hysteresis loop and can further reduce peak acceleration during impact loading when compared to previous structures with the same mass. In addition, the design approach provided in this chapter is not limited to beam-type geometries and the improvement of mechanical properties can also be achieved in other type of structural elements, such as shells. To demonstrate this, we have successfully developed and characterized a type of hierarchical shells with embedded lattice cores, strengthening the versatility of the proposed approach.

Apart from energy absorption, another important functionality of multi-stable metastructures is the shape reconfiguration. In this thesis, by utilizing multi-stable metastructure, we have proposed a new concept of morphing surface design, which is related to the third research objective:

3. *Investigate functionalities of multi-stable metastructures in morphing surface.*

In Chapter 5, we have explored the accessible stable states of morphing surface design based on multi-stable metastructures. It has been shown that the multi-stable surface can be designed by connecting a compliant plate to metastructures consisting of 1D or 2D arrangements of bi-stable elements. For the sake of ensuring stable configurations, it is important to search for proper geometric parameters. In this chapter, design criteria are defined via an analytical formulation. Results suggest that bi-stable elements' height and thickness are crucial for tuning the structure's nonlinear response, and thus the snap-through properties can be further tailored based on the presented design map given by the model. In addition, we present metastructures with 2D arrangements of bi-stable elements. The resulting morphing surface design allows to realize curved stable states in multiple directions, depending on the alignment of bi-stable elements. Various stable configurations can be realized and it is demonstrated that by adopting surfaces consisting of mesostructures, it is possible to extend the stable configurations to a large extent. Adding more bi-stable elements enables to duplicate these curved states in a thin plate, which can achieve a wide range of deformed configurations (e.g., corrugated patterns).

6.2. RECOMMENDATIONS

Although this work presents several design strategies and the in-depth analysis for multi-stable beam-type metastructures, there are still many interesting aspects that are of importance to be explored in future. The following recommendations list some potential interesting topics relevant to the multi-stable metastructures in this work.

- In this dissertation, we mainly focus on the mechanics of rotational snap-through transition. The proposed rotational property as studied may prompt a variety of novel motion-related functional structural designs, which have not been explored here. For example, it is of interest to utilize the rotational elements as building blocks to design three-dimensional deployable structures. Moreover, recent research has proposed a concept of exploiting the unequal energy barrier between the initial and deformed state to achieve a rapid structure deployment [1]. This methodology is promising in the sense that it can avoid the redundant use of actuators and only requires an instant actuation. However, the current state-of-art is limited to translational motion, and it would be interesting to combine rotations to realize such structural deployments.

- From the kinematics point of view, the allowable motions of the multi-stable metastructures are still limited even though we have extended the degrees of freedom into translations and rotations. For designing shape-morphing structures or motion related actuators, it is attractive to realize a monolithic structural design with many degrees of freedom [2–4]. An interesting approach would be to implement stable twisting behavior into metastructures, so that translation, rotation and twisting can be obtained within one structure. This design may feature a few important advantages, such as simplification of design process, offering multiple motions, and no need for continued energy, which will pave the way for developing multi-stable stages with multi-degree-of-freedom.

- In addition, to achieve the snap-through transitions between multiple stable configurations, we employ mechanical loading to achieve configuration change. The implementation of actuation within the metastructures, which will make it easier to realize shape reconfiguration, is not taken into account in this work. Recent development of additive manufacturing enables to fabricate stimuli-responsive materials, and this process, which is also named as 4D printing, can create structures that allow for large deformation based on environmental change, such as temperature and light [5]. By leveraging 4D printing techniques, it is very interesting to develop active multi-stable metastructures that are able to switch to another shape based on the environmental stimuli, which can facilitate the process of design and achieve remote control for reconfiguration.

- The present work has mainly concentrated on macroscopic structures, and studies on micro-scale metastructures are not performed. Manufacturing such reconfigurable micro-structures is not as easy as for the millimeter range. Currently, research on utilizing pre-stretched system to generate 3D multi-stable microstruc-

tures has been an active focus [6, 7]. The pre-stretched system is normally composed of prestrained elastomer substrates and carefully designed 2D precursors. By controlling sequence of the strain release, distinct configurations can be realized within one structure. However, the accessible topology of such 3D mesostructure is still limited and it would be interesting to develop relevant mechanics models to predict post-buckling deformations of the multi-stable mesostructures.

REFERENCES

[1] A. Zareei, B. Deng, and K. Bertoldi, *Harnessing transition waves to realize deployable structures,* Proceedings of the National Academy of Sciences **117**, 4015 (2020).

[2] B. Haghpanah, L. Salari-Sharif, P. Pourrajab, J. Hopkins, and L. Valdevit, *Multistable shape-reconfigurable architected materials,* Advanced Materials **28**, 7915 (2016).

[3] H. Yasuda, T. Tachi, M. Lee, and J. Yang, *Origami-based tunable truss structures for non-volatile mechanical memory operation,* Nature communications **8**, 1 (2017).

[4] C. Jianguo, D. Xiaowei, Z. Ya, F. Jian, and T. Yongming, *Bistable behavior of the cylindrical origami structure with kresling pattern,* Journal of Mechanical Design **137** (2015).

[5] S. M. Montgomery, X. Kuang, C. D. Armstrong, and H. J. Qi, *Recent advances in additive manufacturing of active mechanical metamaterials,* Current Opinion in Solid State and Materials Science **24**, 100869 (2020).

[6] H. Fu, K. Nan, W. Bai, W. Huang, K. Bai, L. Lu, C. Zhou, Y. Liu, F. Liu, J. Wang, *et al.*, *Morphable 3d mesostructures and microelectronic devices by multistable buckling mechanics,* Nature materials **17**, 268 (2018).

[7] K. Bai, X. Cheng, Z. Xue, H. Song, L. Sang, F. Zhang, F. Liu, X. Luo, W. Huang, Y. Huang, *et al.*, *Geometrically reconfigurable 3d mesostructures and electromagnetic devices through a rational bottom-up design strategy,* Science advances **6**, eabb7417 (2020).

A

MODELING ROTATIONAL SNAP-THROUGH BEHAVIOR

This appendix contains details on formulations of the total potential energy associated with rotational transitions, as presented in Chapter 2.

A.1. MODEL A SINGLE BEAM

As discussed in Section 2.4 of the Chapter 2, we first describe the detailed formula for a single clamped-clamped beam by exploiting Mode 1 and 2, whereas the beam's deformed shape can be described as:

$$Y = A_1 Y_1 + A_2 Y_2, \tag{A.1}$$

and the initial shape is:

$$Y_0 = \frac{h}{2} Y_1 \quad \text{and} \quad A_1 = \frac{h}{2}, A_2 = 0, \tag{A.2}$$

where Y_0 represents the initial beam shape. A_1 and A_2 are unknown coefficients, which need to be solved on the basis of the principle of minimum energy. The corresponding bending (U_b) and compression (U_c) energy as a function of A_1 and A_2 can be expressed as:

$$U_b = \frac{EI}{2L^3}[(-h\boldsymbol{A_1} + \boldsymbol{A_1^2} + \frac{h^2}{4})C_1 + \boldsymbol{A_2^2}C_2], \tag{A.3}$$

$$U_c = \frac{EA}{8L^3}\{D_1^2\boldsymbol{A_1^4} + D_2^2\boldsymbol{A_2^4} + 2D_1D_2\boldsymbol{A_1^2}\boldsymbol{A_2^2} - \frac{h^2D_1^2}{2}\boldsymbol{A_1^2} - \frac{h^2D_1D_2}{2}\boldsymbol{A_2^2} + \frac{h^4D_1^2}{16}\}, \tag{A.4}$$

where C_1, C_2, D_1, D_2 are the integration constants, as shown below.

A

$$\begin{cases} C_1 = \int_0^1 (Y_1'')^2 dX = 8\pi^4 \text{ and } C_2 = \int_0^1 (Y_2'')^2 dX \approx 3.26 \times 10^3 \\ D_1 = \int_0^1 (Y_1')^2 dX = 2\pi^2 \text{ and } D_2 = \int_0^1 (Y_2')^2 dX \approx 40.3739 \end{cases} \tag{A.5}$$

A.2. MODELING UNIT CELLS VIA COUPLING TWO BEAMS

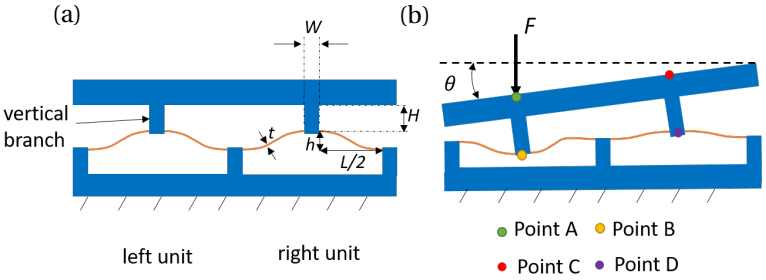

Figure A.1: The unit cell. (a) Structural geometry of the unit. b represents the out-of-plane dimension. (b) Illustration of the deformation of the unit when a point load applied at Point A.

Next, the left and right beam of the unit cell, illustrated in Fig. A.1, can be described as Y^L and Y^R, respectively. The total potential energy of the unit cell is composed of the bending energy of left and right beam (${U_b}^L$ and ${U_b}^R$), the compression energy of left and right beam (${U_c}^L$ and ${U_c}^R$), the bending energy of vertical branch (U_v) and potential energy (U_e). By substituting ${A_1}^L$, ${A_2}^L$ for A_1, A_2 in eqns. (A.3) and (A.4), ${U_b}^L$ and ${U_c}^L$ are derived as:

$${U_b}^L = \frac{EI}{2L^3}[(-h\boldsymbol{A_1}^{\boldsymbol{L}} + (\boldsymbol{A_1}^{\boldsymbol{L}})^{\boldsymbol{2}} + \frac{h^2}{4})C_1 + (\boldsymbol{A_2}^{\boldsymbol{L}})^{\boldsymbol{2}} C_2], \tag{A.6}$$

$$\begin{aligned} {U_c}^L = \frac{EA}{8L^3}\{&D_1^2(\boldsymbol{A_1}^{\boldsymbol{L}})^{\boldsymbol{4}} + D_2^2(\boldsymbol{A_2}^{\boldsymbol{L}})^{\boldsymbol{4}} + 2D_1D_2(\boldsymbol{A_1}^{\boldsymbol{L}}\boldsymbol{A_2}^{\boldsymbol{L}})^{\boldsymbol{2}} - \frac{h^2D_1^2}{2}(\boldsymbol{A_1}^{\boldsymbol{L}})^{\boldsymbol{2}} \\ &- \frac{h^2D_1D_2}{2}(\boldsymbol{A_2}^{\boldsymbol{L}})^{\boldsymbol{2}} + \frac{h^4D_1^2}{16}\}. \end{aligned} \tag{A.7}$$

Similarly, ${U_b}^R$ and ${U_c}^R$ can be obtained by substituting ${A_1}^R$, ${A_2}^R$ for A_1, A_2 in eqns. (A.3) and (A.4). According to the relation between ${A_1}^L$, ${A_1}^R$ and θ, ${U_b}^R$ and ${U_c}^R$ can be formulated by replacing ${A_1}^R$ with ${A_1}^L$ and θ. Furthermore, the bending energy of the vertical branch is expressed as:

$$\begin{aligned} U_v = \frac{EI_B(\theta-\theta_B)^2}{2H} + \frac{EI_B(\theta-\theta_D)^2}{2H} = \frac{EI_B(\frac{A_2^L C_s}{L}+\theta)^2}{2H} + \frac{EI_B(\frac{A_2^R C_s}{L}+\theta)^2}{2H}, \\ where\ I_B = \frac{bW^3}{12}\ \ and\ \ C_s = LY'|_{x=\frac{L}{2}} = -2 + [\frac{N_2^2}{2}+2]\cos(\frac{N_2}{2}), \end{aligned} \tag{A.8}$$

where θ_D and θ_B represent the angle at Point B and D during deformation (see Fig. A.1(b)). The potential energy (U_e), associated to applied load, is:

$$U_e = -Fd^A \approx -Fd^B = -F(h - 2{A_1}^L), \tag{A.9}$$

where d^A and d^B are the displacement of Point A and B. Therefore, the total potential energy is expressed as:

$$U_{tot} = {U_b}^L + {U_c}^L + {U_b}^R + {U_c}^R + U_e + U_v. \tag{A.10}$$

The governing equations can be derived by taking derivative with respect to the four coefficients, as shown below. In order to get the load-displacement ($F - d^A$) curve, the equilibrium equations are solved numerically by giving a range of F as inputs.

$$\frac{dU_{tot}}{d{A_1}^L} = 0, \quad \frac{dU_{tot}}{d{A_2}^L} = 0, \quad \frac{dU_{tot}}{d{A_2}^R} = 0, \quad \frac{dU_{tot}}{d\theta} = 0. \tag{A.11}$$

A.3. CONTACT BETWEEN THE UPPER AND BOTTOM FRAME

Although increasing h gives a wider gap between the upper and bottom frame, the increase of h will also lead to an increase of previously defined stable angle α, as shown in the Section 2.5. As a result, the required displacement to reach the rotational state is larger than the frame gap, causing contact to occur at the rotational state. This contact phenomenon induced by a large h can be observed in Fig A.2 below.

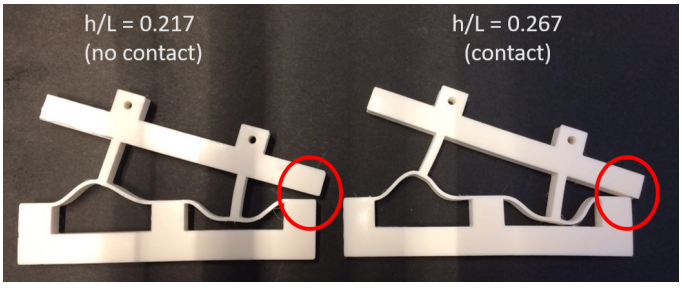

Figure A.2: Contact between the upper and bottom frame appears when h is increased.

B

SIMULATING PRE-STRESSING

This appendix includes details on the methodology we adopted in Chapter 3 for simulating the pre-stressing process in finite element models.

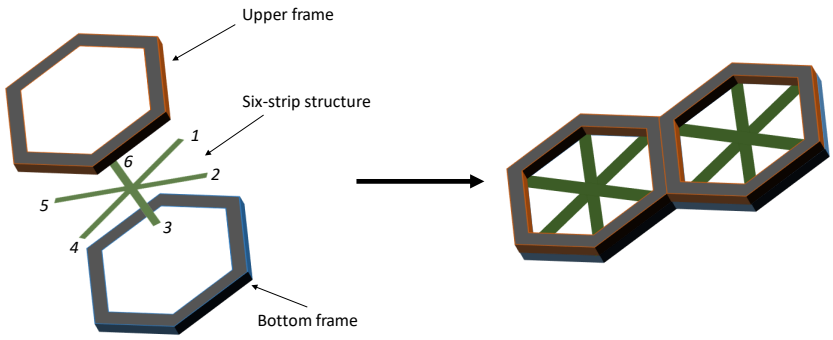

Figure B.1: The schematic of the initial stress-free structural geometry: each unit is composed of two frames and one thin six-strip structure.

To realize the pre-stressed and buckled configuration, we employed an equivalent thermal loading. Fig. B.1 displays a schematic of the initial stress-free geometry we started with. As mentioned in the main text, the structure is composed of a thin six-strip structure and two frames (upper and bottom). As illustrated in Fig. B.1, three branches (Strip 1,3,5) of the six-strip structure are connected with the upper frame while the rest of these strips (Strip 2,4,6) are tied with the bottom frame. In simulations, they are tied together using "tie" constraints in ABAQUS.

To the frames we assigned a thermal expansion coefficient equal to 0.08. Next, starting from the flat configuration as shown in Fig. B.2(a), we applied a temperature drop.

This thermal load causes the frames to shrink, see Fig. B.2(b). As the six-strip structure is connected to the frames, it will experience an in-plane compression, which leads to buckling of the six-strip structure. As a result of this buckling, the upper frame is lifted. In the end, the pre-stressed and buckled state is achieved, as depicted in Fig. B.2(c). Moreover, the distance between the upper and bottom frame, denoted as d in Fig. B.2(c), can be adjusted by changing the temperature as applied to the frames. In addition, we applied prescribed displacements on one side of the upper frame, resulting in a snapping to the tilted stable states.

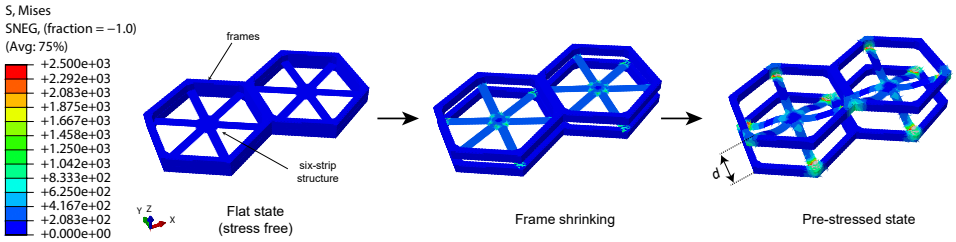

Figure B.2: Introduce pre-stress by applying thermal loads in FEA. (a) The initial flat state without stress. (b) Frames start to shrink under temperature change and therefore the upper and bottom frames start to detach. (c) The desired pre-stressed state.

C

MULTI-STABLE METASTRUCTURES FOR ENERGY ABSORPTION

C.1. THE ANALYTICAL MODEL

As discussed in Chapter 4, snap-through behavior of the curved solid beam can be predicted using an approximate analytical model. This section elaborates on the procedure for establishing the model. As shown in Fig. C.1(a), geometry of the curved beam can be described by H, T, L and B, consistent with the notations defined in the main text.

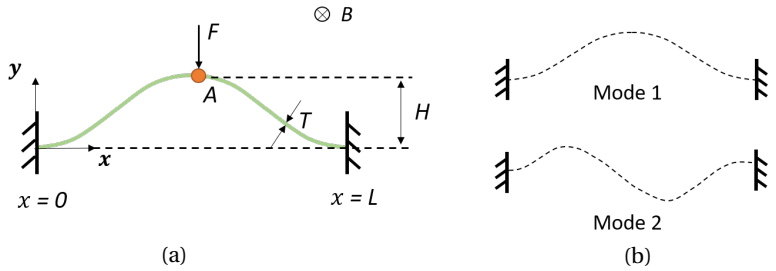

Figure C.1: Schematic of a curved beam under a load applied in the center. (a) Geometry of the beam is described based on the depicted $x-y$ coordinate system. A force is applied at Point A ($x = L/2$). (b) The first two buckling modes are illustrated, where the odd-number modes are symmetric with respect to $x = L/2$ and even-number modes are asymmetric.

According to Euler-Bernoulli theory, buckling modes of a straight beam that is axially compressed to buckle can be derived as:

$$y_i = 1 - \cos(N_i \frac{x}{L}) \quad \text{and} \quad N_i = (i+1)\pi, \quad \text{when} \quad i = 1,3,5... \tag{C.1}$$

where Eqn. (C.1) describes the symmetric mode shapes. Here, the first seven symmetric buckling modes are employed as bases, and the corresponding deformed shape (y) of the beam during loading is expressed as:

$$y = Q_1 y_1 + Q_3 y_3 + Q_5 y_5 + Q_7 y_7. \tag{C.2}$$

Here, $\mathbf{Q} = \{Q_1, Q_3, Q_5, Q_7\}$ is a row vector which includes the unknown coefficients. Next, bending energy of the beam (U_b) during loading can be calculated as:

$$U_b = \frac{EI}{2}\int_0^L (\frac{d^2y}{dx^2} - \frac{d^2y_0}{dx^2})^2 dx \text{ and } I_b = \frac{BT^3}{12}, \tag{C.3}$$

where E is Young's modulus and y_0 represents the initial curved shape ($y_0 = \frac{H}{2}(1-\cos(2\pi\frac{x}{L}))$). By substituting Eqn. (C.2) into Eqn. (C.3), U_b is then derived as:

$$U_b = \frac{EI}{2L^3}[(-HQ_1 + \frac{H^2}{4})C_1 + \sum_{j\in\{1,3,5,7\}} Q_j^2 C_j], \tag{C.4}$$

where C_j are the integration constants, as shown in Eqn. (C.5). ($'$ and $''$ represent the first and second derivative, respectively.)

$$\begin{cases} C_1 = \int_0^1 (Y_1'')^2 dX = 8\pi^4 \text{ and } C_3 = \int_0^1 (Y_3'')^2 dX = 128\pi^4 \\ C_5 = \int_0^1 (Y_5'')^2 dX = 648\pi^4 \text{ and } C_7 = \int_0^1 (Y_7'')^2 dX = 2048\pi^4 \\ X = x/L \ , \ Y_i = 1-\cos(N_i X) \text{ with } N_i = (i+1)\pi \text{ for } i = 1,3,5... \end{cases} \tag{C.5}$$

Furthermore, the compression energy U_c can be expressed as:

$$U_c = \frac{p\Delta s}{2} = \frac{EA(\Delta s)^2}{2L} \text{ with } A = BT, \ p = \frac{EA(\Delta s)}{L}, \tag{C.6}$$

where Δs represents the axial shrinkage of the curved beam during loading. In order to calculate Δs, we define s as the beam's length during deformation, and s_0 is defined as the beam's initial length. Under the assumption of small deformations, s can be formulated as:

$$s = \int_0^L \sqrt{1+(y')^2}dx \approx \int_0^L [1 + \frac{1}{2}(y')^2]dx. \tag{C.7}$$

The length change Δs is :

$$\begin{aligned} \Delta s = s - s_0 &= \frac{1}{2}\int_0^L (y'^2 - y_0'^2)dx \\ &= \frac{1}{2L}\{-\frac{H^2}{4}\underbrace{\int_0^1 (Y_1')^2 dX}_{\text{constant } D_1} + \sum_{j\in\{1,3,5,7\}} Q_j^2 \underbrace{\int_0^1 (Y_j')^2 dX}_{\text{constant } D_j}\}, \end{aligned} \tag{C.8}$$

where

$$D_1 = 2\pi^2, D_3 = 8\pi^2, D_5 = 18\pi^2, D_7 = 32\pi^2. \tag{C.9}$$

Next, U_c is derived by substituting Eqn. (C.8), (C.9) into (C.6), which leads to:

$$U_c = \frac{EA}{8L^3}[-\frac{H^2 D_1}{4} + \sum_{j\in\{1,3,5,7\}} Q_j^2 D_j]^2. \tag{C.10}$$

The total potential energy (U) is then derived as:

$$U = U_b + U_c + U_e \text{ and } U_e = -F[H - 2\sum_{j\in\{1,5\}} Q_j], \tag{C.11}$$

where U_e represents the potential energy associated with the applied force (F). The equilibrium equations can be obtained by taking the derivative of U with respect to each component in $\mathbf{Q}$. Then, the resulting system of equations with four unknown variables $\{Q_1, Q_3, Q_5, Q_7\}$ is solved by giving a range of F.

C.2. EXPERIMENTAL SETUP OF THE UNIAXIAL LOADING

As mentioned in the main text, the hierarchical, hollow and solid beams are printed with thermoplastic elastomers and then are connected to stiff frames. A representative sample can be found in Fig. C.2(a). For the uniaxial loading, rigid connectors are designed and fabricated with PLA, as demonstrated in the figure. Finally, the sample and connectors are connected to the load cell, as shown in Fig. C.2(b). During the test, displacement controlled loading is applied through the load cell, while bottom of the sample is fully clamped.

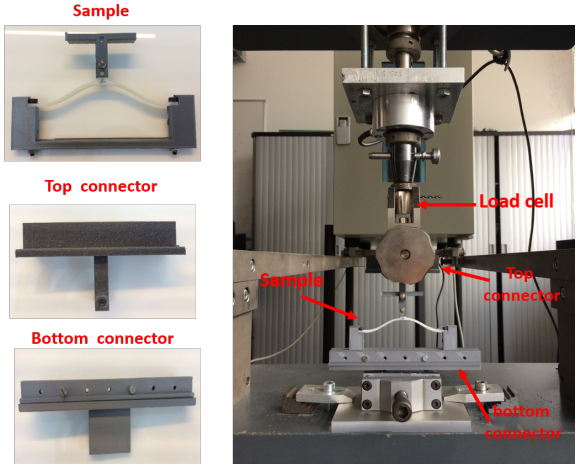

Figure C.2: The experimental setup of loading tests. (a) The sample, top and bottom connector. (b) The uniaxial loading test.

C.3. EFFECTS OF LATTICES ON BI-STABLE BEHAVIOR

As discussed in Section 4.4 of the main text, lattice parameters (t, θ) have minor influence on structural bi-stability. Here, using finite element models, t and θ are changed and the critical H/T corresponding to $F_{min} = 0$ is monitored. As displayed in Fig. C.3, it can be noted that as compared to T_v, changing t and θ do not influence H/T much.

This is because the lattice parameters play a minor role in tuning the bending stiffness. Consequently, varying t and θ do not affect F_{min} significantly.

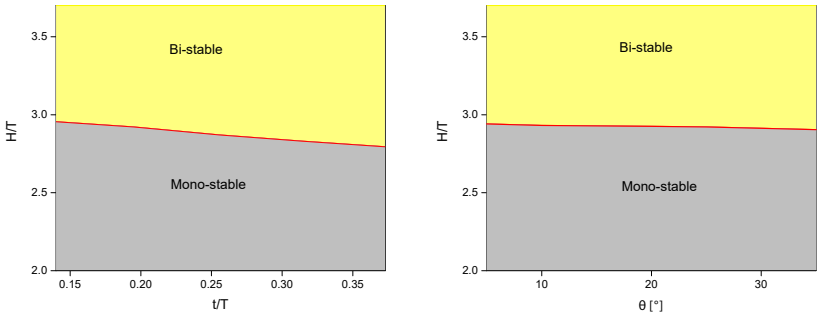

(a) (b)

Figure C.3: The effect of lattice parameters on bi-stability. Red curves in the figure correspond to the case of $F_{min} = 0$. (a) With changing t/T, the bi-stable region for hierarchical beams can be identified. (b) The influence of θ on H/T for structural bi-stability.

C.4. CYCLIC LOADING ON METASTRUCTURES

Cyclic loading has been performed on the metastructure to investigate the force reduction due to the polymer cyclic softening. Figure C.4 shows the measured force displacement curves for a 10-cycle loading-unloading. It can be seen that the critical loads (F_{max} and F_{min}) do not decrease much after 10 cycles, indicating that effect of the polymer's softening on the hysteresis is small.

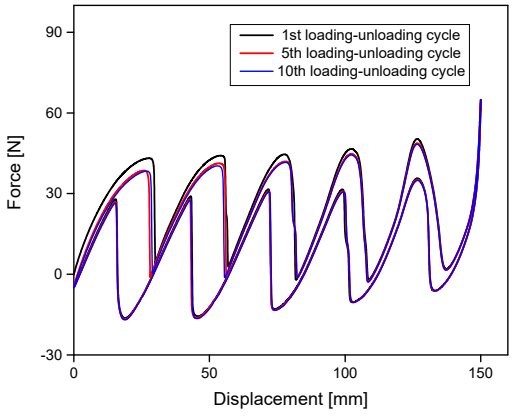

Figure C.4: The metastructure's force-displacement curves under 10 loading-unloading cycles.

D

THE ANALYTICAL MODEL FOR MULTI-STABLE SURFACES

D.1. MODELING THE SNAP-THROUGH TRANSITION

D.1.1. ROTATIONAL STIFFNESS K_t

As discussed in Section 5.3.2 of the main text, in order to calculate the structural total force (F), the first step is to determine the torsional stiffness (K_t). Here a pre-shaped beam subjected to a moment at the center is modeled, as shown in Fig. D.1(a) below. The geometry of the curved beam is described by h, t, L and b, as displayed in this figure.

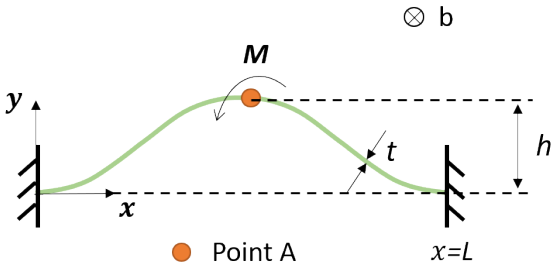

Figure D.1: Model a curved beam under a moment applied in the middle. The geometry of the beam-unit is described based on the depicted $x-y$ coordinate system. A moment is applied at Point A ($x = L/2$).

In order to model the structural deformation (moment-angle relation $M-\theta$), buckling modes have been exploited as bases to construct the displacement field. Then we derive the total potential energy of the structure. As presented in Appendix C.1, buckling modes for a straight beam under a compression can be expressed as y_i. Note that the modes corresponding to $i = 1,3,5...$ are symmetric with respect to the $x = L/2$, while for

$i = 2,4,6...$, the associated modes are asymmetric. When a moment applied at the center, the curved beam mainly experiences asymmetric deformations. Thus, the deformed shape (y) of the curved beam is formulated as:

$$y = \sum_{i\in\{1,2,4,6,8\}} A_i y_i, \tag{D.1}$$

where A_i is the unknown coefficient for each mode y_i. In particular, the initial curved shape of the beam y_0 can be expressed as:

$$y_0 = \frac{h}{2} y_1. \tag{D.2}$$

The displacement (d) of any point along the beam can be expressed as $d = y_0 - y$. Next, we calculate the strain energy of the curved beam. The corresponding bending (U_b) and compression energy (U_c) during the deformation can be calculated as:

$$U_b = \frac{E_b I_b}{2} \int_0^L (\frac{d^2 y}{dx^2} - \frac{d^2 y_0}{dx^2})^2 dx \text{ and } I_b = \frac{bt^3}{12}, \tag{D.3}$$

where E_b is Young's modulus. By substituting eqns. (D.1) to (D.3), U_b is derived as:

$$U_b = \frac{E_b I_b}{2L^3} [(-hA_1 + \frac{h^2}{4})C_1 + \sum_{j\in\{1,2,4,6,8\}} A_j^2 C_j], \tag{D.4}$$

where C_i are the integration constants (see eqns.(C.5)).

$$\begin{cases} C_1 = 8\pi^4, C_2 \approx 3.2608 \times 10^3, C_4 \approx 2.849 \times 10^4, \\ C_6 \approx 1.131 \times 10^5, C_8 \approx 3.132 \times 10^5. \end{cases} \tag{D.5}$$

Similarly, the compression energy (U_B) can be derived as:

$$U_c = \frac{E_b bt}{8L^3} [-\frac{h^2 D_1}{4} + \sum_{j\in\{1,2,4,6,8\}} A_j^2 D_j]^2, \tag{D.6}$$

where D_1, D_2, D_4, D_6, D_8 are $2\pi^2$, 40.3803, 119.35, 237.80, 395.73, respectively (refer to eqns. (C.8)). In addition, the potential energy (U_e) with regard to the applied moment (M) is formulated as:

$$U_e = M\theta \approx M \frac{d(y_0 - y)}{dx}|_{x=\frac{L}{2}}. \tag{D.7}$$

Finally, the total potential energy (U_{tot}) can be derived as:

$$U_{tot} = U_b + U_c + U_e. \tag{D.8}$$

Five governing equations can be obtained by taking the derivative of U_{tot} with respect to A_i, namely:

$$\frac{dU_{tot}}{dA_i} = 0 \text{ and } i = 1,2,4,6,8. \tag{D.9}$$

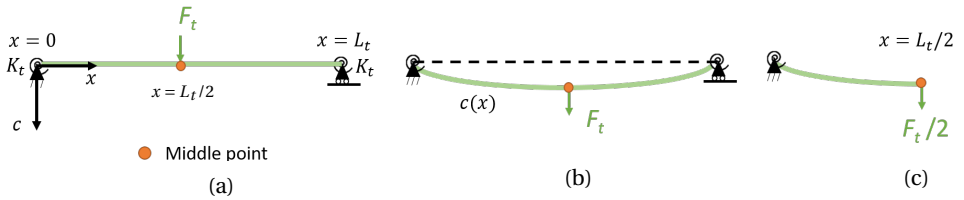

Figure D.2: The flat surface is simplified as a straight beam. (a) A beam structure subjected to a force in the middle. Two torsional springs with stiffness (K_t) are added. The beam is simply supported at two ends and the right end can move horizontally. (b) The deformed state of the beam. (c) According to the symmetric condition, half-beam is modeled.

D

D.1.2. DERIVATION OF F_t

As mentioned in the Section 5.3.2 of the main text, the plate structure is simplified to a simply supported flat beam, where two torsional springs are added on two ends, as illustrated in Fig. D.2(a). When the force (F_t) is exerted at the center, the structure will deform into a curved shape ($c(x)$), as shown in Fig. D.2(b). Based on the symmetric condition, $c(x)$ can be expressed as:

$$c(x) = \frac{S_1}{6}x^3 + \frac{S_2}{2}x^2 + S_3 x + S_4 \quad \text{for} \quad x \in [0, \frac{L_t}{2}], \tag{D.10}$$

where S_1, S_2, S_3, S_4 are unknown coefficients. The corresponding boundary conditions are:

$$\begin{cases} c(0) = 0, -E_t I_t c''(0) = -K_t \frac{dc}{dx}|_{x=0}, \\ c'(\frac{L_t}{2}) = 0, -E_t I_t c'''(\frac{L_t}{2}) = \frac{F_t}{2}, \end{cases} \tag{D.11}$$

where K_t is the computed torsional stiffness obtained in Appendix D.1.1 and $E_t I_t$ is the structural bending stiffness. Then, $c(x)$ is solved by combining eqns. (D.10) and (D.11), which results in:

$$c(\frac{L_t}{2}) = \frac{-F_t}{12E_t I_t}(\frac{L_t}{2})^3 + \frac{F_t L_t^2}{32E_t I_t(\frac{L}{2} + \frac{E_t I_t}{K_t})}(\frac{L_t}{2})^2 + \frac{F_t L_t^2}{8K_t L_t + 16E_t I_t}(\frac{L_t}{2}). \tag{D.12}$$

D.2. STRESS-STRAIN CURVES OF TPU MATERIAL

In this study, we fabricate a series of samples using thermoplastic elastomers. In order to characterize the material's properties, standard uniaxial tensile tests were conducted for the printed dumbbell specimens, as shown in Fig. D.3. Based on the measured stress-strain curve, a hyper-elastic model (Marlow) is adopted in ABAQUS to describe the constitutive relation.

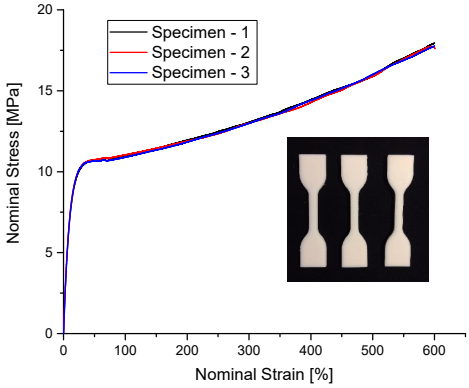

Figure D.3: Stress-strain curves for the material are obtained by standard tensile tests.

CURRICULUM VITÆ

Yong ZHANG

17-02-1992 Born in Yantai, China.

EDUCATION

since 2016 Ph.D. candidate in Mechanical Engineering
Department of Precision and Microsystems Engineering
Delft University of Technology

2014–2016 M.Sc. in Engineering Mechanics
Center for Composite Materials and Structures
Harbin Institute of Technology

2010–2014 B.Sc. in Engineering Mechanics
Department of Mechanics
China University of Mining and Technology

2007–2010 Yantai First Middle School

AWARDS

2021 Presentation Award
Advanced Engineering Materials and Structures Symposium, Luxembourg

2019 Best Poster Award
22nd Engineering Mechanics Symposium in the Netherlands

2012 National Scholarship for Undergraduates

List of Publications

Journal Papers

6. **Y. Zhang**, M. Tichem, F. van Keulen, (2021). A Novel Design of Multi-stable Metastructures for Energy Dissipation, Materials & Design, p.110234.

5. **Y. Zhang**, M. Tichem, F. van Keulen, (2021). Concept and Design of a Metastructure-Based Multi-stable Surface, Extreme Mechanics Letters, (accepted).

4. **Y. Zhang**, M. Tichem and F. van Keulen, (2020). Rotational snap-through behavior of multi-stable beam-type metastructures. International Journal of Mechanical Sciences, 193, p.106172.

3. C. Wang, Y. Zhao, **Y. Zhang**, L. Miao, J. Wu, Y. Yang, ... & C. Sui. (2020). Partially unzipping carbon nanotubes: A route to synchronously improve fracture strength and toughness of nanocomposites inspired by pinning effect of screw. Materials Today Communications, 25, 101355.

2. **Y. Zhang**, Q. Wang, M. Tichem and F. van Keulen, (2019). Design and characterization of multi-stable mechanical metastructures with level and tilted stable configurations. Extreme Mechanics Letters, 34, p.100593.

1. C. Sui, Q. Luo, X. He, L. Tong, K. Zhang, Y. Zhang, **Y. Zhang**, ... & C. Wang. (2016). A study of mechanical peeling behavior in a junction assembled by two individual carbon nanotubes. Carbon, 107, 651-657.

ACKNOWLEDGEMENTS

Over the last four and a half years, there was time period with joy as well as moment of frustration, both accompanying me to this page today. Pursuing a PhD in the Netherlands, although not easy, provides me with a unique opportunity to learn, and to grow, not only in research, but also in my life. During this journey, I am fortunate to get to know a group of nice people who have given me enormous support. I would like to take this chance to thank all of them.

First of all, I would like to thank my promotor & supervisor Prof. **Fred van Keulen** for his patient daily supervision and providing highly critical comments on my manuscripts. When I struggled with problems in the field of solid mechanics, he could always hit the nail right on the head with his rich and in-depth knowledge. Thanks for the commitment to this project. Moreover, I want to thank my co-promotor Dr. **Marcel Tichem** for his valuable comments related to my papers. I appreciate his efforts in providing supports and giving me freedom to be an independent researcher.

I would like to extend my thanks to Dr. **Qi Wang**, who gave me many critical remarks on my first paper. The discussion with him was always inspiring and I sincerely thank him for his kind help.

Besides, I want to appreciate Dr. **Chao Wang** and Prof. **Xiaodong He** at Harbin Institute of Technology for their generous help during my PhD application. The four-year sponsorship from the China Scholarship Council (CSC) is acknowledged for supporting this research.

This project contains a wealth of experimental work, for which the colleagues from PME department provided me with many useful suggestions, as well as a raft of elaborate trainings on a bunch of lab facilities. I want to thank **Patrick, Spiridon, Bradley, Gideon** and **Rob** for their indispensable technical support. In addition, the assistance from **Casper** in DASML Lab on impact testing is highly appreciated. Thanks also go to **Françoise** from BME department who helped me to use their testing system when the machine in my department did not function.

Lovely colleagues from SOM group and PME department make this journey more fascinating and fruitful. The awesome and active office environment I had facilitated efficient work flows and I really enjoy working with them. I would like to take this opportunity to thank: **Alejandro, Abilash, Ahmed, Andres, Can, Deepak, Dirk, Emiel, Freek, Hans, Jiayu, Just, Kai, Lidan, Max, Matthijs, Minxing, Murali, Pierre, Prabat, Renier, Roy, Sanne, Sabiju, Stijn, Tomas, Yi, Zhichao**. I would like to deliver my special thanks to **Arnoud** and **Vibhas** for their valuable feedback on my first paper, which helped me

a lot. I am grateful to my colleague **Rajit**, not only for his selfless help, but also for the enjoyable moments we had in playing table tennis. Besides, the support from PME secretaries makes it convenient for me to work efficiently at the office and I want to express my gratitude to **Birgit, Corinne, Eveline, Lisette, Marli and Marianne**.

Aside from office hours, this journey was also filled with a lot special moments with friends I met in the Netherlands. The accompanying of them and the relaxing gathering we had leave me with a lot of unforgettable memories and great joy. I would like to give my everlasting appreciation to them. **Bowen, Jian and Yandong**, I was lucky to meet you at the beginning of my PhD and we have shared countless joyful moments over the last four years. A special thanks goes to Bowen for helping me to study at TNW on Saturdays during the last few months of my PhD, which greatly expedited the process of writing the thesis. **Yabin and Yageng**, both currently becoming a college professor, I sincerely enjoyed all the moments with you in traveling, playing football, badminton, as well as in research. I have learned a lot from you on additive manufacturing and finite element methods. **Diankun**, who gave me valuable suggestions last year on my papers and research, the in-depth discussion with you steered me in the right direction whenever I needed. **Xianfeng**, my good friend as well as colleague in PME, we have talked a lot about funny things in research, as well as the frustration. Your vitality always perks me up. The lunch breaks with the hardworking and smart office-mate **Hanqing** were always refreshing, in particular during the pandemic. I enjoy a lot and wish you a lot of success with your papers. The generous help from **Long** and **Yueting** makes it easier for me to overcome obstacles in life, and I always cherish the friendship with them.

Finally, I would like to express my deepest gratitude to my parents, who are always patiently encouraging me and giving endless support during the past few years. You have set a great and perfect example to me, and your unmatched work ethics always motivate me to do my best. A big thanks to you from the depth of my heart, and I love you more than I can say.

老爸老妈, 感谢你们!

Yong Zhang
Delft, January 2021